THEORETISCHE PHYSIK

INAUGURAL-DISSERTATION

REAL-TIME TECHNIQUES FOR THE YANG-MILLS PLASMA

zur Erlangung des

DOKTORGRADES DER NATURWISSENSCHAFTEN

im Fachbereich Physik der
Mathematisch-Naturwissenschaftlichen Fakultät der
Westfälischen Wilhelms-Universität Münster

vorgelegt von

MARCUS TASSLER

aus LÜDENSCHEID

2009

Inaugural-Dissertation

Real-Time Techniques for the Yang-Mills Plasma

zur Erlangung des
Doktorgrades der Naturwissenschaften
im Fachbereich Physik der
Mathematisch-Naturwissenschaftlichen Fakultät der
Westfälischen Wilhelms-Universität Münster

Münster, August 2009

Vorgelegt von: *Arbeitsgruppe:*
Marcus Tassler   Owe Philipsen

Westfälische Wilhelms-Universität Münster

All human knowledge begins with the senses, proceeds from thence to concepts, and ends with ideas.

<div align="right">Immanuel Kant, KdV, B730</div>

Dedicated to my family.

Contents

1 Introduction

*The last thing one discovers in composing a work is what
to put first.*

Blaise Pascal

Little is known about time-dependent thermal processes and non-equilibrium phenomena in strongly interacting quantum systems. The problem is of particular significance in the light of recent experimental efforts to probe the quark-gluon plasma, i.e. the conjectured plasma phase of nuclear matter, in heavy-ion collisions. A thermodynamic analysis of quantum chromodynamics, the fundamental theory of the strong interactions, reveals the existence of a transition temperature separating two phases of nuclear matter. In the ordinary state of matter below this temperature quarks are confined into color neutral hadrons by the flux-tubes formed by a cloud of self-interacting gluons and resist direct observation. Beyond the transition temperature the existence of a plasma of free quarks and gluons is expected. This is where the state of confinement is breached and the fundamental nuclear constituents become accessible to direct observation. By probing the properties of nuclear matter in a plasma phase, additional insight can be gained into the nature of fundamental particles and interactions which shape physical reality. This research is of particular relevance to cosmology, due to the possible existence of a phase transition from a nuclear plasma to ordinary hadronic matter, including the neutrons and protons forming the basic building blocks of the elements, during the cooling of the universe after the Big Bang.

The notion that a dense, strongly interacting plasma is created in heavy ion collisions is supported by a number of model-independent observations, referred to as hard probes, which include jet quenching and J/ψ suppression as discussed below. Experiments have most notably been carried out at the Relativistic Heavy Ion Collider (RHIC) of Brookhavens National Laboratory and new experiments scheduled at the Large Hadron Collider (LHC) in Geneva as well as the planned Facility for Antiprotons and Ions Research (FAIR) in Darmstadt are set to shed additional light on this previously inaccessible state of matter. Existing theoretical tools for the description of strongly interacting many particle systems are continuously refined in the quest to reconcile fundamental theory and experimental evidence, laying the ground for progress in a wide range of areas from cosmology to the practical concerns of solid matter physics. The modern understanding of numerous distinct disciplines, ranging from nuclear physics to classical plasma dynamics, needs to be integrated into a comprehensive model of heavy ion collisions to facilitate a comparison between theoretical predictions and experimental observations. These efforts are significantly complicated by the fact that these collisions are a dynamic process consisting of many physically distinct stages which leave their imprint on experimental data. It is therefore a necessity to develop a solid understanding of dynamical processes in strongly interacting quantum systems if any contact between theory and experiment is to be established. As a first step towards this comprehensive understanding pure Yang-Mills theory is investigated employing perturbative as well as numerical techniques in the course of the research presented here. Significant progress in the quest to gain deeper insight into the real-time behavior of strongly interacting quantum systems has also been made in the context of AdS/CFT techniques which rely on a conjectured duality between super gravity on an $AdS_5 \times S^5$ manifold and $N = 4$ Super Yang-Mills theory defined on the asymptotic boundaries of

the anti de Sitter space. Since the applicability of this technique is limited to a specific supersymmetric Yang-Mills theory at infinite 't Hooft coupling and the relation to observables in ordinary Yang-Mills remains unclear a detailed discussion of these techniques is omitted.

A direct relation to recent experimental observations is established in various chapters of this thesis. The suppression of J/ψ resonances has long been speculated to be a signature of plasma formation. It remains debated whether the suppression of this charmonium state, which has already been observed at CERN's SPS facility at surprisingly low collision energies, can indeed be fully attributed to the formation of a strongly interacting deconfined state of matter or is caused partially by unrelated nuclear matter effects. Due to the prospect of using quarkonium resonances as a direct probe of interactions in the deconfined phase the in-medium modification of these resonances is repeatedly discussed throughout this thesis. It is shown in chapter 4 that the in-vacuo description of quarkonium by a Schrödinger equation can be extended to a thermal setting. This equation is subsequently used to define a thermal potential which can be directly related to the quarkonium spectral function and parametrizes both the energy and decay width of the ground state resonance. By taking the limit of infinite time and quark mass the real time static potential is defined as an analogue to the QCD static potential for a generic thermal medium.

The real-time static potential has by now been investigated in numerous other studies and predictions have been obtained for the initial phase of heavy ion collisions where an anisotropic distribution of gluon momenta is expected. These results are revisited in chapter 5. It is shown that changes to the real-time static potential, induced by varying the anisotropy of the momentum distribution of plasma constituents, are insignificant if the density of the medium is kept constant. To underline these findings the limit of asymptotically strong anisotropy is investigated where the quarkonium spectral function is found to remain in qualitative agreement with its counterpart in an isotropic medium. The perturbative analysis of quarkonium potentials in chapters 4 and 5 is supplemented by a lattice measurement of the free energy of a static $q\bar{q}$-pair in chapter 6. Some additional intuition is gained by a measurement of Polyakov loop correlators in the Green-Karsch effective theory as a naive strong coupling model for lattice Yang-Mills theory on coarse lattices.

As a first step towards a non-perturbative analysis of plasma dynamics the classical limit of statistical Yang-Mills theory is considered in chapter 7. It is shown that that the classical limit provides an excellent approximation for the dynamics of strongly occupied modes in any thermal quantum field theory with a clean separation between soft and hard energy scales. The problems resulting from the interdependence of hard and soft scales in Yang-Mills theory are highlighted. Large parts of this chapter are devoted to the numerical implementation of classical Yang-Mills theory on a Hamiltonian lattice. Analogous lattice techniques have been successfully applied in the context of baryogenesis and suffer from excessive thermalization times due to the necessity of generating a thermal ensemble of initial field configurations for the classical time evolution. The duality of the classical partition function to a Yang-Mills theory coupled to an adjoint Higgs field is used to employ standard Monte-Carlo techniques for the generation of the ensemble. A significant performance gain is achieved in comparison with conventional thermalization techniques and spurious thermalization times are eliminated.

One of the most important indications of the formation of a quark-gluon plasma is a significant reduction of the energy of jets at high momenta, referred to as jet quenching. The phenomenon is attributed to an energy loss of partons in a dense strongly interacting medium. It remains puzzling from a perturbative point of view that jets associated with heavy and light quarks or gluons experience a similar quenching. The phenomenon is studied in chapter 8, in the framework of the

classical lattice model developed in the previous chapter, by measuring non-perturbative corrections to the momentum diffusion of heavy quarks. The break down of the classical lattice model in the strong coupling regime is analyzed in detail. Further use is made of this model by measuring non-perturbative corrections to the imaginary part of the real-time static potential which is associated with Landau damping and thus sensitive to soft field dynamics.

From hydrodynamic simulations a multitude of additional properties of the plasma has been deduced. One of the best known results of hydrodynamic models is a low plasma viscosity, deduced from the elliptic flow of the expanding medium, making the quark-gluon plasma the most perfect liquid ever observed. To establish contact between the effective description of heavy ion collisions by relativistic hydrodynamics and perturbative QCD the semi-classical framework of kinetic theory is considered in chapter 9. Techniques developed in the context of the purely classical lattice model are extended to take into account the effects induced by hard, i.e. sparsely occupied modes, in the plasma. A generic framework is developed to simulate a plasma in the presence of an arbitrary hard mode background.

A prerequisite for the successful modeling of experimental data by hydrodynamic simulation is the assumption that a hydrodynamic description of the expanding plasma is viable already in early collision phases. From a theoretical point of view it is highly surprising that a local thermal equilibrium is established so rapidly. Recently Weibel-type instabilities, which have long been known to drive the rapid formation of a QED-plasma in the presence of an anisotropic background current, have been put forward as an explanation of this phenomenon. A numerical simulation of these instabilities is presented in chapter 10.

The presentation of the mentioned subjects is embedded in the attempt to give a rigid and comprehensive discussion of present analytical and numerical techniques to compute time dependent correlation functions in a Yang-Mills plasma in thermal equilibrium and beyond.

2 YANG-MILLS THEORY

God used beautiful mathematics in creating the world.

Paul Dirac

In this chapter a brief introduction to the theory underlying our present understanding of the fundamental forces encountered in high energy physics is given.

2.1 Introduction to Yang-Mills Theory

Since its formulation in 1954 Yang-Mills theory [1] has become one of the cornerstones of our modern understanding of the strong and electroweak forces. The theory is formulated on the manifold $\mathbb{R}^{d,1}$ of a flat Minkowskian space-time with d spatial dimensions and characterized by an invariance under local SU(N) transformations. Before proceeding to the Yang-Mills Lagrangian, it is necessary to introduce some mathematical notation. Let M be a manifold on which the symmetry group acts in some fixed representation. The *covariant derivative*, acting on a field $\psi \in \mathbb{R}^{d,1} \times M$, is then defined as

$$\mathrm{D}_\mu \psi(x) = (\partial_\mu - \mathrm{i}gA_\mu(x))\psi(x), \tag{2.1}$$

where $x \in \mathbb{R}^{d,1}$ denotes the position in space-time. The constant g is called the gauge coupling. The Lie algebra element $A_\mu(x) \in \mathrm{su}(N)$ is referred to as *gauge field*. Employing the usual Minkowski space notation covariant or contravariant space-time indices are written in greek letters while spatial indices will be indicated by latin letters. The repeated appearance of an index in a product implies a summation over the index unless explicitly stated otherwise. The curvature of the gauge field A defines the *field-strength tensor*

$$F_{\mu\nu} = \frac{\mathrm{i}}{g}[\mathrm{D}_\mu, \mathrm{D}_\nu] = \partial_\mu A_\nu - \partial_\nu A_\mu - \mathrm{i}g[A_\mu, A_\nu] \tag{2.2}$$

with $[A_\mu, A_\nu]$ being the commutator of the fields. The Yang-Mills Lagrangian can now be introduced as a quadratic invariant of the field curvature,

$$\mathscr{L}_{\mathrm{YM}} = -\frac{1}{4}\mathrm{Tr}F_{\mu\nu}F^{\mu\nu}. \tag{2.3}$$

Quantum chromodynamics (QCD), the standard theory for strong interactions [2, 3, 4], is obtained by supplementing the Yang-Mills Lagrangian with the Dirac Lagrangian of a fermion doublet in the fundamental representation,

$$\mathscr{L}_{\mathrm{D}} = \mathrm{i}\overline{\psi}\gamma^\mu \mathrm{D}_\mu \psi - m\overline{\psi}\psi, \tag{2.4}$$

for each quark species of respective mass m. The fermion fields $\psi \in \mathbb{R}^{d,1} \times G_N(\mathbb{C})$ are defined as complex N-dimensional Grassmann variables, transforming in the fundamental representation at each point in space-time. Many physical questions can be answered within pure Yang-Mills theory itself which is referred to as *quenched approximation*. The question of whether or not to include fermion contributions is often a question of precision versus conceptual clarity and it is an effective approach to investigate physical problems in a pure Yang-Mills framework first and to

obtain a more precise answer later in full QCD. Following this spirit the work presented here will be concerned with pure Yang-Mills theory. Modifications, introduced by an inclusion of fermions, are discussed where appropriate. To proceed with the discussion it is important to highlight the gauge invariance of Yang-Mills theory under a local gauge transformation $S(x) \in \mathrm{SU}(N)$ in more detail. The transformation acts on a field ψ defined on $\mathbb{R}^{d,1} \times M$ via

$$\psi(x) = S(x)\psi'(x). \tag{2.5}$$

By demanding the covariant derivative of ψ to transform in the same fashion as the field itself it is straightforward to derive the transformation behavior of the gauge field and field tensor

$$A_\mu = SA'_\mu S^{-1} + \frac{\mathrm{i}}{g} S\partial_\mu S^{-1} \quad \Rightarrow \quad F_{\mu\nu} = SF'_{\mu\nu} S^{-1}. \tag{2.6}$$

The gauge invariance of the Yang-Mills Lagrangian follows from the cyclicity of the trace. For quantities to be meaningful in Yang-Mills theory, it is natural to demand them to remain invariant under a local gauge transformation as well. To relate two fields $\psi, \phi \in \mathbb{R}^{3,1} \times M$ at different points $x, y \in \mathbb{R}^{3,1}$ in a gauge invariant fashion the parallel transport $W_\mathcal{C}(x, y)$ along a space-time curve $\mathcal{C}$ from x to y is introduced. Let $c(t) : \mathbb{R} \to \mathbb{R}^{d,1}$ be a parametrization of the curve $\mathcal{C}$ with $|\partial_t c| = 1$. The parallel transport along this curve is then defined by the differential equation

$$\partial_t W_\mathcal{C}(x, c(t)) = -\mathrm{i}g \frac{\partial c^\mu}{\partial t} A_\mu \quad \text{with} \quad W_\mathcal{C}(x, c(0)) = 1, \tag{2.7}$$

which is solved by an expression [5] commonly referred to as a *Wilson line* [$\mathcal{P}$ denotes a path ordering along the curve $\mathcal{C}$]:

$$W_\mathcal{C}(x, y) = \mathcal{P} \, \exp\left\{ -\mathrm{i}g \int_\mathcal{C} \mathrm{d}x^\mu A_\mu(x) \right\}. \tag{2.8}$$

The Wilson line transforms as $S^{-1}(y)W_\mathcal{C}(x, y)S(x)$ and thus renders the correlator of the fields $\psi(x), \phi^+(y)$ connected by a Wilson line invariant under arbitrary gauge transformations.

To conclude this section it remains to be pointed out that gauge field configurations can be separated into equivalence classes of configurations mutually related by continuous and differentiable gauge transformations. For many applications it is useful or even necessary to pick a subset of field configurations containing a single element for each equivalence class which is called *gauge fixing*. This is often done by specifying a certain gauge fixing condition. In Coulomb gauge, for instance, the spatial gradient of the gauge field vanishes: $\partial_i A^i = 0$. A more sophisticated method consists in supplementing the Yang-Mills Lagrangian with an explicit symmetry breaking term of the form

$$\delta\mathscr{L} = -\frac{(\partial_\mu A^\mu)^2}{2\lambda}. \tag{2.9}$$

These so called *covariant gauges* include the Landau ($\lambda \to 0$) and Feynman ($\lambda = 1$) gauges and will be used in their general form throughout this thesis. Some problems will necessitate the use of a temporal gauge $A_0 = 0$. It is important to point out that it is difficult to properly fix a gauge in Yang-Mills theory and that all commonly used gauges are plagued by a residual gauge invariance due to the existence of multiple intersections of gauge orbits with the hyper plane, proscribed by the gauge fixing, which are referred to as *Gribov copies* [6]. For a review of Yang-Mills theory see [7].

2.2   Euler-Lagrange Equations

Before proceeding to a quantization of Yang-Mills theory it is necessary to introduce the classical Euler-Lagrange equations obtained from the variation $\delta \mathcal{S}_{\mathrm{YM}} = 0$ of the Yang-Mills action,

$$\mathcal{S}_{\mathrm{YM}} = \int \mathrm{d}^4 x \left\{ \mathscr{L}_{\mathrm{YM}}(x) + g \mathrm{Tr} j^\mu(x) A_\mu(x) \right\}, \tag{2.10}$$

with respect to the gauge fields. External fields or charges coupled to the Yang-Mills field are represented by the *color current* $j^\nu \in \mathbb{R}^{d,1} \times \mathrm{su}(N)$. The process of quantizing the theory will consist in moving from the space of classical solutions to the complex Hilbert space of quantum states. As discussed in later chapters in more detail the classical theory itself is a useful approximation for quantum Yang-Mills theory at high temperatures and will serve as an indispensible tool for gaining an understanding of the dynamics of the Yang-Mills plasma. The Euler-Lagrange equations of Yang-Mills theory are referred to as the *Yang-Mills equations* and take the following simple form, with the covariant derivative acting on the adjoint components of the field curvature:

$$\mathrm{D}_\mu F^{\mu\nu} = j^\nu. \tag{2.11}$$

The analogy to the Maxwell equations of relativistic electrodynamics can be worked out in more detail by formulating the Yang-Mills equations in terms of electric and magnetic fields $E^i, B^i \in \mathbb{R}^{d,1} \times \mathrm{su}(N)$ defined by the following relations:

$$E_i = F_{0i} \qquad \text{and} \qquad B_i = -\frac{1}{2}\epsilon_{ijk}F_{jk}. \tag{2.12}$$

Choosing a temporal gauge the Yang-Mills equations can be written in the following form reminiscent of the familiar Maxwell equations for $d = 3$:

$$
\begin{aligned}
\partial_t \mathbf{B} &= -\mathbf{D} \times \mathbf{E} & \text{(Faraday's law of induction)} & \tag{2.13}\\
\partial_t \mathbf{E} &= \mathbf{D} \times \mathbf{B} - \mathbf{j} & \text{(Ampere's circuital law)} & \tag{2.14}\\
\mathrm{D} \cdot \mathbf{E} &= -j^0 & \text{(Gauss's law)} & \tag{2.15}
\end{aligned}
$$

The mapping between the gauge fields appearing in the covariant derivative and the electromagnetic fields is provided by the relation $A(t) = A(t_0) + \int_{t_0}^t \mathrm{d}t E(t)$. Upon decomposing the gauge fields into the adjoint components of the Lie algebra a set of Maxwell equations for $N^2 - 1$ electromagnetic fields coupled by a nonlinear memory term is obtained. An evaluation of this set of equations and in particular the numerical analysis of the classical statistics of the Yang-Mills field is a challenging task which will be discussed in detail in the chapters 7 and 8. It is shown that the classical theory provides a viable approximation to the physics of soft fields, i.e modes with high occupation numbers, in the full quantum theory at sufficiently high temperature. The application of a classical approximation to Yang-Mills theory is complicated by an interdependence of soft and hard momentum scales where quantum effects can not be neglected. The inclusion of these quantum effects is discussed in chapter 9 and illustrated in chapter 10 by an analysis of non-abelian plasma instabilities.

2.3   The Problem of Quantization and the Existence of a Mass Gap

Since Yang-Mills theory is expected to describe the force field of the strong interactions the question needs to be raised why wave solutions of the Yang-Mills equations are not observed on everyday length and energy scales while we are constantly surrounded by solutions of the Maxwell equations in the familiar form of light and the many electromagnetic phenomena encountered in our daily lives. This is a common way of stating the famous mass gap problem since it is assumed that quantum Yang-Mills theory is fundamentally different from its abelian counterpart and has no valid classical approximation at low energies due to the existence of a mass gap separating the lowest energy state from the vacuum. To understand how the nonlinear nature of the Yang-Mills field leads to fundamental differences to the electromagnetic interactions in a quantized theory it is instructive to consider the quantization of electromagnetism first. Let W be the space of solutions to the Maxwell equations modulo gauge transformations. W is an infinite dimensional linear space whose elements are represented by the classical plane wave solutions in a given gauge. The classical Hamiltonian is a positive quadratic function on W and thus provides a metric for the space of classical solutions. The theory is quantized in a rigid fashion by demanding that the Hamiltonian H must be represented by a bounded hermitian operator acting on the Hilbert space $\mathscr{H}$ of the quantized theory. The Hilbert space of energy eigenstates is then uniquely defined,

$$\mathscr{H} = \oplus_{n=0}^{\infty} \mathrm{Sym}^n W, \tag{2.16}$$

where $\mathrm{Sym}^n W$ is the subspace of classical solutions with an n-fold U(1)-symmetry (i.e. with n charges present). In the non-abelian theory the situation is more complicated since the space of classical solutions is neither linear nor is the Hamiltonian H quadratic. Thus a quantization along the previously sketched lines is only possible by expanding around the minimum of the energy where H is quadratic. The systematic expansion in the coupling constant of the quantized theory is referred to as *perturbation theory* (see chapter 3 for details). Energy eigenstates of nonlinear theories are *bound states* characterized by complex exchanges of the linear modes of the non-interacting theory. A perturbative treatment of Yang-Mills theory breaks down at low energies however due to a divergence of the running coupling while at asymptotically high energies the theory becomes non-interacting. This property is known as *asymptotic freedom* [8, 9]. It still remains an open question how to quantize nonlinear theories in a non-perturbatively valid way and to rigidly prove the existence of a mass gap in quantum Yang-Mills theory. For a more in depth discussion of these subjects the interested reader is referred to [10].

In practice the most viable method of quantizing Yang-Mills theory is by using path integral quantization. This amounts to stating that the expectation value of some function $f(A)$ is given by a path integral over all possible field configurations weighed by their classical action $\mathcal{S}$,

$$\langle f \rangle = \frac{1}{Z} \int [\mathrm{D}A] \, f(A) \mathrm{e}^{\mathrm{i}\mathcal{S}} \quad \text{with} \quad Z = \int [\mathrm{D}A] \, \mathrm{e}^{\mathrm{i}\mathcal{S}}. \tag{2.17}$$

Z is the *partition function* of the theory. By performing the *Wick rotation* $t \to \mathrm{i}\tau$ and discretizing the path integral on a lattice (see chapter 5) the system becomes amenable to a numerical treatment. The spectrum of energy eigenstates in Yang-Mills theory, referred to as *glueballs*, obtained in numerical simulation confirms the existence of a mass gap with the lowest excited energy eigenstate 0^{++} having the mass $m_{0^{++}} \simeq 1.7$ GeV.

2.4 External Charges and Confinement

In this section the concept of a *static charge* and the *binding energy* between charge multiplets is defined. Let $\psi \in M \times \mathbb{R}^{d,1}$ be a fermion field with the symmetry group acting on M in some representation r. From (2.4) the adjoint components of the associated color current are

$$j_\mu^a = \overline{\psi}\gamma_\mu T_r^a \psi, \tag{2.18}$$

with T_r^a denoting the generator a of $\mathrm{SU}(N)$ in the representation r. The color current is invariant under a local symmetry transformation $S \in r \times \mathbb{R}^{d,1}$ while gauge field configurations fulfilling the Yang-Mills equations (2.11) transform according to

$$S A^\mu S^{-1} = j^\mu. \tag{2.19}$$

To state the presence of a static color charge $j^0 = q\delta(x)$ in the representation r at some position $x \in \mathbb{R}^{d,1}$ thus means to demand that the gauge field component A^0 transforms in the representation r under a local SU(N) transformation at x. To remove field configurations not fulfilling the transformation property (2.19) in the path integral formalism a projection function is introduced. Let $\mathcal{C}$ be the world line of a localized color charge g in the representation r parametrized by the function $c(t) : \mathbb{R} \to \mathbb{R}^{d,1}, |c(t)| = 1$. The projection function $W_{\mathcal{C}}^r$ must equal the product of group characters of the gauge field in the representation r along $\mathcal{C}$ to ensures that unphysical configurations vanish upon integration over the gauge fields along the world line. It is straightforward to verify that the quantity satisfying this property is just the Wilson line (2.8) along $\mathcal{C}$ in the representation r. The simplest gauge invariant projector for a charge multiplet is given by a closed Wilson line, called *Wilson loop*, of the form

$$L[(x,y),(0,t)] = \frac{1}{N}\mathrm{Tr} \; \boxed{} \; = \frac{1}{N}\mathrm{Tr}\left\{ W_{x,0\to t} W_{x\to y,t} W_{y,t\to 0} W_{y\to x,0} \right\} \tag{2.20}$$

which corresponds to a static $q\overline{q}$-pair connected by a parallel transport along a straight spatial line between the constituent positions $x, y \in \mathbb{R}^d$. The pair exists in the time interval $[0,t]$. The ground state binding energy of any static charge multiplet is the lowest energy eigenstate in the presence of the charges. Let $Q(0,t)$ be a projection function for the charge multiplet suitably chosen to include field configurations with constant overlap to the ground state. The ground state energy V can then be determined by Wick rotation from the relation:

$$V = -\lim_{\tau \to \infty} \frac{\partial}{\partial\tau} \ln\langle Q(0,-\mathrm{i}\tau)\rangle \tag{2.21}$$

For a static $q\overline{q}$-pair the potential, as determined from lattice simulations, depends on the spatial separation x of the charges with a linear part due to the formation of a flux tube with string tension σ and a Coulomb part with effective coupling α_s [$\mathrm{C_F} = 2N/(N^2-1)$ is the fundamental Casimir]:

$$V^{q\overline{q}}(x) = -\mathrm{C_F}\frac{\alpha_s}{x} + \sigma x. \tag{2.22}$$

It is obvious that it is impossible to separate both charges since the potential becomes infinite in the limit $x \to \infty$. Since it is also clear from (2.21) that the binding energy is ill defined for any non gauge-invariant quantity, where $\langle Q \rangle = 0$, charge multiplets must form color neutral bound states of limited size. This phenomenon is referred to as *confinement*.

2.5   Yang-Mills Theory at Finite Temperature

To introduce the concept of a *medium* in a statistical sense it is again useful to choose a temporal gauge where the familiar framework of statistical mechanics can be applied in a straightforward fashion. Let $\hat{\sigma}$ be a Hermitian operator acting on the Hilbert space $\mathscr{H}$ of eigenstates to the set of gauge field operators $\{A_i(t, x)\}, x \in \mathbb{R}^d$ at a time $t = t_0$. The statistical expectation value of an arbitrary operator $\hat{f}$ in a medium, defined by the *statistical operator* $\hat{\sigma}$, is

$$\langle \hat{f} \rangle = \frac{1}{Z} \mathrm{Tr} \, \{\hat{\sigma}\hat{f}\} \quad \text{with} \quad Z = \mathrm{Tr} \, \hat{\sigma}, \tag{2.23}$$

where the trace runs over all states of the Hilbert space $\mathscr{H}$ and Z is called *partition function*. $\hat{\sigma}$ is also called *density matrix*. The density matrix for a relativistic system in thermal equilibrium was conjectured to be identical to the familiar non-relativistic Boltzmann factor by Jüttner in 1911 [11] while investigating a dilute relativistic gas. When referring to *thermal equilibrium* it is thus expressed that the distribution of states in a statistical system is described by the density matrix

$$\hat{\sigma}_{eq} = \mathrm{e}^{-\beta\hat{H} - \mu_i \hat{Q}_i} \tag{2.24}$$

where $\hat{H}$ is the Hamilton operator and $\beta = 1/T$ is the inverse temperature. The system of natural, where $\hbar = c = k_B = 1$, is used throughout this thesis unless stated otherwise. The operator $\mu_i \hat{Q}_i$ represents the set of classically conserved charges $\{Q_i\}$ and their associated chemical potentials. A rigid proof of Jüttners conjecture on a classical level is outstanding to the present day due to difficulties in formulating Hamiltonian mechanics for a relativistic system of interacting particles. Upon supplementing the Hilbert space $\mathscr{H}$ with a canonical commutation relation

$$[\hat{A}_i^a(x), \hat{E}_j^b(y)] = \mathrm{i}\delta_{ij}\delta_{ab}\delta(x - y) \tag{2.25}$$

between the adjoint components of the field operator and their conjugate momenta given by the electric fields $\hat{E}_i^a$ a path integral representation of the partition function is obtained as discussed in the next chapter. In the special case of thermal equilibrium and vanishing chemical potentials observables can be calculated by formulating the theory on the manifold M of a flat Euclidean space-time $\mathbb{R}^{d+1}$ with a compactified temporal dimension of extent β. The expectation value of an observable $\hat{f}$ is then given by the expression [12]

$$\langle f \rangle = \frac{1}{Z} \int [\mathrm{D}A] \, f(A)\mathrm{e}^{-\mathcal{S}_\mathrm{E}} \quad \text{with} \quad Z = \int [\mathrm{D}A] \, \mathrm{e}^{-\mathcal{S}_\mathrm{E}}. \tag{2.26}$$

with $x \in M$ and $\mathrm{S_E}$ denoting the Yang-Mills action (2.10) with a Euclidean metric. Time dependent observables are obtained by Wick rotation and analytical continuation of the corresponding euclidean quantities. In Euclidean Yang-Mills theory with a finite temporal extent β the relations (2.21,2.22) which led to the postulate of confinement are no longer valid. The fact that it is no longer possible to define the binding energy of a charge pair by taking the infinite Euclidean time limit is revisited in later chapters. By assuming the usual thermodynamic relations to hold it is however possible to define the free energy F of a charge multiplet represented by the projector Q:

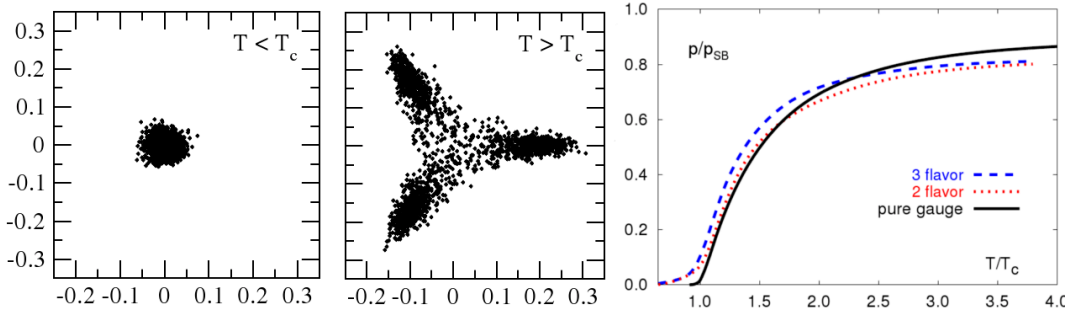$$F = -\beta \ln\langle Q \rangle \tag{2.27}$$

Figure 2.1: Scatter plots of the Polyakov loop in the complex plane for a thermal ensemble of randomly chosen SU(3) field configurations illustrating the Z(3) symmetry breaking in the deconfined phase (left and middle,[13]). The ratio p/p_{sb} for SU(3) shows that the Boltzmann limit of a free gas is not reached at relevant temperatures beyond deconfinement. The medium remains characterized by complex interactions (right,[14]).

It is instructive to investigate the free energy of a single static color charge g at a spatial position $x \in \mathbb{R}^d$ which is represented by a straight fundamental Wilson line in the Euclidean time direction closed by the compactification of the manifold and referred to as a *Polyakov loop*:

$$L_x = \frac{1}{N}\text{Tr}W_{x,0\to\beta} \tag{2.28}$$

Lattice measurements of this quantity indicate that upon lowering the temporal extent of the manifold there exists some critical temperature T_c where $\langle|L|\rangle$ takes on a finite value due to the spontaneous breaking of the global $Z(N)$ center symmetry of the theory (see figure 2.1). This renders the free energy of a $q\bar{q}$-pair represented by the projector $Q = L_x L_y^+$ finite at large separations between the charge positions $x, y \in \mathbb{R}^d$. There is thus some critical temperature where a transition to a phase occurs where charge multiplets are no longer required to be color neutral and unbound color charges may exist. The existence of a *deconfinement phase transition* can also be demonstrated with the free energy of a static charge singlet (see chapter 6) or by an analysis of dispersion relations. It was conjectured by Svetitsky and Yaffe [15] that any Yang-Mills theory formulated on a compactified $d + 1$ dimensional Euclidean space $\mathbb{R}^{d+1}$ with symmetry group G falls into the same universality class as a d-dimensional model of spins transforming in the center of the group $\mathcal{C}(G)$. The conjecture was verified for the SU(2) and SU(3) Yang-Mills theories in particular which fall into the universality class of the Ising and Potts model respectively. In the case of $d = 3$ the phase transition for SU(2) is thus second order while SU(3) exhibits a first order transition. Lattice measurements of the pressure p of Yang-Mills theory (see figure 2.1)

$$p(T) = T\frac{\partial}{\partial V}\ln Z \tag{2.29}$$

are well described by a glueball gas below the deconfinement phase transition [16]. Beyond the critical temperature the Stefan Boltzmann limit of a free gas $p_{sb}(T) \sim T^4$ is only approached at very high temperatures which indicates that Yang-Mills theory remains governed by complex interactions in the deconfined phase. It is thus a formidable theoretical challenge to understand the physical nature of Yang-Mills theory in the deconfined phase and to develop suitable calculation tools for venturing into this regime. This thesis will be devoted to the development and application of analytical and numerical techniques applicable to general statistical media governed by the Yang-Mills Lagrangian.

Perturbation Theory

3 Schwinger-Keldysh Formalism

*Imaginary time behaves like another direction in space,
histories in imaginary time can be closed surfaces, like the
surface of the Earth, with no beginning or end.*

Stephen Hawking

This chapter will serve as an introduction to the path integral representation of expectation values in general statistical quantum field theories. The Schwinger-Keldysh contour as well as the derived diagrammatic techniques are introduced. Thermal equilibrium is discussed as a special case.

3.1 Schwinger-Keldysh Contour

To evaluate the expectation value of an arbitrary operator $\hat{Q}$ in a statistical quantum system with a density of states characterized by the statistical operator $\hat{\sigma}$ the following relation must be solved:

$$\langle \hat{Q} \rangle = \frac{1}{Z} \text{Tr}\{\hat{\sigma}\hat{Q}\} = \frac{1}{Z} \int [\text{D}\varphi] \langle \varphi | \hat{\sigma}\hat{Q} | \varphi \rangle. \tag{3.1}$$

No restrictions are made on the nature of the operator $\hat{Q}$ which may be time dependent and non-local. The statistical operator $\hat{\sigma}$ is defined at a time $t = 0$ in Minkowski space $\mathbb{R}^{d,1}$ which will be referred to as the initial time. The trace runs over all field eigenstates spanning the Hilbert space of the system span $\{|\varphi\rangle\} = \mathscr{H}$. To construct a path integral representation of (3.1) a complete set of field eigenstates spanning the Hilbert space $\mathscr{H}$

$$\mathbf{1} = \int [\text{D}\psi] |\psi\rangle\langle\psi| \tag{3.2}$$

is inserted to separate off the statistical operator:

$$\langle \hat{Q} \rangle = \frac{1}{Z} \int [\text{D}\varphi][\text{D}\psi] \langle \varphi | \hat{\sigma} | \psi \rangle \langle \psi | \hat{Q} | \varphi \rangle. \tag{3.3}$$

The second amplitude is expressed as a path integral by inserting alternating sets of field and momentum eigenstates at infinitesimal distances along a contour $\zeta[s]$, $\zeta : \mathbb{R} \to \mathbb{C}, s \in [0,1]$ in the complex time plane. For a general introduction on the construction of path integrals see [17] for instance. The amplitude involving the statistical operator subsequently takes the form

$$\langle \psi | \hat{Q} | \varphi \rangle = \int_\zeta [\text{D}\varphi] Q(\varphi) e^{iS_\zeta} \Big|_{\varphi_0 = \varphi, \varphi_1 = \psi} \tag{3.4}$$

where $\varphi_s = \varphi(\zeta[s])$ is the field configuration at the time $t = \zeta[s]$. The path integral along the contour is defined via

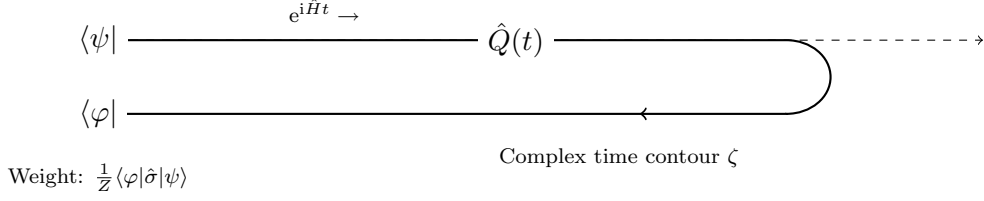$$\int_\zeta [\text{D}\varphi] = \lim_{\Delta_s \to 0} \prod_{s=1}^{1/\Delta_s} [\text{D}\varphi_{s\Delta_s}]. \tag{3.5}$$

Figure 3.1: Path integral representation of the amplitude $\langle\psi|\hat{Q}(\{t_i\})|\varphi\rangle$ using the Schwinger-Keldysh integration contour ζ. The choice of the contour is customary and constrained only by the boundary conditions $\zeta(0) = \zeta(1) = 0$ and the necessity to pick up the time dependence of the operator $\{t_i\} \in \zeta(s)$.

The action S_ζ is defined as the integral of the Lagrangian $\mathscr{L}(t)$ of the theory, analytically continued to the complex time plane, along the contour ζ:

$$S_\zeta = \int_\zeta \mathrm{d}t\, \mathscr{L}(t) = \int_0^1 \mathrm{d}s \frac{\partial \zeta[s]}{\partial s} \mathscr{L}(\zeta[s]). \tag{3.6}$$

The choice of the contour ζ is limited only by the following mild restrictions and otherwise completely arbitrary [18]:

1. ζ is continuous, differentiable and constrained by the boundary conditions $\zeta[0] = \zeta[1] = 0$. The contour should not intersect with itself.

2. The contour ζ must contain the observable $\hat{Q}$, i.e. if the observable can be decomposed into local operators $\{\hat{Q}_i\}$ via $\hat{Q} = \prod_i \hat{Q}_i(t_i)$ the contour must contain the set of points $\{t_i\} \in \mathbb{C}$.

Since the purpose of this technique will be to calculate observables defined at physical times, the contour should include the real axis for practical applications. The customary choice of contour is the Schwinger-Keldysh contour [19, 20] shown in figure 3.1 which follows the real time axis to infinity and returns on a parallel line shifted by the amount $-i\epsilon \to 0$ along the imaginary time axis. To summarize, the path integral representation of the expectation value of an arbitrary quantity $\hat{Q}$ takes the following form for a system characterized by the Lagrangian $\mathscr{L}$ and the density of states $\hat{\sigma}$ in the Schwinger-Keldysh formalism:

$$\langle\hat{Q}\rangle = \frac{1}{Z} \int_\zeta [\mathrm{D}\varphi]\sigma(\varphi_0, \varphi_1)Q(\varphi)e^{iS_\zeta(\varphi)}. \tag{3.7}$$

The field configuration $\varphi_s = \varphi(\zeta[s])$ is defined at the complex time $\zeta[s]$ on the Schwinger-Keldysh contour. The partition function Z is defined as

$$Z = \int_\zeta [\mathrm{D}\varphi]\sigma(\varphi_0, \varphi_1)e^{iS_\zeta(\varphi)} \tag{3.8}$$

where the action S_ζ is obtained by integrating the Lagrangian $\mathscr{L}(t)$ along the time contour ζ. The statistical weight $\sigma(\varphi_0, \varphi_1)$ represents the amplitude

$$\sigma(\varphi_0, \varphi_1) = \langle\varphi_1|\hat{\sigma}|\varphi_0\rangle. \tag{3.9}$$

It is emphasized that the path integral representation derived here is completely general and can be applied to any statistical quantum field theory. The implications as well as diagrammatic techniques for the practical evaluation of expectation values are discussed in the following sections.
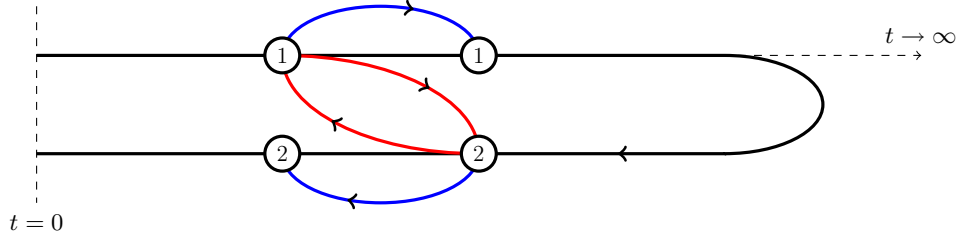
Figure 3.2: Illustration of a propagator in the real-time formalism.

3.2   Real-Time Correlators

Let $\hat{\varphi}(t), \psi(t')$ be two operators, which are local in time and contained in the Schwinger-Keldysh contour ζ. To define both correlators unambiguously an index $i \in \{1, 2\}$ is introduced to specify whether the respective operator is located on the forward time part ($i = 1$) or backward part ($i = 2$) of the contour. Using these indices the correlator of both operators is written in the matrix form

$$\mathrm{i}\boldsymbol{G} = \mathrm{i} \begin{pmatrix} G_{11} & G_{12} \\ G_{21} & G_{22} \end{pmatrix} = \begin{pmatrix} \langle \mathrm{T}\hat{\psi}(t')\hat{\varphi}(t) \rangle & -\langle \hat{\varphi}(t)\hat{\psi}(t') \rangle \\ \langle \hat{\psi}(t')\hat{\varphi}(t) \rangle & \langle \tilde{\mathrm{T}}\hat{\psi}(t')\hat{\varphi}(t) \rangle \end{pmatrix}, \tag{3.10}$$

where the first index specifies the location of $\hat{\psi}$ and the second index the location of $\hat{\varphi}$ on the contour as illustrated in figure 3.2. A time or anti-time ordering is imposed by the operators T and $\tilde{\mathrm{T}}$ respectively. Note that the inclusion of the prefactor i in the definition of the correlator is customary. According to their definition the components of the correlator are not independent and obey the relation

$$G_{11} + G_{22} = G_{12} + G_{21}, \tag{3.11}$$

reducing the correlator to at most 3 independent entries. It is convenient for many applications to choose a basis where this is accounted for explicitly:

$$\boldsymbol{G}' = \boldsymbol{R}^{-1} \cdot \boldsymbol{G} \cdot \boldsymbol{R} = \begin{pmatrix} 0 & G_A \\ G_R & G_S \end{pmatrix}. \tag{3.12}$$

The component G_R is called the retarded, while G_A is referred to as the advanced and G_S as symmetric. The transformation matrix mediating between both representations is defined via:

$$\boldsymbol{R} = \frac{1}{\sqrt{2}} \begin{pmatrix} 1 & 1 \\ -1 & 1 \end{pmatrix} \quad \text{and} \quad \boldsymbol{R}^{-1} = \frac{1}{\sqrt{2}} \begin{pmatrix} 1 & -1 \\ 1 & 1 \end{pmatrix}. \tag{3.13}$$

In a homogeneous system where the statistical operator is independent of space-time the correlator $\mathbf{G}(x, x')$ of two local operators $\hat{\varphi}(x)$ and $\hat{\psi}(x')$ defined at the space time positions $x, x' \in \mathbb{R}^{d,1}$ will only depend on the separation between both positions $\mathbf{G} = \mathbf{G}(x - x')$. A momentum space representation of the correlator is defined via the following Fourier transform in this case:

$$\mathbf{G}(K) = \int \mathrm{d}^{d+1}x\, \mathrm{e}^{\mathrm{i}K_\mu x^\mu} \mathbf{G}(x), \quad \mathbf{G}(x) = \int \frac{\mathrm{d}^{d+1}K}{(2\pi)^{d+1}} \mathrm{e}^{-\mathrm{i}K_\mu x^\mu} \mathbf{G}(K) \tag{3.14}$$

A homogenity of the system, which is assumed throughout this thesis, imposes the additional constraint

$$G_A(K) = G_R^*(K) \tag{3.15}$$

on the correlator in momentum space reducing the number of independent components to two. In thermal equilibrium there is only one independent entry of the correlator due to the Kubo-Martin Schwinger condition.

3.3 Free Theory

As a first step in the introduction of a perturbative technique suitable for application to a general quantum field theory out of equilibrium a free gas of scalar bosons is considered. The discussion will loosely follow the lines of [21], and the Greens functions introduced in this section will serve as fundamental building blocks in the perturbative series obtained for a general interacting system. The momentum distribution $f(\boldsymbol{p})$ of the particles constituting the gas is arbitrary with the only prior being the restriction of particle momenta to a mass shell imposed by the dispersion relation:

$$\omega^2 = \pi(\boldsymbol{p}), \tag{3.16}$$

where $\pi(\boldsymbol{p}) = \boldsymbol{p}^2$ for a massless particle. Let $\hat{a}(P)$ be the creation operator for a particle with on-shell momentum $P = (\omega, \boldsymbol{p})$ in the canonical formalism. The statement that the momentum distribution of particles in the system is $f(\boldsymbol{p})$ is equivalent to the formal relations:

$$\langle \hat{a}^+(P)\hat{a}(P) \rangle = f(\boldsymbol{p}) + \Theta(-\omega) \quad \text{and} \quad \langle \hat{a}(P)\hat{a}^+(P) \rangle = f(\boldsymbol{p}) + \Theta(\omega). \tag{3.17}$$

This immediately translates into the following Greens functions for particle and anti-particle propagation:

$$G_{12}(P) = -2\pi\mathrm{i}(f(\boldsymbol{p})+\Theta(-\omega))\delta(\omega^2-\pi(\boldsymbol{p})) \quad \text{and} \quad G_{21}(P) = -2\pi\mathrm{i}(f(\boldsymbol{p})+\Theta(\omega))\delta(\omega^2-\pi(\boldsymbol{p})). \tag{3.18}$$

In addition the retarded propagator is constrained by the dispersion relation which is expressed by the following differential equation in position space:

$$\left[(i\partial_t)^2 - \pi(-\mathrm{i}\nabla_{\boldsymbol{r}})\right] G_R(t, \boldsymbol{r}) = \delta(t)\delta^{(d)}(\boldsymbol{r}). \tag{3.19}$$

This corresponds to the momentum space form

$$G_R(P) = \hat{P}\frac{1}{\omega^2 - \pi(\boldsymbol{p})}, \tag{3.20}$$

where $\hat{P}$ denotes the principal part. The advanced propagator in a homogeneous system is related to the retarded propagator by complex conjugation. By making use of the identity

$$\frac{1}{\omega^2 - \pi(\boldsymbol{p}) + \mathrm{i}\epsilon} = \hat{P}\frac{1}{\omega^2 - \pi(\boldsymbol{p})} - \mathrm{i}\pi\delta(\omega^2 - \pi(\boldsymbol{p})) \tag{3.21}$$

and the relations (3.12) the remaing propagators are obtained. The complete set of real-time propagators is written in a compact form by separating vacuum and in-medium contributions:

$$\boldsymbol{G}(P) = \boldsymbol{G}^{\mathrm{vac}}(P) + \boldsymbol{G}^{\mathrm{med}}(P). \tag{3.22}$$

The vacuum component is defined as

$$\boldsymbol{G}^{\mathrm{vac}}(P) = \begin{pmatrix} \frac{1}{\omega^2-\pi(\boldsymbol{p})+\mathrm{i}\epsilon} & 0 \\ 0 & \frac{-1}{\omega^2-\pi(\boldsymbol{p})-\mathrm{i}\epsilon} \end{pmatrix} - 2\pi\mathrm{i}\delta(\omega^2 - \pi(\boldsymbol{p})) \begin{pmatrix} 0 & \Theta(-\omega) \\ \Theta(\omega) & 0 \end{pmatrix} \tag{3.23}$$

while the in-medium component is:

$$\boldsymbol{G}^{\text{med}}(P) = -2\pi\mathrm{i}\delta(\omega^2 - \pi(\boldsymbol{p}))f(\boldsymbol{p})\begin{pmatrix} 1 & 1 \\ 1 & 1 \end{pmatrix}. \tag{3.24}$$

In the context of perturbation theory the propagators of the free theory are referred to as *bare propagators*. In a basis of retarded, advanced and symmetric components the bare propagator of a scalar boson takes the form:

$$\begin{pmatrix} 0 & G_A \\ G_R & G_S \end{pmatrix} = \hat{P}\begin{pmatrix} 0 & \frac{1}{\omega^2 - \pi(\boldsymbol{p})} \\ \frac{1}{\omega^2 - \pi(\boldsymbol{p})} & 0 \end{pmatrix} - 4\pi\mathrm{i}\delta(\omega^2 - \pi(\boldsymbol{p}))f(\boldsymbol{p})\begin{pmatrix} 0 & 0 \\ 0 & 1 \end{pmatrix} \tag{3.25}$$

It is evident that the impact of the momentum distribution $f(\boldsymbol{p})$ on particle propagation is confined to the symmetric component which will facilitate the discussion of in medium effects in later chapters.

3.4 Perturbation Theory

The perturbative series approximating the expectation value of an observable $\hat{Q}$ in a general quantum field theory is obtained by expanding $\langle\hat{Q}\rangle$ in powers of the coupling constants $\{g_i\}, i \in \{1,\dots,n\}$ of the theory truncated at some finite order of the expansion. For transparency the construction of the series will be discussed for the example of a neutral scalar field with quartic self interaction. The expectation value of the operator $\hat{Q}$ is defined by (3.7)

$$\langle\hat{Q}\rangle = \frac{1}{Z}\int_\zeta[\mathrm{D}\varphi]\ \sigma(\varphi_0, \varphi_1)Q(\varphi)\mathrm{e}^{\mathrm{i}S_\zeta(\varphi)}. \tag{3.26}$$

The statistical weight σ is assumed to be the weight of a free bosonic gas, i.e. to be independent of the coupling constant for now. The action of the theory appearing in the path integral representation (3.7) is split into the action along the forward and backward part of the contour

$$S_\zeta = \int_\zeta\mathrm{d}t\mathscr{L}(t) = \int_0^\infty\mathrm{d}t(\mathscr{L}_1(t) - \mathscr{L}_2(t)) \tag{3.27}$$

where the Lagrangians along the respective parts of the contour are defined as:

$$\mathscr{L}_i(t) = \int\mathrm{d}^d\mathbf{x}\left\{\frac{1}{2}\left[(\partial_\mu\varphi_i)(\partial^\mu\varphi_i) - m^2\varphi_i^2\right] - \frac{\lambda}{4!}\varphi_i^4 + j_i\varphi_i\right\}. \tag{3.28}$$

The index $i \in \{1,2\}$ indicates whether an operator is defined on the forward or backward part of the contour. An external current j has been added to facilitate the perturbative expansion. In the next step the interaction term is isolated:

$$S_\zeta(\varphi) = S_\zeta^0(\varphi) + \sum_{i\in 1,2}S_\zeta^i(\varphi) \quad \text{where} \quad S_\zeta^i(\varphi) = (-1)^i\frac{\lambda}{4!}\int\mathrm{d}^{d+1}x\ \varphi_i^4(x). \tag{3.29}$$

Note that the initial time has been shifted to $-\infty$ to write the interaction as an integral over the full space-time manifold. The interaction term associated with the forward part of the contour is

identical to the vertex of φ^4 theory in the vacuum while the vertex for the backward part acquires an opposite sign due to the different time direction. By expanding the exponential of the action in powers of the coupling constant λ the expectation value is rewritten as:

$$\langle \hat{Q} \rangle = \frac{1}{Z} \int_\zeta [\mathrm{D}\varphi] \mathrm{e}^{\mathrm{i}S_\zeta^0(\varphi)} \sigma(\varphi_0, \varphi_1) Q(\varphi) \sum_{n=0}^\infty \frac{\mathrm{i}^n}{n!} \left(S_\zeta^1 + S_\zeta^2 \right)^n (\varphi). \tag{3.30}$$

In the absence of an external current this can also be written as:

$$Q\left(\frac{\delta}{\delta j}\right) \sum_{n=0}^\infty \frac{\mathrm{i}^n}{n!} (S_\zeta^1 + S_\zeta^2)^2 \left(\frac{\delta}{\delta j}\right) \ln Z_0 \Big|_{j=0} \quad \text{where} \quad Z_0 = \int [\mathrm{D}\varphi] \mathrm{e}^{\mathrm{i}S_\zeta^0(\varphi)} \tag{3.31}$$

It is now a straightforward exercise to derive Wicks theorem along the usual lines. The following rules for the construction of Feynman diagrams are obtained in position space:

1. The topological structure of diagrams is identical to the vacuum case. For each interaction a summation must be performed over vertices of type 1 and type 2 defined on the two strips of the Schwinger-Keldysh contour. Both vertices differ by their sign and the type 1 vertex is $i\lambda$. As usual the position of every vertex is integrated over the space-time manifold.

2. The vertices are connected by the bare propagators introduced in (3.22) transformed to position space with a vertex of type i and a vertex of type j connected by the propagator $G_{ij}(x)$.

3. The expectation value of an operator is obtained by summing over all possible diagrams for the given set of particles and interactions constrained by the external legs representing the operator. The symmetry factors for the diagrams as well as order of the expansion must be taken into account as prefactors.

Upon making the transition to momentum space the integrals over the space-time manifold at each vertex translate into momentum conservation and a momentum integration must be performed for each unconstrained propagator. The difference to ordinary perturbation theory in the vacuum state thus consists only in the necessity to sum over two types of vertices for each interaction. In addition the bare propagator connecting two vertices is now a 2×2 matrix containing additional on shell insertions of the momentum distribution. The situation is more complicated, if the statistical factor itself depends on the coupling constant since σ must then be expanded in the coupling constant as well compromising the perturbative scheme previously introduced. In thermal equilibrium the problem is remedied by expressing the statistical prefactor as an additional branch of the integration contour as discussed in the next section. A momentum distribution f is often imposed on a system and directly inserted into the free propagators (3.22) again implicitly assuming the statistical weight of a free gas. In many media a hierarchy of energy scales is encountered which often involve the coupling constant. A typical example is the hierarchy of electric, magnetic and hard scales encountered in equilibrium Yang-Mills theory (see the next section). This additional dependence on the coupling invalidates naive perturbative schemes and necessitates a replacement of bare propagators and vertices with their full (resummed) counterparts. A fundamental relation employed for the derivation of resummed propagators and vertices is the Schwinger Dyson relation

$$\langle \frac{\delta}{\delta \hat{\varphi}} \hat{Q} \rangle = -\mathrm{i} \langle \hat{Q} \frac{\delta}{\delta \hat{\varphi}} S_\zeta \rangle \tag{3.32}$$

where $\hat{Q}$ is a polynomially bounded operator. The relation is proven by partial integration for an arbitrary $x = (t, \boldsymbol{x}) \in \mathbb{C} \times \mathbb{R}^d$ satisfying $t \neq 0$. Applied to the n-point functions of the theory the Schwinger Dyson equation represents an infinite tower of relations coupling the full n-point functions. It is important to point out that in the Schwinger-Keldysh formalism there are relations for the derivative in (3.32) acting on the forward and backward part of the contour. The Schwinger Dyson relation for the resummed two point function $\tilde{\boldsymbol{G}}$ takes the following form in momentum space

$$\tilde{\boldsymbol{G}} = \boldsymbol{G} + \boldsymbol{G} \cdot \boldsymbol{\Pi} \cdot \tilde{\boldsymbol{G}}, \tag{3.33}$$

where $\boldsymbol{\Pi}$ is the self energy resumming one particle irreducible interactions and $\boldsymbol{G}$ the bare propagator. The bold print indicates matrices with respect to Schwinger-Keldysh indices. Note that the self energy is transformed to a basis of retarded, advanced and symmetric components via:

$$\boldsymbol{\Pi}' = \boldsymbol{R}^{-1} \cdot \boldsymbol{\Pi} \cdot \boldsymbol{R} = \begin{pmatrix} \Pi_S & \Pi_R \\ \Pi_A & 0 \end{pmatrix}. \tag{3.34}$$

In this basis the following set of Schwinger-Dyson equations for the resummed two-point function ensues:

$$\begin{aligned} \tilde{\boldsymbol{G}}_{\mathrm{R,A}} &= \boldsymbol{G}_{\mathrm{R,A}} + \boldsymbol{G}_{\mathrm{R,A}} \cdot \boldsymbol{\Pi}_{\mathrm{R,A}} \cdot \tilde{\boldsymbol{G}}_{\mathrm{R,A}}, \\ \tilde{\boldsymbol{G}}_{\mathrm{S}} &= \boldsymbol{G}_{\mathrm{S}} + \boldsymbol{G}_{\mathrm{R}} \cdot \boldsymbol{\Pi}_{\mathrm{R}} \cdot \tilde{\boldsymbol{G}}_{\mathrm{S}} + \boldsymbol{G}_{\mathrm{S}} \cdot \boldsymbol{\Pi}_A \cdot \tilde{\boldsymbol{G}}_{\mathrm{A}} + \boldsymbol{G}_{\mathrm{R}} \cdot \boldsymbol{\Pi}_{\mathrm{S}} \cdot \tilde{\boldsymbol{G}}_{\mathrm{A}}. \end{aligned} \tag{3.35}$$

See chapter 5 for a practical application of these relations.

3.5 Thermal Equilibrium

As discussed in the previous chapter a system in thermal equilibrium is characterized by the statistical density operator $\hat{\sigma} = \mathrm{e}^{-\beta \hat{H}}$ where $\beta = 1/T$ introduces the temperature T and $\hat{H}$ is the Hamilton operator. The statistical operator is thus identical to a time evolution operator in euclidean space allowing the statistical weight entering the path integral representation (3.7) to be rewritten as

$$\sigma(\varphi_0, \varphi_1) = \langle \varphi_1 | \mathrm{e}^{-\beta \hat{H}} | \varphi_0 \rangle = \int_{0 \to -\mathrm{i}\beta} [\mathrm{D}\varphi] \mathrm{e}^{-S_E} \Big|_{\varphi_0 = \varphi_1}. \tag{3.36}$$

where S_E is the euclidean action of the theory along the strip $0 \to -\mathrm{i}\beta$ of the imaginary axis in the complex time plane:

$$S_E = \int_0^\beta \mathrm{d}\tau \mathscr{L}(\mathrm{i}\tau) \tag{3.37}$$

The statistical weight can therefore be interpreted as a euclidean branch $0 \to -\mathrm{i}\beta$ of the complex time contour ζ as depicted in figure 3.3. The path integral in thermal equilibrium has the following explicit form with the boundary condition $\varphi_0 = \varphi_1$ imposed on the first and last configuration along the equilibrium contour. For time independent observables the real time part of the contour can be omitted to arrive at a theory formulated on the manifold of a euclidean space time with a compactified temporal dimension of extent β. Thermal equilibrium is a steady state of the system. Statistical fluctuations and dissipative processes must therefore be related to ensure the
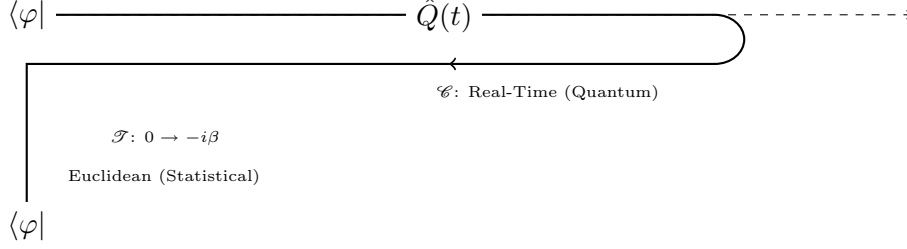
Figure 3.3: The Schwinger-Keldysh contour in thermal equilibrium. The amplitude $\sigma(\varphi_0, \varphi_1)$ is represented as an additional euclidean branch of the integration contour.

time independence of the thermal distribution which leads to an additional constraint for the Greens functions of the system called the Kubo-Martin-Schwinger (KMS) condition:

$$G_{12}(K) = \mathrm{e}^{-\beta\omega} G_{21}(K) \tag{3.38}$$

The constraint applies for bare as well as resummed propagators and can easily be checked in the former case by inserting the Bose distribution n_B into the general expression for bare bosonic propagators (3.22). It is straightforward to derive this condition in a position space representation of both off diagonal components of the propagator. Let $\hat{\varphi}(x)$ be the creation operator for a particle at the space-time position $x = (t, \boldsymbol{x}) \in \mathbb{R}^{d,1}$. The off-diagonal components of the propagator are given by the following expressions:

$$\mathrm{i}G_{21}(x, x') = \frac{1}{Z}\mathrm{Tr}\ \mathrm{e}^{-\beta\hat{H}}\hat{\varphi}(x)\hat{\varphi}(x'), \quad \mathrm{i}G_{12}(x, x') = \frac{1}{Z}\mathrm{Tr}\ \mathrm{e}^{-\beta\hat{H}}\hat{\varphi}(x')\hat{\varphi}(x). \tag{3.39}$$

Using the fact that the Boltzmann factor is a time evolution operator in euclidean space

$$\mathrm{e}^{-\beta\hat{H}}\varphi(t, \boldsymbol{x})\mathrm{e}^{\beta\hat{H}} = \varphi(t + \mathrm{i}\beta, \boldsymbol{x}) \tag{3.40}$$

as well as the rotation invariance of the system in thermal equilibrium the following identity is obtained:

$$G_{21}(x, x') = G_{12}((t + \mathrm{i}\beta, \boldsymbol{x}), x') \tag{3.41}$$

The identity is proven by inserting (3.40) into the definition of G_{12} in (3.39) and using the cyclicity of the trace. Upon performing the Fourier transform to a momentum space representation the Kubo-Martin Schwinger condition in the form (3.38) is obtained.

3.6   Application to Yang-Mills Theory

In the final section of this chapter the application of the previously introduced techniques to Yang-Mills theory is discussed. The Feynman rules for Yang-Mills theory in a generic non-equilibrium setting are obtained along the lines discussed for scalar theory. An additional complication arises when fixing to a specific gauge by the introduction of auxiliary ghost fields since these degrees of freedom can not be viewed as physical plasma constituents. A covariant gauge [22, 23] is assumed throughout this section. The building blocks for perturbation theory in a generic non-equilibrium system are briefly summarized in the following:

1. *Gluon Propagator*

   The bare gluon propagator $\boldsymbol{G}_{\mu\nu}^{ab}$ in a general covariant gauge with gauge parameter λ takes the following form [24]

   $$i\boldsymbol{G}_{\mu\nu}^{ab}(K) = \delta_{ab}\left\{\left[g_{\mu\nu} + (\lambda-1)\frac{K_\mu K_\nu}{K^2}\right]\boldsymbol{G}^{\mathrm{vac}} - P_{T\mu\nu}\boldsymbol{G}^{\mathrm{med}}\right\}, \tag{3.42}$$

   using the components of the bare scalar boson propagator introduced in (3.22). P_T is the transverse projector defined below.

2. *Ghost Propagator*

   A gauge fixing is imposed by the introduction of an auxiliary adjoint ghost field [17]. The propagator for each component of the ghost field is identical to the scalar boson propagator (3.22) at vanishing temperature,

   $$\boldsymbol{S}^{ab} = -i\delta_{ab}\boldsymbol{G}^{\mathrm{vac}}, \tag{3.43}$$

   since ghost particles can not be interpreted as physical plasma constituents and are not included in the density matrix of the system [25, 26].

3. *Interaction Vertices*

   The 3- and 4-vertices for the gluon self-interaction as well as the ghost-gluon vertex are identical to their vacuum counterparts [18] on the forward part of the contour. Type 2 vertices differ by an opposite sign.

A momentum space expansion is performed by drawing all topologically different diagrams and summing over all possible combinations of type 1 and 2 vertices which are joined by the appropriate entries of the bare real time propagators. Momentum conservation is imposed at every vertex, and an integration is performed over the remaining unconstrained momenta appearing in the propagators. A factor g is included for every ghost-gluon and gluon 3-vertex while a factor of g^2 is included for every 4-vertex. The order in g is the order of the expansion. The results from naive perturbation theory are unreliable and typically gauge dependent due to the appearance of characteristic momentum scales involving the coupling constant in many media. In thermal equilibrium and anisotropic media (see chapter 5) the problem is remedied by performing a *loop expansion* using resummed propagators and vertices as building blocks. The resummed propagators are obtained from the Schwinger Dyson equation (3.32) truncated to the required order of the expansion. This resummation is discussed in some detail in the following, assuming a thermal equilibrium, i.e. $f(\boldsymbol{p}) = n_B(\boldsymbol{p})$, for the remainder of this section. Using the previously introduced building blocks of bare perturbation theory the resummed retarded gluon propagator in a covariant gauge is obtained to leading order as

$$G_R^{\mu\nu}(K) = \frac{1}{K^2 - \Pi_T}P_T^{\mu\nu} + \frac{1}{K^2 - \Pi_L}P_L^{\mu\nu} - \frac{\lambda}{K^4}K^\mu K^\nu \tag{3.44}$$

where the projectors on longitudinal and transverse components are defined via:

$$P_T^{00} = P_T^{0i} = 0, \quad P_T^{ij} = \delta_{ij} - \frac{K^i K^j}{k^2}, \quad \text{and} \quad P_L^{\mu\nu} = -g^{\mu\nu} + \frac{K^\mu K^\nu}{K^2} - P_T^{\mu\nu}. \tag{3.45}$$

In thermal equilibrium the Lorentz symmetry of Yang-Mills theory at $T = 0$ is broken by the appearance of a symmetry vector corresponding to the 4-velocity of the plasma. It is natural to expect the appearance of thermal masses since the propagator has to be expanded in an extended tensor basis including longitudinal as well as transverse components to take into account the broken Lorentz symmetry. Using the fact that the system is homogeneous and employing the KMS-condition the remaining propagators are obtained as:

$$\tilde{G}_A = \tilde{G}_R^* \quad \text{and} \quad \tilde{G}_S = -2i(e^{\beta\omega} + 1)n_B(\omega)\text{Im}G_R. \tag{3.46}$$

The retarded self energy has been decomposed into longitudinal and transverse components

$$\Pi_R = P_L\Pi_L + P_T\Pi_T \tag{3.47}$$

which take the following form for soft external momentum $K \ll T$ where loop integrations are dominated by hard internal momenta $\sim T$:

$$\Pi_L = m_D^2 \left[1 - \frac{\omega^2}{k^2}\right] \left[1 - \frac{\omega}{2k} log \frac{\omega + k}{\omega - k}\right], \quad \Pi_T = \frac{m_D^2}{2} \frac{\omega^2}{k^2} \left[1 - \frac{\omega^2 - k^2}{2\omega k} \log \frac{\omega + k}{\omega - k}\right]. \tag{3.48}$$

The advanced and symmetric self energies are obtained from the KMS condition and the relation

$$\Pi_A(K) = \Pi_R^*(K). \tag{3.49}$$

An analysis of the dispersion relations of the gluon at leading order leads to the identification of the following characteristic scales of the Yang-Mills plasma:

1. *Hard Momentum Scale: $k \sim T$*

   The characteristic momentum scale for gluons in a Yang-Mills plasma corresponds to the temperature T of the medium. The corresponding length scale $1/T$ is the average inter particle spacing.

2. *Electric Scale: $k \sim gT$*

   The thermal mass of soft longitudinal gluons is given by the Debye mass $m_D \sim gT$. The exchange of longitudinal gluons is significantly suppressed below this threshold which translates into a suppression of electrical interactions at distances larger than $1/m_D$.

3. *Magnetic Scale: $k \sim g^2T$*

   Magnetic interactions, which are the most far reaching interaction in the Yang-Mills plasma, experience a dynamical screening over distances larger than $1/g^2T$.

It is important to discuss the appearance of plasma scales involving the coupling constant in more detail at this point. Feynman diagrams involving these scales acquire an additional dependence on the coupling constant which compromises a naive perturbative expansion in the coupling constant. It is found in particular that the resummed propagators and vertices obtained from the tower of Schwinger-Dyson relations are of the same order as the bare ones. It is therefore necessary to expand in the resummed Greens functions and vertices, i.e. to perform a loop expansion. Systematical use can be made of the fact that loop integrations for Feynman diagrams with soft external momenta are dominated by contributions from the hard momentum region. It is thus possible to expand integrands in the quotients of external and internal momenta. The resulting expansion scheme is referred to as *hard thermal loop* (HTL) approximation and discussed for the euclidean theory in [18]. For a discussion of HTL improved perturbation theory in the real-time formalism see [27]. Details of this scheme will be highlighted as required in following chapters.

4 QUARKONIA AT FINITE TEMPERATURE

Facts are the air of scientists.
Without them you can never fly.

John Dewey

While attempts to calculate the resonances of bound states in a quark-gluon plasma have a long history, a definition of the static potential in a thermal medium from first principles has only been attempted recently. In the following the techniques presented in the preceding chapter are applied to derive a leading-order expression for the static potential in a generic (non-)equilibrium plasma and to obtain the quarkonium spectral function in thermal equilibrium. The findings are discussed in detail in the following articles: [28, 29, 30, 31].

4.1 A Model System for Confinement

Mesons constituted by a pair of heavy quarks of the same flavor, referred to as *quarkonia*, are the most simple bound states of QCD. The symmetric nature of these systems and the high mass of their constituents make them amenable to the description by a nonrelativistic Schrödinger equation

$$i\partial_t \psi(\boldsymbol{r}) = \left(-\frac{\triangle_r}{M} + V(\boldsymbol{r})\right)\psi(\boldsymbol{r}) \tag{4.1}$$

where M is the mass of the charm or bottom quark and ψ the quark wave-function. Due to the slow movement of constituent quarks the effective potential $V(\boldsymbol{r})$ is identical to the static potential introduced in (2.22) allowing quarkonium resonances to be related directly to the confinement properties of the underlying theory. The discovery of the J/ψ in 1974 [32, 33] and subsequent confirmation of QCD predictions for the effective potential was a key element in establishing QCD as the correct theory for the strong interactions. Ever since their discovery quarkonia have retained their role as a model system for the confinement properties of QCD and are expected to provide valuable clues on the nature of the deconfinement transition observed in heavy-ion collisions. In 1987 Matsui and Satz [34] proposed the following effective potential at finite temperature assuming the Schrödinger equation (4.1) to remain valid in a thermal setting

$$V(r) = -\frac{g^2 \mathrm{C_F}}{4\pi} \frac{\mathrm{e}^{-m_D r}}{r} \tag{4.2}$$

where $r = |\boldsymbol{r}|$ is the distance between the constituent quarks and m_D the Debye mass. The flux tube, connecting the constituent quarks is assumed to vanish while the Coulomb component of the potential, which arises from single gluon exchange, takes the form of a Yukawa potential due to the generation of a gluon mass m_D beyond deconfinement. Since the leading order Debye mass is of the form $m_D \sim gT$, the screening increases with the temperature leading to a widening of the quarkonium resonance which is referred to as the *melting of quarkonium*.

4.2   The Static Potential in a Thermal Medium

It remains unclear to the present day how to derive the binding energy and decay width of bound state resonances in a QCD-plasma from first principles. In a recent series of papers [28, 37, 29, 35] the heavy quark static potential was extended to thermal media using the Schrödinger equation for the quarkonium correlator as a starting point. Formally the time evolution of the quarkonium correlator

$$\mathrm{i}C_{21}(t,\boldsymbol{r}) = \quad\underbrace{\qquad}\quad = \int \mathrm{d}^3 x \left\langle \overline{\psi}(t, \frac{\boldsymbol{x}+\boldsymbol{r}}{2})\gamma^{\mu} W \psi(t, \boldsymbol{x}-\frac{\boldsymbol{r}}{2})\overline{\psi}(0,\boldsymbol{0})\gamma_{\mu}\psi(0,\boldsymbol{0}) \right\rangle \qquad (4.3)$$

is expected to be governed by the following equation and initial condition which can easily be verified in NRQCD at leading order:

$$\mathrm{i}\partial_t C_{21}(t,\boldsymbol{r}) = \left(2M - \frac{\triangle_{\boldsymbol{r}}}{M} + V(t,\boldsymbol{r}) \right) C_{21}(t,\boldsymbol{r}) \quad \text{with} \quad \mathrm{i}C_{21}(0,\boldsymbol{r}) = -6N\delta^{(3)}(\boldsymbol{r}). \qquad (4.4)$$

M denotes the mass of the constituent quarks and W represents a straight Wilson line connecting the quark fields at time t. The potential $V(t,\mathbf{r})$ is a complex quantity with the imaginary part parametrizing the damping effects induced by the medium to generalize the concept of a potential to a thermal setting. In the limit of infinite quark masses the amplitude $C_{21}(t,\mathbf{r})$ is represented by the expectation value of a Wilson loop of spatial extent $\mathbf{r}$ and temporal extent t after introduction of another point-splitting. Note that the correlator $C_{21}(t,\boldsymbol{r})$ can be replaced with the time ordered correlator $C_{11}(t,\boldsymbol{r})$ at positive times to avoid ambiguities due to time and path ordering:

$$\mathrm{i}C_{11}(t,\boldsymbol{r}) = \frac{1}{N}\mathrm{Tr} < \boxed{\qquad} > . \qquad (4.5)$$

The following Schrödinger equation ensues after scaling out the phase factor associated with the quark mass:

$$\mathrm{i}\partial_t C_{11}(t,\mathbf{r}) = V(t,\mathbf{r})C_{11}(t,\mathbf{r}). \qquad (4.6)$$

The real-time static potential is subsequently defined as the infinite time limit of the potential $V(t,\mathbf{r})$:

$$V(\boldsymbol{r}) = \lim_{t\to\infty} V(t,\boldsymbol{r}) = \lim_{t\to\infty} \frac{\mathrm{i}\partial_t C_{11}(t,\mathbf{r})}{C_{11}(t,\mathbf{r})}. \qquad (4.7)$$

It is important to emphasize that the relation (2.21) can *not* simply be continued to Minkowski space. The real-time definition of the static potential is motivated instead by noting that a non-vanishing potential in the infinite time limit will generate a dominant peak in the spectral function of the static correlator at low energies [37]. In the following section a leading order expression for the real-time static potential in an arbitrary medium is derived by expanding the Wilson Loop (4.5) with respect to the gauge coupling. It is shown that the real-time static potential to leading order consists of two components obtained as integral transforms of the retarded and symmetric HTL gluon propagators. In thermal equilibrium these two components will translate into a real and imaginary part of the potential parametrizing the binding and decay of the quarkonium ground state.

4.3   Expansion of the Wilson Loop

For convenience the Wilson loop will be assumed to be oriented in the z-direction for the following steps of the derivation. The series of diagrams resulting from an expansion of the Wilson Loop to first order in g^2 is briefly listed below with $\tilde{G}$ denoting the resummed gluon propagator in the medium under consideration. The following contributions from the spatial Wilson lines are readily summed up to a compact expression $[K = (\omega, \boldsymbol{k})]$

$$\frac{1}{N}\mathrm{Tr}\,\langle \boxed{} + \boxed{} + \boxed{} \rangle$$

$$= 2g^2\mathrm{C_F}\int \frac{\mathrm{d}^4K}{(2\pi)^4}\frac{\mathrm{e}^{-\mathrm{i}\omega t}-1}{(k^3)^2}(1-\cos k^3 r)\mathrm{i}\tilde{G}_{11}^{33}(K),$$

while the diagrams containing only contributions from the temporal Wilson lines can be summed up in an analogous fashion introducing the longitudinal propagator into the expression for the real time static potential:

$$\frac{1}{N}\mathrm{Tr}\,\langle \boxed{} + \boxed{} + \boxed{} \rangle$$

$$= 2g^2\mathrm{C_F}\int \frac{\mathrm{d}^4K}{(2\pi)^4}\frac{\mathrm{e}^{\mathrm{i}k^3 r}-1}{\omega^2}(1-\cos \omega t)\mathrm{i}\tilde{G}_{11}^{00}(K).$$

The final set of diagrams consists of the cusp contributions correlating the spatial and temporal Wilson lines which add up to the following expression:

$$\frac{1}{N}\mathrm{Tr}\,\langle \boxed{} + \boxed{} + \dots \rangle$$

$$= 4g^2\mathrm{C_F}\int \frac{\mathrm{d}^4K}{(2\pi)^4}\frac{1}{\omega k^3}(1-\cos \omega t)(1-\cos k^3 r)\mathrm{i}\tilde{G}_{11}^{03}(K).$$

Summing up all diagrams and employing the definition (4.7) the potential $V(\boldsymbol{r})$ is represented by the leading order expression listed in the following:

$$\begin{aligned}V(\boldsymbol{r}) &= \lim_{t\to\infty} 2g^2\mathrm{C_F}\int \frac{\mathrm{d}^4K}{(2\pi)^4}\{\omega\frac{\mathrm{e}^{-\mathrm{i}\omega t}}{(k^3)^2}(1-\cos k^3 r)\mathrm{i}G_{11}^{33}(K)\\ &\quad -\frac{\mathrm{e}^{\mathrm{i}k^3 r}-1}{\omega}\sin \omega t\, G_{11}^{00}(K) + \frac{2\sin \omega t}{k^3}(\cos k^3 r - 1)G_{11}^{03}(K)\}.\end{aligned}$$

The sum is easily reduced to a more simple form by employing the following representation of the δ-distribution

$$\delta(\omega) = \lim_{t\to\infty}\frac{\sin \omega t}{\pi\omega} \tag{4.8}$$

leading to a generic expression for the real-time static potential in arbitrary (non-)equilibrium systems upon removing the restriction that the Wilson loop points in the z-direction:

$$V(\boldsymbol{r}) = g^2\mathrm{C_F}\int \frac{\mathrm{d}^3k}{(2\pi)^3}(1-\mathrm{e}^{\mathrm{i}\boldsymbol{k}\cdot\boldsymbol{r}})\tilde{G}_{11}^{00}(\omega = 0, \boldsymbol{k}). \tag{4.9}$$

4.4   Static Potential and Relation to the Free Energy

To obtain an explicit expression for the real-time static potential in thermal equilibrium, it is convenient to decompose the propagator $\tilde{\mathbf{G}}_{11}$ into the retarded and symmetric propagator (3.12):

$$\tilde{\mathbf{G}}_{11} = \mathrm{Re}\tilde{\mathbf{G}}_R + \frac{1}{2}\tilde{\mathbf{G}}_S. \tag{4.10}$$

The retarded propagator $\tilde{\mathbf{G}}_R$ in thermal equilibrium is given by the following expression [18, 36] in a general covariant gauge

$$\tilde{G}_R^{\mu\nu}(K) = \frac{1}{K^2 - \Pi_T}P_T^{\mu\nu} + \frac{1}{K^2 - \Pi_L}P_L^{\mu\nu} - \frac{\lambda}{K^4}K^\mu K^\nu \tag{4.11}$$

where the longitudinal and transversal self-energies [28]

$$\Pi_L(K) = m_D^2\left[1 - \frac{\omega^2}{k^2}\right]\left[1 - \frac{\omega}{2k}\log\frac{\omega+k}{\omega-k}\right] \quad \Pi_T(K) = \frac{m_D^2}{2}\frac{\omega^2}{k^2}\left[1 - \frac{\omega^2-k^2}{2\omega k}\log\frac{\omega+k}{\omega-k}\right] \tag{4.12}$$

develops an imaginary part for $\omega < k$. The physical branch of the logarithm is $\mathrm{Im}\log(\omega+k)/(\omega-k) = -\pi\Theta(k^2-\omega^2)$. The transversal and longitudinal projectors $P_T^{\mu\nu}$ and $P_L^{\mu\nu}$ are listed in (3.45). The symmetric propagator is readily obtained from the retarded propagator by employing the Kubo-Martin-Schwinger condition which can be written in the form presented below using the constraint (B.2) as well as the homogenity of the system:

$$\tilde{\mathbf{G}}_S(K) = 2\mathrm{i}n_{\mathrm{B}}(\omega)(\mathrm{e}^{\beta\omega} + 1)\mathrm{Im}\tilde{\mathbf{G}}_R(K). \tag{4.13}$$

The analytic expression for the real-time static potential is finally obtained by inserting the static limit of the propagators into (4.9) with the real part corresponding to the Debye screened potential (4.2):

$$
\begin{aligned}
V(\mathbf{r}) &= g^2\mathrm{C}_{\mathrm{F}}\int\frac{\mathrm{d}^3k}{(2\pi)^3}\left[1 - \cos k^3 r\right]\left(\underbrace{\frac{1}{k^2 + m_D^2}}_{\text{Retarded}} - \mathrm{i}\underbrace{\frac{\pi m_D^2}{\beta}\frac{1}{k(k^2 + m_D^2)^2}}_{\text{Symmetric}}\right)\\
&= \underbrace{-\frac{g^2\mathrm{C}_{\mathrm{F}}}{4\pi}\left(m_D + \frac{\mathrm{e}^{-m_D r}}{r}\right)}_{\mathrm{Re}(V),\text{Retarded contribution}} - \mathrm{i}\underbrace{\frac{g^2 T\mathrm{C}_{\mathrm{F}}}{2\pi}\int_0^\infty\frac{\mathrm{d}z z}{(z^2+1)^2}\left(1 - \frac{\sin(z\,m_D r)}{z\,m_D r}\right)}_{\mathrm{Im}(V),\text{Symmetric contribution}}
\end{aligned} \tag{4.14}
$$

A calculation of the corresponding potential for a $q\bar{q}$-pair transforming in the adjoint representation is in preparation [42]. Being the integral transform (4.9) of the symmetric propagator the imaginary part is associated with Landau damping. It is important to emphasize that, while the analytic continuation of the potential $V(t = -\mathrm{i}\beta, \mathbf{r})$ is identical to the singlet free energy, the real-time static potential does not correspond to this quantity. The static potential at finite temperature, as defined here from first principles, can in fact not be related in a straightforward way to an analogous quantity in euclidean space. It is nevertheless instructive to measure the singlet free energy in a non-perturbative setting to estimate the extent to which the full real part of the static $q\bar{q}$-potential will deviate from the leading-order result. This measurement is presented in chapter 6.
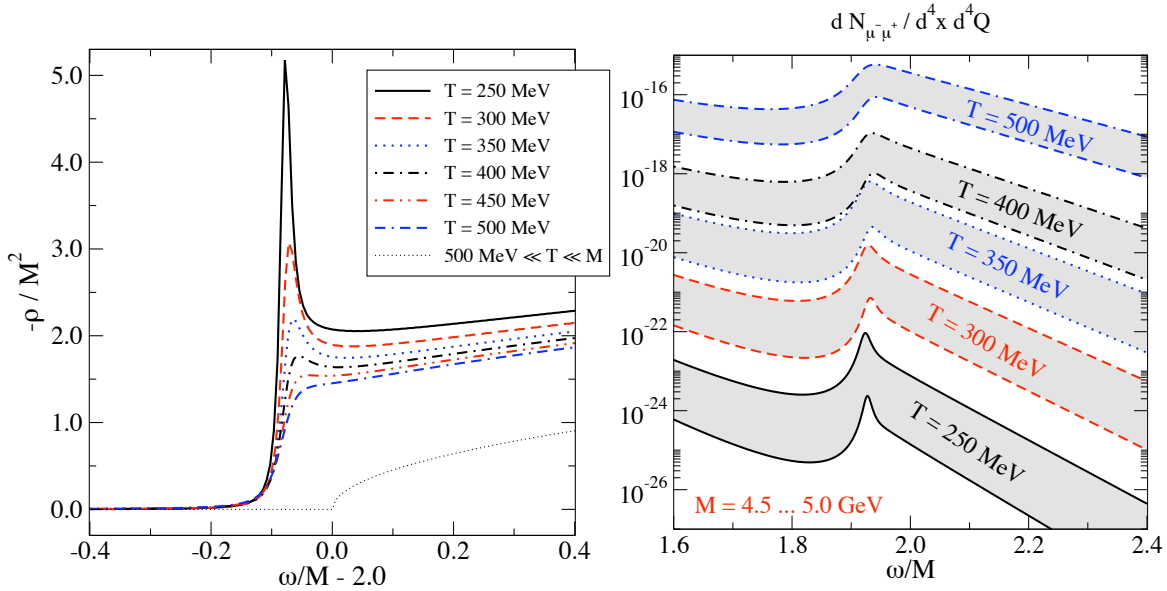
Figure 4.1: *Left:* Spectral function for bottomonium at rest obtained from a numerical solution of the Schrödinger equation (4.4) using the Real-Time Static Potential [37]. *Right:* The expected quarkonium peak in the $\mu^-\mu^+$-emission spectrum from dissociation of quarkonium in the vector channel [38].

4.5 Quarkonium Spectral Function and Physical Signatures

To obtain the spectral function $\rho(\omega)$ for quarkonium at rest the real-time static potential is reinserted into the finite-mass Schrödinger equation (4.4) to calculate the correlator:

$$\mathrm{i}C_{21}(t,\mathbf{0}) = \qquad . \tag{4.15}$$

The spectral function is subsequently obtained from the correlator via [37]:

$$\rho(\omega) = \frac{\mathrm{i}}{2}\int_{-\infty}^{\infty}\mathrm{d}t e^{\mathrm{i}\omega t}\left\{C_{21}(t,\mathbf{0}) - C_{12}(t,\mathbf{0})\right\} = \frac{1}{2}\left(1 - e^{-\beta\omega}\right)\int_{-\infty}^{\infty}\mathrm{d}t e^{\mathrm{i}\omega t}\mathrm{i}C_{21}(t,\mathbf{0}) \tag{4.16}$$

The numerical solution of the Schrödinger equation (4.4) and the extraction of the correlator (4.15) is discussed in [37] (see also chapter 5). Fig. 4.1 (left) depicts the shape of the bottomonium resonance assuming a bottom quark mass of $m_b = 4.5\,GeV$. The melting of the resonance peak with increasing temperature is induced by the imaginary part of the potential (4.14). The quarkonium spectral function ρ_V in the vector channel is directly related to the dilepton rate due to dissociation of quarkonium at rest [39, 40, 41]

$$\frac{\mathrm{d}N_{l^-l^+}}{\mathrm{d}^4x\mathrm{d}^4K} = \frac{2c^2e^4}{3(2\pi)^5\omega^2}\left(1 + \frac{2m_l^2}{\omega^2}\right)\left(1 - \frac{4m_l^2}{\omega^2}\right)^{\frac{1}{2}}n_{\mathrm{B}}(\omega)(-\rho^V(\omega)). \tag{4.17}$$

which has been calculated in [38]. The electric charge of the lepton family l is denoted as e, m_l is the lepton mass and $c \in \{-\frac{1}{3}, \frac{2}{3}\}$ is the electromagnetic coupling of the constituent quarks. The expected quarkonium peak in the $\mu^-\mu^+$-emission spectrum is shown in fig. 4.1 (right) for bottomonium.

5 ANISOTROPIC QUARK-GLUON PLASMA

*In physics you don't have to go around making trouble for
yourself. Nature will do this for you.*

Frank Wilczek

A plasma with an anisotropy imposed on the momentum distribution of the system is considered
and the real time static potential for quarkonia studied. The distribution function is normalized so
as to preserve the particle number in an ideal gas as required in the Schwinger-Keldysh formalism.
Contrary to recent findings without this normalization, a weak anisotropy does not lead to an
increase in the melting temperature for bound states. To test for the maximal effect, the gluonic
medium is also investigated in the limit of an asymptotically strong anisotropy. The spectral func-
tion of quarkonium is calculated for this case and found to be in remarkable qualitative agreement
with the corresponding results for an isotropic medium. These findings were published in [43].
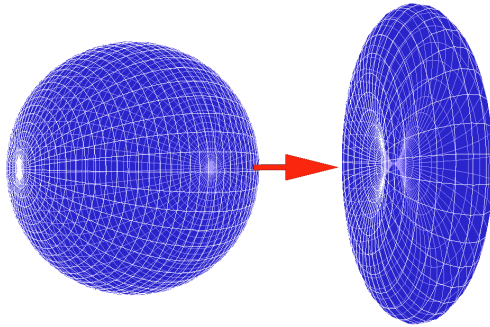

Figure 5.1: Comparison of the angular momentum distribution $f(\boldsymbol{k})$ at a fixed momentum k in an isotropic
medium (left) and the deformed angular distribution in an anisotropic gluonic medium with $\xi > 0$ (right).

5.1 Model System and Purpose of the Calculation

The QCD-plasma with an anisotropic momentum distribution has been subject to several recent
investigations as a simple model for the early stages of heavy ion collisions [44, 45, 46]. Such a
system is obtained by replacing the isotropic momentum space distribution functions by

$$f(\boldsymbol{k}, \xi) = N(\xi)\, f_{\text{iso}}\left(\sqrt{\boldsymbol{k}^2 + \xi(\boldsymbol{k} \cdot \boldsymbol{n})^2}\right), \tag{5.1}$$

which removes modes with momentum components along the direction of the anisotropy, $\boldsymbol{n}$. Here, ξ
parametrizes the strength of the anisotropy and $N(\xi)$ is a normalization factor with $N(\xi = 0) = 1$.
Interest has particularly focused on the question how such an anisotropy influences the dissociation
of non-relativistic quarkonium systems within potential model studies [36, 47, 48]. The general
approach in those works was to consider small anisotropies $\xi \leq 1$ and to calculate the correction
to the propagators and the static potential to first order in ξ. The effect of the anisotropy on the
normalization was neglected, i.e. $N(\xi) \equiv 1$ in those works, and with the exception of [49] all employ
the equilibrium Kubo-Martin-Schwinger (KMS) condition, which strictly speaking does not hold in

the anisotropic case. The general conclusion of those investigations was that the anisotropy tends to decrease the effect of Landau damping and thus to increase the dissociation temperature.
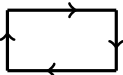
In this paper the extent is assessed to which these results are modified by taking a ξ-dependent normalization factor into account and solving again the Dyson-Schwinger equations for the non-equilibrium system. This is motivated by the fact that modifying only the argument of the isotropic distribution function in (5.1) simply removes particles/modes with momentum components along the anisotropy direction, i.e. the plasma gets diluted with growing ξ. The momentum distribution defines the thermal parts of the bare propagators in the real-time formalism and thus parametrizes a gas of non-interacting particles. Hence, the anisotropy must not affect the average number density of particles. This results in a normalization condition for all ξ [50, 45],

$$n = \int \frac{\mathrm{d}^3 \boldsymbol{p}}{(2\pi)^3} f_{\mathrm{iso}}(\boldsymbol{p}) \stackrel{!}{=} \int \frac{\mathrm{d}^3 \boldsymbol{p}}{(2\pi)^3} f(\boldsymbol{p}, \xi) \, , \tag{5.2}$$

with the solution $N(\xi) = \sqrt{1 + \xi}$. For example, the integral over the Bose distribution function, $f_{\mathrm{iso}}(\boldsymbol{p}) = n_B(\boldsymbol{p})$, evaluates to $n = 3.606 \, T^3/(2\pi)^2$. Using $N(\xi) = 1$ for $\xi \neq 0$ gives instead $n = \{2.55, 1.09, 0.3\} \, T^3/(2\pi)^2$ for $\xi = \{1, 5, 100\}$, respectively. Even for "small" anisotropy $\xi = 1$, the dilution amounts to a significant 30% and affects observables. It is found that the modified normalization largely compensates the effects observed previously, such that for $\xi = 1$ there is little difference in the static potential between the isotropic and anisotropic cases. To underline this finding the 'maximal anisotropy effect' is studied by considering the limit $\xi \to \infty$, in which the plasma is confined to a thermal plane in momentum space perpendicular to the symmetry axis of the system. Somewhat surprisingly, also in this case the quarkonium spectral function is qualitatively in agreement with the isotropic situation. For simplicity a purely gluonic system is considered, the inclusion of light fermions is straightforward and will merely introduce a modification to self energy prefactors [51].

5.2   The Static Potential, Propagator and Self Energy

For our calculations we use the Keldysh-Schwinger real time formalism [21], similar to [49]. There one considers matrices of correlation functions, C_{ij}, with indices $i, j \in \{1, 2\}$ denoting the forward and backward portions of the Keldysh contour. The real time static potential in a thermal medium may be defined through the quarkonium Wightman function in the infinite quark mass limit, i.e. the Wilson loop in Minkowski time evaluated in a thermal bath [28] , whose time evolution is governed by a 'Schrödinger equation':

$$\mathrm{i}C_{21}(t, \boldsymbol{r}) = \frac{1}{N} \mathrm{Tr} < \boxed{\quad} > , \qquad \mathrm{i}\partial_t C_{21}(t, \mathbf{r}) = V(t, \boldsymbol{r}) \, C_{21}(t, \mathbf{r}) \, . \tag{5.3}$$

The static potential corresponds to the large time limit of this evolution, where the Wightman function may be replaced by C_{11},

$$V(\boldsymbol{r}) = \lim_{t \to \infty} V(t, \boldsymbol{r}) = \lim_{t \to \infty} \frac{\mathrm{i}\partial_t C_{11}(t, \mathbf{r})}{C_{11}(t, \mathbf{r})} \, , \tag{5.4}$$

and to leading order in perturbation theory is equivalent to a matching coefficient appearing in a non-relativistic effective theory for finite temperatures [52, 35, 53]. Calculating the Feynman

diagrams corresponding to the Wilson loop through order g^2 in the real time formalism, one finds the generic expression for the potential in an arbitrary (non-)equilibrium system [31],

$$
\begin{aligned}
V(\boldsymbol{r}) &= g^2 C_F \int \frac{\mathrm{d}^3 \boldsymbol{k}}{(2\pi)^3} (1 - \mathrm{e}^{\mathrm{i}\boldsymbol{k}\cdot\boldsymbol{r}}) \tilde{G}_{11}^{00}(\omega = 0, \boldsymbol{k}) \\
&= g^2 C_F \int \frac{\mathrm{d}^3 \boldsymbol{k}}{(2\pi)^3} (1 - \mathrm{e}^{\mathrm{i}\boldsymbol{k}\cdot\boldsymbol{r}}) \left(\frac{1}{2} \tilde{G}_S^{00} + \mathrm{Re}\tilde{G}_R^{00} \right) .
\end{aligned}
\tag{5.5}
$$

The tilde indicates a HTL-resummation of the gluon propagator. Thus we need to evaluate the resummed retarded and symmetric propagators for the various degrees of anisotropy we wish to discuss. These are solutions to the Dyson-Schwinger equations,

$$
\begin{aligned}
\tilde{\boldsymbol{G}}_R &= \boldsymbol{G}_R + \boldsymbol{G}_R \cdot \boldsymbol{\Pi}_R \cdot \tilde{\boldsymbol{G}}_R, \\
\tilde{\boldsymbol{G}}_S &= \boldsymbol{G}_S + \boldsymbol{G}_R \cdot \boldsymbol{\Pi}_R \cdot \tilde{\boldsymbol{G}}_S + \boldsymbol{G}_S \cdot \boldsymbol{\Pi}_A \cdot \tilde{\boldsymbol{G}}_A + \boldsymbol{G}_R \cdot \boldsymbol{\Pi}_S \cdot \tilde{\boldsymbol{G}}_A .
\end{aligned}
\tag{5.6}
$$

The bold face notation indicates matrices in Lorentz and colour space. In the following all colour matrices are $\sim \delta_{ab}$ and will be suppressed to simplify the notation. The retarded self energy for an anisotropic plasma has been calculated in HTL-approximation in [54], and the retarded propagator in a general covariant gauge in [36]. The resummed retarded gluon propagator in a general covariant gauge can be written in the form

$$
\tilde{G}_R^{\mu\nu}(K) = \Delta_A[A^{\mu\nu} - C^{\mu\nu}] + \Delta_G \left[(K^2 - \alpha - \gamma)\frac{\omega^4}{K^4}B^{\mu\nu} + (\omega^2 - \beta)C^{\mu\nu} + \delta\frac{\omega^2}{K^2}D^{\mu\nu} \right] - \frac{\lambda}{K^4}K^\mu K^\nu .
\tag{5.7}
$$

Here the symmetry vector $n^\mu = (0, \boldsymbol{n})$ represents the anisotropy, $K = (\omega, \boldsymbol{k})$, λ is the gauge parameter and the electric and magnetic propagators are

$$
\begin{aligned}
\Delta_G^{-1} &= (K^2 - \alpha - \gamma)(\omega^2 - \beta) - \delta^2[\boldsymbol{k}^2 - (n \cdot K)^2] , \\
\Delta_A^{-1} &= K^2 - \alpha .
\end{aligned}
\tag{5.8}
$$

Explicit expressions for the tensors $A - D$ and the structure functions $\alpha(K, \xi) - \delta(K, \xi)$ for arbitrary anisotropies are listed in Eqs. (2–5) in [36] and Eqs. (B1–B4) in [44], respectively. Note however, that the structure functions given there are for $N(\xi) = 1$ and need to be multiplied by $N(\xi) = \sqrt{1 + \xi}$ for the purposes of this study. Since the interest is in applications for potential models, it is expedient to take the static limit $\omega \to 0$ already at this stage to facilitate the calculations. In this case the bare symmetric propagator vanishes and, using the fact that the retarded and advanced propagators are related via $\tilde{G}_A^{\mu\nu} = (\tilde{G}_R^{\nu\mu})^*$ in a general homogeneous system [21], the second of equations (5.6) simplifies to (see also [51])

$$
\tilde{\boldsymbol{G}}_S = \tilde{\boldsymbol{G}}_R \cdot \boldsymbol{\Pi}_S \cdot \tilde{\boldsymbol{G}}_R^* .
\tag{5.9}
$$

The propagator in the static limit is (with the notation $k^2 \equiv \boldsymbol{k}^2, \cos\theta_k \equiv \boldsymbol{n} \cdot \boldsymbol{k}/k$)

$$
\begin{aligned}
\tilde{G}_R^{\mu\nu}(\omega = 0, \boldsymbol{k}) &= \Delta_A[C^{\mu\nu} - A^{\mu\nu}] + \Delta_G \left[(k^2 + m_\alpha^2 + m_\gamma^2)B^{\mu\nu} - (k^2 + m_\beta^2)C^{\mu\nu} + \mathrm{i}\frac{m_\delta^2}{\sin\theta_k}D^{\mu\nu} \right] \\
&\quad - \frac{\lambda}{k^4}K^\mu K^\nu
\end{aligned}
\tag{5.10}
$$

with now
$$\Delta_{\text{A}}^{-1} = k^2 + m_\alpha^2, \qquad \Delta_{\text{G}}^{-1} = (k^2 + m_\alpha^2 + m_\gamma^2)(k^2 + m_\beta^2) - m_\delta^4 \ . \tag{5.11}$$
The tensor basis is simplified and takes the form
$$\begin{aligned}
A^{0\mu}(\boldsymbol{k}) = A^{\mu 0}(\boldsymbol{k}) = 0 \quad A^{ij}(\boldsymbol{k}) = \delta_{ij} - k^i k^j / k^2 \qquad B^{\mu\nu}(\boldsymbol{k}) = \delta_{\mu 0}\delta_{\nu 0} \\
C^{0\mu}(\boldsymbol{k}) = C^{\mu 0}(\boldsymbol{k}) = 0 \qquad C^{ij}(\boldsymbol{k}) = \tilde{n}^i \tilde{n}^j \qquad D^{\mu\nu}(\boldsymbol{k}) = \delta_{\mu 0}\tilde{n}^\nu + \delta_{\nu 0}\tilde{n}^\mu
\end{aligned} \tag{5.12}$$

with $\tilde{x}^i = A^{ij}x^j$. A rescaling of the tensors $\frac{\omega^2}{k^2}B^{\mu\nu} \to B^{\mu\nu}$, $\frac{\omega}{k^2}D^{\mu\nu} \to D^{\mu\nu}$, as well as $-\frac{\omega^2}{k^2}\Delta_G \to \Delta_G, -\Delta_A \to \Delta_A$ has been introduced with respect to (5.7,5.8) to keep all components of the retarded propagator explicitly finite in the static limit. The effective masses are the static limits of the structure functions [44],

$$m_\alpha^2 = \lim_{\omega\to 0} \alpha \ , \quad m_\beta^2 = \lim_{\omega\to 0} -\frac{k^2}{\omega^2}\beta \ , \quad m_\gamma^2 = \lim_{\omega\to 0} \gamma \ , \quad m_\delta^2 = \lim_{\omega\to 0} \frac{k^2 \sin\theta_k}{\omega}\text{Im}(\delta) \ . \tag{5.13}$$

5.3   Weak Anisotropy, $\xi \leq 1$

In order to discuss the effect of a weak anisotropy, the distribution function (5.1) is employed, including the non-trivial normalization with $N(\xi)$, and the resummed propagators expanded up to linear order in ξ. For the longitudinal component of the retarded propagator appearing in (5.5) the following form is derived

$$\tilde{G}_{\text{R}}^{00}(\omega = 0, \boldsymbol{k}) = \frac{k^2 + m_\alpha^2 + m_\gamma^2}{(k^2 + m_\alpha^2 + m_\gamma^2)(k^2 + m_\beta^2) - m_\delta^4} \ . \tag{5.14}$$

All ξ-dependence resides in the effective masses. To linear order the dimensionless combinations $\hat{m}_x^2 = m_x^2/m_D^2$ read

$$\hat{m}_\alpha^2 = -\frac{\xi}{3}\cos^2\theta_k, \qquad \hat{m}_\beta^2 = 1 + \xi(\cos^2\theta_k - \frac{1}{6}), \tag{5.15}$$

$$\hat{m}_\gamma^2 = \frac{\xi}{3}\sin^2\theta_k, \qquad \hat{m}_\delta^2 = -\xi\frac{\pi}{4}\sin\theta_k\cos\theta_k \ . \tag{5.16}$$

Note that $\hat{m}_\beta^2$ differs from the expression given in [44] due to the normalization factor $N(\xi) = \sqrt{1+\xi}$ in the distribution function (5.1). The retarded propagator to linear order then is

$$\tilde{G}_{\text{R}}^{00} = \frac{1}{k^2 + m_D^2} - \xi\frac{m_D^2}{(k^2 + m_D^2)^2}(\cos^2\theta_k - \frac{1}{6}) \ . \tag{5.17}$$

Expanding also the static potential, $V(\boldsymbol{r}) = V_0(r) + \xi V_1(\boldsymbol{r}) + \ldots$, the correction of the real part due to the anisotropy is found to be,

$$\text{Re}V_1(\boldsymbol{r}) = g^2 C_F m_D^2 \int \frac{\text{d}^3\boldsymbol{k}}{(2\pi)^3}(1 - \cos(\boldsymbol{k}\cdot\boldsymbol{r}))\frac{1}{(k^2 + m_D^2)^2}\left(\cos^2\theta_k - \frac{1}{6}\right). \tag{5.18}$$

For the imaginary part the symmetric propagator and the symmetric self-energy are needed in addition, cf. (5.9). In the static limit and for soft external momenta $k_i \ll p_i$ the latter takes the form [51]

$$i\Pi_{\text{S}}^{\mu\nu} = 8\pi g^2 N\frac{1}{k}\int \frac{d^3p}{(2\pi)^3}v_p^\mu v_p^\nu f(\boldsymbol{p})(1 + f(\boldsymbol{p} + \boldsymbol{k}))\delta(\boldsymbol{v}_p \cdot \boldsymbol{v}_k) \ . \tag{5.19}$$

Straightforward calculation gives the following expansion for the symmetric propagator

$$
\begin{aligned}
\tilde{G}_{\mathrm{S}}^{00} &= -\mathrm{i}\frac{2\pi}{k(k^2+m_D^2)^2}\frac{m_D^2}{\beta}\left(1+\xi\left[\frac{\pi^2-3\zeta(3)}{\pi^2}-\frac{3}{4}\sin^2\theta_k\right]\right)\\
&\quad +i\xi4\pi\frac{m_D^4}{\beta}\frac{1}{k(k^2+m_D^2)^3}(\cos^2\theta_k-\frac{1}{6})\,.
\end{aligned}
\tag{5.20}
$$

where ζ is the Riemann zeta function. For $N(\xi)=1$ the first fraction in square brackets is absent and $1/6 \to 2/3$ in the last line. In this case the symmetric propagator from [49] is reproduced. The leading correction to the imaginary part of the potential due to the anisotropy is given by

$$
\mathrm{Im}V_1(r) = g^2 C_F \int \frac{\mathrm{d}^3\boldsymbol{k}}{(2\pi)^3}(1-\cos\boldsymbol{k}\cdot\boldsymbol{r})\frac{1}{2}\frac{\partial}{\partial\xi}\tilde{G}_S^{00}\Big|_{\xi=0}.
\tag{5.21}
$$

The remaining integrations can be done numerically, and the results for the real and imaginary parts of the static potential are shown in figure 5.2, where the angle between $\boldsymbol{r}$ and the anisotropy axis has been defined: $\cos\theta_r \equiv \boldsymbol{r}\cdot\boldsymbol{n}/r$. For the normalization $N(\xi)=1$ it has been observed that an increasing anisotropy lowers the real part of the static potential towards a Coulomb potential [36]. However, this follows trivially for $\xi\to\infty$ since the medium is disappearing in this case, and hence $m_D \to 0$. By contrast, the effect of the anisotropy is much weaker when the normalization $N(\xi)=\sqrt{1+\xi}$ is chosen. Note also, that in this case the potential is even slightly enhanced at small distances. The difference between the two normalizations is even more pronounced in the imaginary part, which is caused by Landau damping and introduces a broadening of the spectral function [37]. A weaker damping effect is seen for $N(\xi)=1$, leading to the conclusion that bound states should melt at higher temperatures [47, 48, 49]. For $N(\xi)=\sqrt{\xi+1}$, this effect is modified and persists only at very large distances. For smaller distances, on the scale of the bound states, there is only very little difference to the isotropic case. Uncertainties due to non-perturbative corrections to the diffusive physics underlying the existence of the imaginary part were found to be significantly larger in recent studies [29, 55].

5.4   Strong Anisotropy, $\xi \to \infty$

Having seen that, with the properly normalized distribution function, the effects of a weak momentum space anisotropy on the static potential are rather small, we are now asking how a maximally anisotropic plasma would behave. To begin the gluon propagator in a general covariant gauge is revisited, (5.7), to discuss some aspects of the dispersion relations which have been derived in [45].

In the limit of maximal anisotropy, the structure functions $\alpha(K)-\delta(K)$ take on an analytic form [45], facilitating a numerical evaluation of the dispersion relations of the retarded gluon propagator, $\Delta_G = 0$ and $\Delta_A = 0$. The associated modes are referred to as electric and magnetic modes respectively (for an analysis of dispersion relations at arbitrary anisotropies see [44, 45]). They can be conveniently expressed by introducing effective pole masses $m(\boldsymbol{k})$, which satisfy the relation

$$
\omega^2 = k^2 + m^2(\boldsymbol{k})
\tag{5.22}
$$

at poles and branch cuts of the electric and magnetic propagators. The results from a numerical determination of the pole masses are illustrated in figure 5.3 and summarized in the following. The
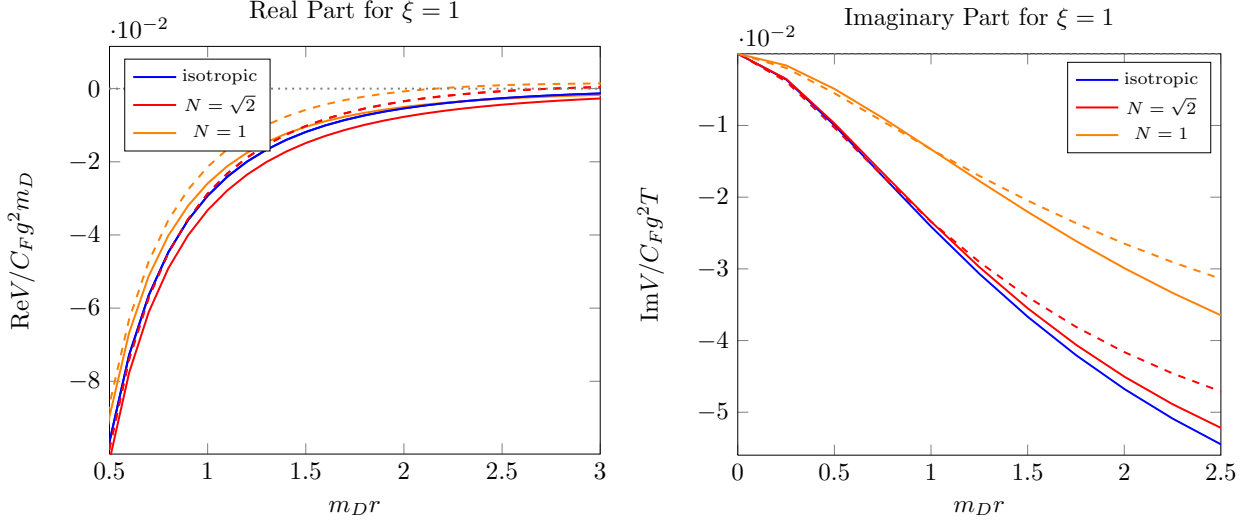
Figure 5.2: Real (left) and imaginary (right) part of the static potential. The blue curve corresponds to the isotropic plasma, $\xi = 0$, the other curves to $\xi = 1$ with normalization factor $N(\xi) = 1$ (orange) and $N(\xi) = \sqrt{1 + \xi}$ (red). The potential is evaluated for $\theta_r = \frac{\pi}{2}$ (solid) and $\theta_r = 0$ (dashed).

dynamical screening masses of the lowest electric mode as well as the magnetic mode are found to be comparable in magnitude to the screening masses in an isotropic medium with a moderate angular dependence of both masses towards higher momenta. The findings indicate that strongly coupled interactions over large distances are suppressed leading to a deconfinement of colour charges. This is a prerequisite for the possibility of a consistent perturbative treatment using the HTL approach.

For $\theta_k < \pi/4$ the gluon propagator has additional poles along the imaginary ω-axis indicating the existence of unstable field modes. The instability, which is present in a general anisotropic QCD plasma, is speculated to be responsible for the rapid isotropisation of the quark gluon plasma observed in heavy ion collisions [56]. The growth rate $\gamma = \text{Im}(\omega)$ of unstable modes is observed to increase and to peak at higher momenta towards the symmetry axis.

5.5   The Static Potential

Next, the static limit of the maximally anisotropic propagator is taken in order to discuss the static potential. At maximal anisotropy the appropriate effective masses read:

$$m_\alpha^2 = -\frac{\pi m_D^2}{4 \tan^2 \theta_k} , \quad m_\beta^2 = \frac{\pi m_D^2}{4} , \quad m_\gamma^2 = \frac{\pi m_D^2}{4} \left(1 + \frac{2}{\tan^2 \theta_k} \right) , \quad m_\delta^2 = \frac{\pi m_D^2}{4} \frac{\cos \theta_k}{\sin^2 \theta_k} . \quad (5.23)$$

The symmetric self energy, Eq. (5.19), needs to be reevaluated as well. Since the momentum distribution function for the anisotropic medium $f(\boldsymbol{p})$ becomes sharply peaked around $\boldsymbol{v}_p \cdot \boldsymbol{n} = 0$ upon sending ξ to infinity, the following identity may be derived [57]:

$$\lim_{\xi \to \infty} f(\boldsymbol{p}) = \delta(\boldsymbol{v}_p \cdot \boldsymbol{n}) \int_{-\infty}^{\infty} dx \, n_{\text{B}}(p\sqrt{1 + x^2}) = \delta(\boldsymbol{v_p} \cdot \boldsymbol{n})h(p). \quad (5.24)$$
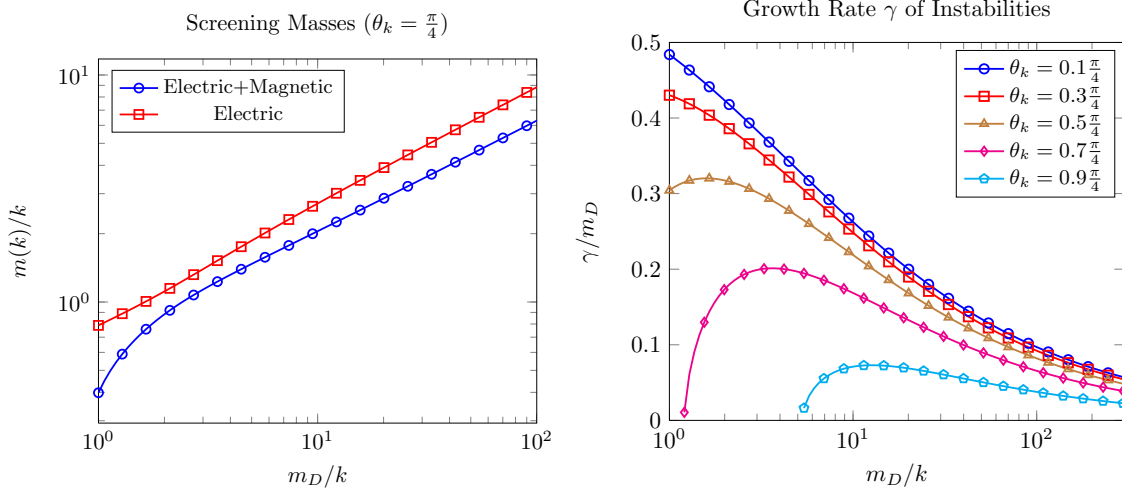
Figure 5.3: The effective masses of stable electric and magnetic modes (shown on the left for $\theta_k = \pi/4$ and $k \leq m_D$) indicate a screening of long range interactions. For $\theta_k < \pi/4$ the gluon propagator has poles on the imaginary ω-axis due to the Weibel instability. The growth rate $\gamma = \mathrm{Im}(\omega)$ of the associated unstable modes (right) increases towards the symmetry axis.

The self energy thus takes the following analytically tractable form:

$$i\Pi_S^{\mu\nu}(\boldsymbol{k}) = \frac{8\pi g^2 N}{k} \int \frac{\mathrm{d}^3 \boldsymbol{p}}{(2\pi)^3} \, v_p^\mu v_p^\nu \, h(p)\delta(\boldsymbol{v}_p \cdot \boldsymbol{n})\delta(\boldsymbol{v}_p \cdot \boldsymbol{v}_k) \left(1 + h(p)\frac{|\boldsymbol{p} + \boldsymbol{k}|}{k}\delta(\boldsymbol{v}_k \cdot \boldsymbol{n}) \right). \qquad (5.25)$$

The Bose enhanced part of the self energy is amplified by a factor $|\boldsymbol{p} + \boldsymbol{k}|/k \approx p/k$ which will translate into an amplification by T/k, indicating that scattering processes are dominated by Bose enhanced scattering into the thermal plane. The self energy is diagonal,

$$i\Pi_S^{00} = i\Pi_S^{jj} = \frac{m_D^2}{k\beta \sin\theta_k} \left(c_\parallel + \frac{c_\perp}{k\beta}\delta(\boldsymbol{v}_k \cdot \boldsymbol{n}) \right), \quad k_i\Pi_S^{ij} = n_i\Pi_S^{ij} = 0 \qquad (5.26)$$

with $m_D^2 = \frac{N}{3}g^2 T^2$ and the prefactors c_x are obtained from the following integrals

$$c_\parallel = \frac{6}{\pi^2}\beta^3 \int_0^\infty dp \, p^2 h(p) = 2.9231\ldots$$

$$c_\perp = \frac{6}{\pi^2}\beta^4 \int_0^\infty dp \, p^3 h^2(p) = 3.4230\ldots \qquad (5.27)$$

The symmetric propagator can now be calculated from (5.9) in a straightforward fashion. Its longitudinal component can be separated in contributions dominated by external momenta perpendicular and parallel to the symmetry axis

$$i\tilde{G}_S^{00}(\boldsymbol{k}) = i\tilde{G}_S^\perp(\boldsymbol{k}) + i\tilde{G}_S^\parallel(\boldsymbol{k})$$

$$i\tilde{G}_S^\perp(\boldsymbol{k}) = \frac{c_\perp m_D^2}{\beta^2} \frac{1}{k^2(k^2 + \frac{\Pi}{4}m_D^2)^2}\delta(\cos\theta_k)$$

$$i\tilde{G}_S^\parallel(\boldsymbol{k}) = \frac{c_\parallel m_D^2}{\beta k \sin\theta_k} \frac{(k^2 + m_\alpha^2 + m_\gamma^2)^2}{[(k^2 + m_\alpha^2 + m_\gamma^2)(k^2 + m_\beta^2) - m_\delta^4]^2}. \qquad (5.28)$$
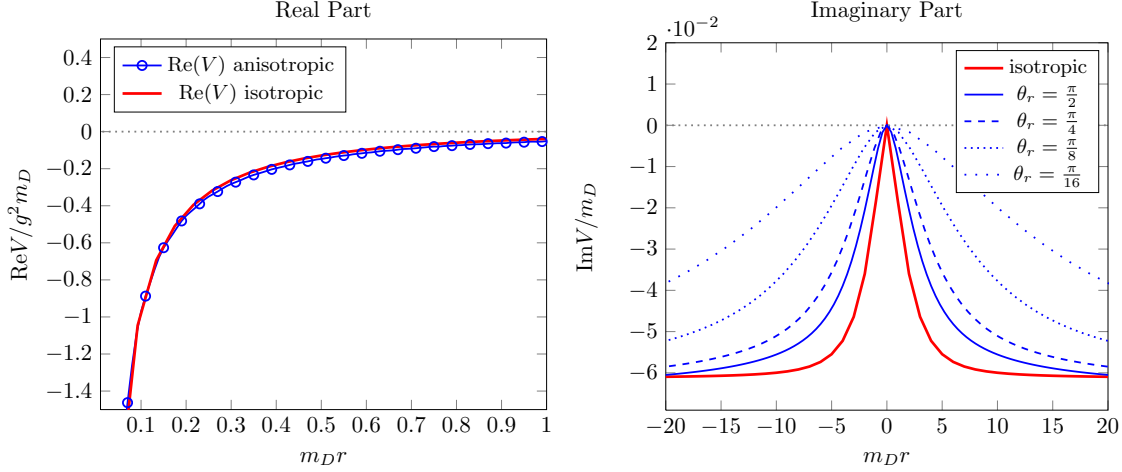
Figure 5.4: The real part of the anisotropic static potential, normalized to $V(\infty) = 0$ and the imaginary part shown as a function of the radial separation r for $N = 3$ and $g^2 = 3$. The cylindrical symmetry of the anisotropic imaginary part is illustrated by varying θ_r.

The first component corresponds to Bose enhanced scattering into the thermal plane and is enhanced in $\frac{T}{k} \gg 1$ while the second component, corresponding to scattering away from the thermal plane, is suppressed even for $\sin \theta_k \to 0$ due to the diverging effective mass m_δ^2 in this limit. Contributions from the symmetric propagator will therefore be dominated by momenta perpendicular to the symmetry axis,

$$\mathrm{i}\tilde{G}_S^{00}(\boldsymbol{k}) \approx \mathrm{i}\tilde{G}_S^{\perp}(\boldsymbol{k}) \; . \tag{5.29}$$

The static potential in a maximally anisotropic medium can now be discussed, by inserting these ingredients into (5.5). Upon choosing a spherical coordinate system with the anisotropy vector $\boldsymbol{n}$ pointing in the z-direction, $\cos \theta_r \equiv \boldsymbol{r} \cdot \boldsymbol{n}/r$ and with the abbreviation $x = \cos \theta_k$, one angular integration can be performed immediately leading to

$$
\begin{aligned}
\mathrm{Re}V(\boldsymbol{r}) \;=\;& g^2 \mathrm{C_F} \int \frac{\mathrm{d}k\,\mathrm{d}x}{(2\pi)^2} \left(1 - \mathrm{J}_0(kr\sqrt{1-x^2}\sin\theta_r)\cos\left(krx\cos\theta_r\right) \right) \\
& \times \frac{k^2(k^2 + m_\alpha^2 + m_\gamma^2)}{(k^2 + m_\alpha^2 + m_\gamma^2)(k^2 + m_\beta^2) - m_\delta^4} \; ,
\end{aligned}
\tag{5.30}
$$

where $\mathrm{J_n}$ is the Bessel function of the first kind. The expression is readily evaluated numerically using standard integration routines [58]. The potential contains a linear divergence which we subtract by normalizing $V(|\boldsymbol{r}| \to \infty) = 0$. The resulting real part displays an approximate spherical symmetry. The radial profile, as depicted in figure 5.4 for $N = 3$, turns out to be in good agreement with the standard Debye screened potential. For the imaginary part we obtain in a similar way

$$\mathrm{Im}V(\boldsymbol{r}) = -\frac{3\mathrm{C_F}m_D^4 c^{\perp}}{8N\pi^2} \int \mathrm{d}k \, (1 - \mathrm{J}_0(kr\sin\theta_r))\frac{1}{(k^2 + \frac{\pi}{4}m_D^2)^2} \; . \tag{5.31}$$

The imaginary part thus only depends on the separation $r\sin\theta_r$ of the static quark pair in the thermal plane perpendicular to the anisotropy vector. Unlike the previously studied quantities the

imaginary part turns out to be quantitatively different from its isotropic counterpart [28]. This is because the damping of the static quark correlator is significantly weakened in the collision plane for reasonable values of the bare coupling, while no additional damping occurs along the anisotropy axis.

5.6 Quarkonium Spectral Function

In order to compare a more physical quantity between the isotropic and anisotropic cases, the quarkonium spectral function is calculated as well. Since this has not been done before for anisotropies, it is presented in some detail. For a $q\bar{q}$ system with finite constituent mass M the following Schrödinger equation must be solved [28],

$$\mathrm{i}\partial_t C_{21}(t, \boldsymbol{r}) = \left(2M - \frac{\triangle_{\boldsymbol{r}}}{M} + V(\boldsymbol{r}) \right) C_{21}(t, \boldsymbol{r}), \qquad \mathrm{i}C_{21}(0, \boldsymbol{r}) = -6N\delta^{(3)}(\boldsymbol{r}) \tag{5.32}$$

where $V(\boldsymbol{r})$ is the real time static potential discussed in the previous sections. For $\boldsymbol{r} = \boldsymbol{0}$ the quarkonium correlator coincides with the quark current correlator $C_{21}(t, \boldsymbol{0}) = \langle J^\mu(t)J_\mu(0)\rangle$ where $J^a_\mu = \overline{\psi}\gamma_\mu T^a\psi$. The quark pair is assumed to be created at time $t = 0$ and the initial condition for the Schrödinger equation (5.32) ensues from the afore mentioned relation. The spectral function for quarkonium at rest $\rho(\omega)$ can be calculated from the difference of the two off-diagonal elements of the heavy-quarkonium correlator,

$$\rho(\omega) = \int \mathrm{d}t \, \mathrm{e}^{-\mathrm{i}\omega t} \left\{ \mathrm{i}C_{21}(t, \boldsymbol{0}) - \mathrm{i}C_{12}(t, \boldsymbol{0}) \right\} . \tag{5.33}$$

In thermal equilibrium both components are related via the Kubo- Martin- Schwinger condition, which does not hold for the system under consideration. In the operator formalism the difference between the two correlators takes the form

$$C_{21}(t, \boldsymbol{0}) - C_{12}(t, \boldsymbol{0}) = \frac{1}{Z}\mathrm{Tr}\left\{ \hat{\sigma}\hat{J}_\mu(t, \boldsymbol{0})\hat{J}^\mu(0, \boldsymbol{0}) \right\} - \frac{1}{Z}\mathrm{Tr}\left\{ \hat{\sigma}\hat{J}_\mu(0, \boldsymbol{0})\hat{J}^\mu(t, \boldsymbol{0}) \right\} , \tag{5.34}$$

where the trace is over all energy eigenstates and $\hat{\sigma}$ is the statistical operator of the anisotropic system. Using the cyclicity of the trace, C_{12} is expressed as

$$C_{12}(t, \boldsymbol{0}) = \frac{1}{Z}\mathrm{Tr}\left\{ \hat{J}_\mu(t, \boldsymbol{0})\hat{\sigma}\hat{J}^\mu(0, \boldsymbol{0}) \right\} . \tag{5.35}$$

The difference between both contributions is that in C_{12} the density matrix acts on the Hilbert space of the plasma with the quark pair present. For $2\beta M \gg 1$, where the quarkonium threshold $\simeq 2M$ is much higher than the average particle momentum β^{-1} in the thermal plane, the contribution of the correlator C_{12} will be substantially suppressed. This justifies the following approximation which is also employed in the equilibrium case [37]:

$$\rho(\omega) \approx \int dt \, \mathrm{e}^{-\mathrm{i}\omega t} C_{21}(t, \boldsymbol{0}). \tag{5.36}$$

The Wightman propagator $C_{21}(t, \boldsymbol{r})$ for a static quark pair is obtained at large positive times as a solution of the Schrödinger equation (5.4). Similarly, using $\mathrm{i}C_{ij}(-t, \boldsymbol{r}) = [\mathrm{i}C_{ij}]^*(t, \boldsymbol{r})$, the static

potential in the infinite past is

$$V'(\boldsymbol{r}) = \lim_{t \to -\infty} \frac{\mathrm{i}\partial_t C_{22}(t, \boldsymbol{r})}{C_{22}(t, \boldsymbol{r})} = -g^2 \mathrm{C_F} \int \frac{\mathrm{d}^3 \boldsymbol{k}}{(2\pi)^3} (1 - \cos \boldsymbol{k} \cdot \boldsymbol{r}) \tilde{G}_{22}^{00} = V^*(\boldsymbol{r}) \,. \tag{5.37}$$

The spectral function can thus be computed from the relation

$$\rho(\omega) = 2 \int_0^\infty dt \left\{ \cos(\omega t) \mathrm{Re}(\mathrm{i}C_{21}) - \sin(\omega t) \mathrm{Im}(\mathrm{i}C_{21}) \right\} . \tag{5.38}$$

The numerical solution of the Schrödinger equation for the Wightman correlator C_{21} is non-trivial. The task consists in the interesting problem to solve a parabolic complex differential equation in three dimensions with a potential consisting of a parametrically large spherically symmetric real part and a small cylindrically symmetric imaginary part. Due to the positive parity and the symmetry of the potential with respect to the anisotropy axis, the correlator may be expanded in a subset of spherical harmonics,

$$\begin{aligned}
C_{21}(t, \boldsymbol{r}) &= c_l(t, r) \mathrm{Y}_{2l}^0(\theta_r) \,, \\
V(\boldsymbol{r}) &= V^{(re)}(r) + \mathrm{i} V_l^{(im)}(r) \mathrm{Y}_{2l}^0(\theta_r) \,,
\end{aligned} \tag{5.39}$$

with $V^{(re)}(r)$ and $V_l^{(im)}(r)$ denoting the real and imaginary parts of the potential respectively. With the rescaling

$$c_l(t, r) = \frac{u_l(t, r)}{r} \mathrm{e}^{-\mathrm{i}2Mt}, \tag{5.40}$$

the one-dimensional Schrödinger equations for the components of the spherical expansion take a numerically tractable form,

$$\mathrm{i}\partial_t u_l = -\frac{1}{M} \left(\frac{\mathrm{d}^2}{\mathrm{d}r^2} - \frac{2l(2l+1)}{r^2} \right) u_l + V^{(re)} u_l + \mathrm{i}\mathcal{P}_{lmn} V_m^{(im)} u_n \,. \tag{5.41}$$

The tensor $\mathcal{P}_{lmn}$ is defined by a unit sphere integration over a product of three spherical harmonics which can be evaluated exactly via Wigner-3j symbols [59]:

$$\mathcal{P}_{lmn} = \int \mathrm{d}\Omega \mathrm{Y}_{2l}^0 \mathrm{Y}_{2m}^0 \mathrm{Y}_{2n}^0 = \sqrt{\frac{(4l+1)(4m+1)(4n+1)}{4\pi}} \begin{pmatrix} 2l & 2m & 2n \\ 0 & 0 & 0 \end{pmatrix}^2 . \tag{5.42}$$

Without the coupling between different spherical components, a relation of the following type needs to be evaluated for every timestep $\mathrm{d}t$,

$$\tilde{u}_l(t + \mathrm{d}t) = \mathrm{e}^{-\mathrm{i}\hat{\mathrm{H}}_l \mathrm{d}t} u_l(t), \tag{5.43}$$

where the differential operator $\hat{\mathrm{H}}_l$ is given by

$$\hat{\mathrm{H}}_l = -\frac{1}{M} \left(\frac{d^2}{dr^2} - \frac{2l(2l+1)}{r^2} \right) + V^{(re)}(r) + \mathrm{i}\mathcal{P}_{lml} V_m^{(im)}(r) \,. \tag{5.44}$$

To ensure a stable time evolution we employ the Crank-Nicolson scheme [60] by introducing the second order approximation

$$\left(1 + \frac{1}{2} \mathrm{i}\hat{\mathrm{H}} \mathrm{d}t \right) \tilde{u}_l(t + \mathrm{d}t) = \left(1 - \frac{1}{2} \mathrm{i}\hat{\mathrm{H}} \mathrm{d}t \right) u_l(t) \,, \tag{5.45}$$

which is solved as a tridiagonal matrix equation for the discretized system. The full problem is solved without sacrificing the stability of the algorithm by treating the parametrically small coupling between the various spherical components as a linear perturbation,

$$u_l(t + \mathrm{d}t) = \tilde{u}_l(t + \mathrm{d}t) + \mathrm{d}t \sum_{m,n \neq l} \mathcal{P}_{lmn} V_m^{(im)} \, u_n(t) \, . \tag{5.46}$$

The system is discretized on a finite lattice with spacing a and lattice sites $[1, \ldots, N_L]$, choosing the boundary conditions

$$u_l(0) = 0 \quad \text{and} \quad u_l(N_L + 1) = 0 \tag{5.47}$$

for all spherical components with l limited to the range $l \in [0, \ldots, l_{max}]$. The initial condition (5.32) is discretized as follows [37],

$$u_0(0, r) = -6N \frac{r}{4\pi} \delta(r) \rightarrow -6N \left(\frac{2}{\pi a} \right)^2 \frac{n(-1)^{n+1}}{4n^2 - 1} \, ,$$

with $r = na$ being the discretized radial coordinate. All other spherical components $u_{l \neq 0}(0, r)$ are set to zero. The scale for the numerical determination of the bottomonium spectral function for $N = 3$ shown in Fig. 5.5 is set by the QCD scale $\Lambda_{\overline{MS}} \simeq 300 MeV$ in the $\overline{MS}$ scheme. The bottom quark mass $M = 14.15 \Lambda_{\overline{MS}}$ is chosen in agreement with [37]. Introducing a spherical cutoff $l_{max} = 10$ the system of coupled one dimensional Schrödinger equations is solved on three different grids $N_L \in \{2000, 4000, 8000\}$ with a fixed physical size of $aN_L = 400/\Lambda_{\overline{MS}}$. A time-step of $dt = 0.02a$ is chosen and in all three cases the system is evolved for a fixed time $t = 265/\Lambda_{\overline{MS}}$. The spectral function depends linearly on the lattice spacing a since the coupling between the different spherical components of (5.41) is introduced as a linear perturbation. To take into account a^2-corrections, the spectral function is extrapolated to the continuum by fitting the a-dependence of the spectral function at a given frequency against a quadratic polynomial. The melting of the quarkonium resonance due to Landau damping effects is in qualitative agreement with the decay of the resonance in thermal equilibrium obtained using the same approach [37].

5.7 Summary of Physical Findings

The effects of an anisotropic momentum distribution on the real-time static potential of a quark pair in a plasma has been reconsidered using a normalized distribution function. At small anisotropies, previously observed effects of the distortion were shown to be mostly due to the missing normalization factor. In order to probe for a larger effect the limit of maximal anisotropy was investigated. The calculation of the quarkonium spectral function indicates a melting of the quarkonium resonance similar to the one for an isotropic medium due to a screening of the Coulomb potential and a dissociation of bound states by Landau damping effects in the thermal plane. Strongly coupled interactions over large distances are suppressed due to the generation of nearly isotropic screening masses comparable in magnitude to their equilibrium counterparts. For small angles with the anisotropy axis, the gluon propagator has additional poles along the imaginary ω-axis indicating the existence of unstable field modes. The growth rate $\gamma = Im(\omega)$ of unstable modes is observed to increase and to peak at higher momenta towards the symmetry axis.

The overall physical picture that emerges from a weak-coupling analysis of this system indicates that the strongly anisotropic state of matter created in the initial stages of heavy-ion collisions is
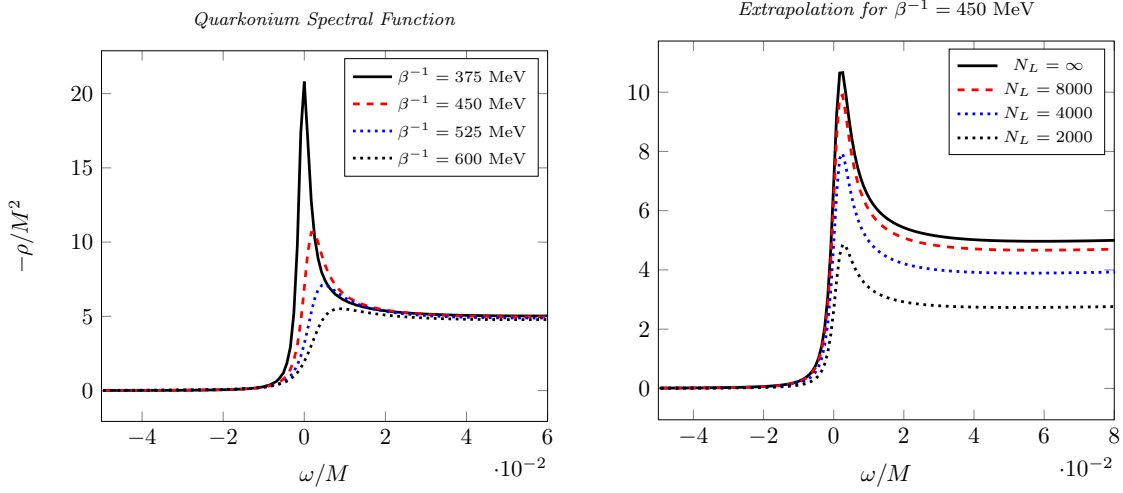
Figure 5.5: Left: The melting of the bottomonium spectral function in a maximally anisotropic quark gluon plasma at a fixed coupling of $g^2 = 3$ ($\alpha_s \approx 0.25$). Right: The polynomial extrapolation of the spectral function using three different grid spacings.

characterized by an early deconfinement of colour charges and a rapid diffusive transport of these charges in the collision plane. The most striking result is that observables related to quarkonium are very similar to their counterparts in an isotropic medium, making it difficult to distinguish a highly anisotropic plasma from its isotropic counterpart on the basis of heavy quark observables.

Lattice Techniques

6 Lattice Gauge Theory

*Anyone who attempts to generate random numbers by
deterministic means is, of course, living in a state of sin.*

John von Neumann

The only viable technique for an ab-initio calculation of thermal correlation functions in quantum field theory available today consists in a Monte Carlo evaluation of the euclidean path integral discretized on a hypercubic lattice. This approach is by construction limited to static quantities in thermal equilibrium at vanishing chemical potential and difficult to extend beyond this realm of applicability. In the following this common technique is briefly reviewed for thermal Yang-Mills theory, and the lattice notation used throughout this thesis is introduced. The last part of this chapter discusses the free energy of a static quark pair in Yang-Mills theory as well as in the Green-Karsch effective theory as a simple model for Yang-Mills theory on coarse lattices.

6.1 Yang-Mills Theory on the Lattice

To discretize a gauge theory it is necessary to keep in mind that the mathematical function of gauge fields is to realize the parallel transport between different points in space-time and thus to allow for a construction of gauge independent quantities. A natural way to discretize gauge fields on a hypercubic space-time lattice is thus to introduce an $SU(N)$ variable in some representation r for every link connecting adjacent lattice sites to represent the Wilson line connecting the corresponding space-time points along a straight path. Gauge fields are thus represented by a set of *links* $\{U_\mu(x)\}$ defined as

$$U_\mu(x) = W_{x \to x+\hat{\mu}} = e^{iga\tilde{A}_\mu(x)} \tag{6.1}$$

at every point x of the lattice and in every direction μ of the Euclidean space-time. The distance a between neighboring lattice points, which is assumed to be equal in every space-time direction, is called the *lattice spacing*. $\tilde{A}_\mu(x) = \tilde{A}_\mu^a(x)T^a$ is the effective gauge field along a straight line between neighboring lattice points x and $x + \hat{\mu} = x + ae_\mu$ [e_μ is the unit vector in the direction μ]. The $SU(N)$ generators T^a are normalized according to the convention

$$\text{Tr } T^a T^b = \frac{1}{2}\delta_{ab} \tag{6.2}$$

in a lattice context. To allow for the introduction of quark like color charges a fundamental representation $r = 1$ is chosen throughout this thesis with the generators of $SU(2)$ and $SU(3)$ given by the Pauli and Gell-Mann matrices (see the appendix) multiplied by a factor of $1/\sqrt{2}$ to take into account the normalization (6.2). Gauge transformations $S(x)$ are defined at lattice sites with links transforming at both end points according to the usual relation for parallel transporters:

$$U_\mu(x) \to S^+(x + \hat{\mu})U_\mu(x)S(x). \tag{6.3}$$

In numerical simulations the extent of the lattice is limited by imposing periodic boundary conditions $U_\nu(x) = U_\nu(x + N_\mu\hat{\mu})$ in every direction μ and thus compactifying the lattice to a hyper-torus
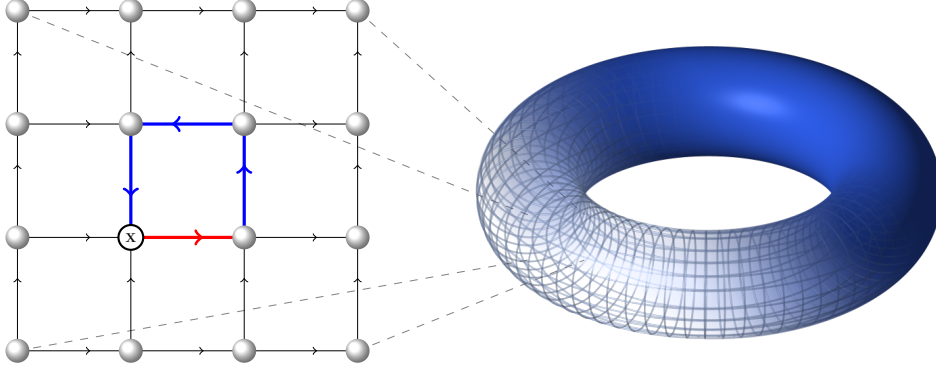
Figure 6.1: Illustration of a 2-dimensional lattice compactified to a torus by periodic boundary conditions. The plaquette $U_{12}(x)$ is shown in blue while the single link $U_1(x)$, which forms a part of the plaquette, is shown in red.

(see figure 6.1 for an illustration). By performing a Fourier series expansion of the effective gauge fields $\tilde{A}^a_\mu$ the space-time lattice is related to a lattice in momentum space with lattice spacing $\tilde{a}_\mu = 2\pi/aN_\mu$ in the direction μ and extent $2\pi/a$. In the limit of infinite lattice extent $aN_\mu \to \infty$ in all directions μ the lattice model corresponds to a gauge theory with continuous momenta constrained to a Brillouin zone with *momentum cutoff* $\Lambda_{BZ} = |k|_{max} = \pi/a$. The expectation value of a function $f(U)$ of the links is defined by the lattice representation of the path integral (2.26)

$$\langle f \rangle = \frac{1}{Z} \int [\mathrm{D}U]\, f(U)\, \mathrm{e}^{-S}, \quad Z = \int [\mathrm{D}U]\, \mathrm{e}^{-S} \tag{6.4}$$

where S is the action of the lattice model and the integration is performed over every link using the gauge invariant Haar measure [61]. The action S of the lattice model is constrained by the demands that it must reduce to the Euclidean Yang-Mills action in the continuum limit $a \to 0$ and should respect the gauge symmetry of Yang-Mills theory, i.e. be invariant under the transformation (6.3). So called plaquette actions rely on the gauge invariant Wilson loops around plaquettes of the lattice

$$U_{\mu\nu}(x) = U_\mu(x)U_\nu(x+\hat{\mu})U^+_\mu(x+\hat{\nu})U^+_\nu(x) \tag{6.5}$$

as construction elements to satisfy these demands. The most simple action belonging to this family is the *Wilson action*

$$S_W = \beta_L \sum_x \left\{ 1 - \frac{1}{N}\mathrm{ReTr}\sum_{\mu<\nu} U_{\mu\nu}(x) \right\}, \quad \text{where} \quad \beta_L = \frac{2N}{ag^2}. \tag{6.6}$$

The constant β_L is called the *lattice coupling*. By parametrizing links with the effective fields $\tilde{A}_\mu$ it is straightforward to show that S_W reduces to the Yang-Mills action in the limit $a \to 0$. Deviations from the continuum theory appear at $\mathcal{O}(a^2)$ in a systematic expansion of the action in the lattice spacing a and are called *discretization errors* while errors introduced by a compactification of the lattice are called *volume effects*.

6.2 Markov Chains and Importance Sampling

To introduce the necessary techniques for a numerical evaluation of the path integral (6.4) a general statistical system is considered in this section which is characterized by a finite set of quantities $\{\sigma_i\}, i \in [1, \ldots, m]$. Let Ω be the state space of the system and $f : \Omega \to \mathbb{R}$ be some function of these variables. The expectation value of the function f is then defined as

$$\langle f \rangle = \prod_i \int d\sigma_i \ f(\varphi) \ w(\varphi) \tag{6.7}$$

where $\varphi = \{\sigma_i\} \in \Omega$. The positve definite function $w : \Omega \to \mathbb{R}$ is called the *statistical weight*. Numerical algorithms for a practical evaluation of this integral rely on the construction of a suitable Markov chain of state space configurations. Formally let $\{\Phi_i\}$, $i \in [0, \ldots, n+1]$ be a sequence of states φ_i generated from a finite[1] state space Ω by a stochastic process. If the conditional probability P obeys

$$P(\Phi_{n+1} = \varphi_{n+1} | \Phi_n = \varphi_n, \ldots, \Phi_1 = \varphi_1) = P(\Phi_{n+1} = \varphi_{n+1} | \Phi_n = \varphi_n) \tag{6.8}$$

and the transition probability $\varphi_n \to \varphi_{n+1}$ is thus independent of previous states the sequence is called a *Markov chain*. If, in addition, the conditional probability $P(\Phi_{n+1} = \psi | \Phi_n = \varphi)$ is independent of n for all $\varphi, \psi \in \Omega$ the Markov chain is said to be a *homogenous*. A Markov chain where any state is accessible from any other state in some finite sequence of steps

$$\exists \ n \geq 1 : \ P(\Phi_{i+n} = \psi | \Phi_i = \varphi) > 0 \ \ \forall \ (\varphi, \psi, i) \tag{6.9}$$

is said to be *irreducible*. Finally a Markov chain is said to be *positive recurrent* if the largest possible number of steps after which the Markov chain will return to an initial state φ is finite for all states $\varphi \in \Omega$. It is possible to show that a homogenous and irreducible Markov chain will approach a unique stationary probability distribution of states $\pi(\varphi)$ after a large number of steps from any initial state, if and only if it is positive recurrent. This property leads to a statement known as the ergodic theorem:

The ergodic theorem

Let $\Phi_n, n > 0$ be an irreducible, homogenous and positive recurrent Markov chain with stationary distribution π and let $f : \Omega \to \mathbb{R}$ such that

$$\sum_{\varphi \in \Omega} |f(\varphi)| \pi(\varphi) < \infty \tag{6.10}$$

then for any initial state,

$$\lim_{N \to \infty} \sum_{i=1}^{N} f(\Phi_i) = \sum_{\varphi \in \Omega} f(\varphi) \pi(\varphi). \tag{6.11}$$

---

[1] Note that the state space for a lattice system implemented on a computer is always finite since the lattice has a finite volume and numbers are represented as binary sequences of limited extent.

This theorem lies at the heart of modern lattice techniques since it states that it is possible to obtain the solution to the path integral (6.4) as an average over the sequence of configurations of a Markov chain with stationary solution $\pi = \mathrm{e}^{-\beta S}/Z$. A particularly useful approach to construct this chain in practice is to demand a *detailed balance condition* to hold for the probability distribution π

$$P(\psi \leftarrow \varphi)\pi(\varphi) = P(\varphi \leftarrow \psi)\pi(\psi) \tag{6.12}$$

where $P(\psi \leftarrow \varphi) = P(\Phi_{n+1} = \psi | \Phi_n = \varphi)$. The condition states that the overall probability for the transitions $\varphi \to \psi$ and $\psi \to \varphi$ between arbitrary states $\varphi, \psi \in \Omega$ is identical in every step of the Markov chain. A probability distribution π satisfying this property is evidently stationary. The principle of detailed balance will be used as a guiding concept for the construction of lattice algorithms throughout this thesis.

The most simple method to implement this concept is the *Metropolis algorithm*. A single iteration of the algorithm consists of proposing a random change of the field configuration $\varphi \to \psi$ with probability $P_C(\psi \leftarrow \varphi) > 0 \ \forall \varphi, \psi \in \Omega$ and accepting the suggested change with probability

$$P_A(\psi \leftarrow \varphi) = \min\left(1, \frac{P_C(\varphi \leftarrow \psi)w(\psi)}{P_C(\psi \leftarrow \varphi)w(\varphi)}\right). \tag{6.13}$$

This so called *accept/ reject step* can be conveniently implemented by generating a random number $\lambda \in \mathbb{R}$, drawn with uniform probability from the interval $[0 \ldots 1]$, and accepting the suggested change whenever λ is smaller than the probability ratio (6.13). For practical purposes it is usually necessary to partition the set of variables $\{\sigma_i\}$ into subsets which may consist of individual variables for instance and perform a subsequent Metropolis update of all subsets. A critical issue in the design of any Metropolis algorithm is the choice of a suitable proposition step to ensure a sufficient acceptance rate which is typically required to exceed 50%.

Another efficient technique consists in iterating through the individual variables σ_i of the system and performing a random change $\sigma_i \to \sigma_i'$ of these variables with transition probability

$$P_i(\sigma_i' \leftarrow \sigma_i) = w(\sigma_i', \{\sigma_{j \neq i}\}) > 0. \tag{6.14}$$

The algorithm therefore subsequently generates the correct statistical distribution for each variable. It is important to note that this is *not* identical to generating the correct distribution for the overall system if different variables of the system are coupled. It is however straightforward to show that the overall transition probability

$$P(\{\sigma_i'\} \leftarrow \{\sigma_i\}) = \prod_i P_i(\sigma_i' \leftarrow \sigma_i) \tag{6.15}$$

after one iteration of the algorithm, which consists in a sweep of all variables of the system, satisfies detailed balance (6.12). Since the statistical weight is given by a Boltzmann factor $w(\varphi) = e^{-\beta H(\phi)}/Z$ in many physical problems and individual variables are drawn from a thermal distribution the approach is called *heatbath algorithm*.

It is a common feature of all Monte-Carlo algorithms that, starting from an arbitrary initial configuration $\varphi_0 \in \Omega$, the desired probability distribution $\pi(\varphi) = w(\varphi)$ is only approached to a desired precision after some finite number s of steps. This equilibration time is often called *"burn in"* and accounted for in practice by omitting all states $\{\varphi_i\}, i < s$ of the chain in the calculation of expectation values.

6.3 Algorithms for Lattice Yang-Mills Theory

For lattice Yang-Mills theory with a Wilson action (6.6) efficient algorithms have been developed for the numerical evaluation of the discretized path integral (6.4). These methods shall be briefly reviewed in the following to lay the ground for algorithms introduced in the coming chapters. For details the reader is referred to [61].

The starting point for the *Cabbibo-Marinari* pseudo-heatbath algorithm is to decompose the group $SU(N)$ into a set of $SU(2)$ subgroups $SU(2)_k, k \in \{1, \ldots, m\}$ which cover the whole group and leave only the unit element invariant. To perform a heatbath update of the individual link $U_\mu(x) \in SU(N)$ the new link

$$U'_\mu(x) = a_m \ldots a_1 U_\mu(x) \tag{6.16}$$

is chosen by subsequently drawing the transformation elements $a_k \in SU(2)_k$ from the distribution

$$dP(a_k) = d^{(k)} a_k \frac{e^{-S_W(a_k U_\mu^{k-1}(x), \hat{U})}}{Z_k(U_\mu^{k-1}(x))} \quad \text{where} \quad Z_k(U) = \int d^{(k)} a \ e^{-S_W(aU, \hat{U})} \tag{6.17}$$

which is the differential statistical weight after updating the subgroup $SU(2)_{k-1}$ for the link $x \to x + \hat{\mu}$. $\hat{U}$ denotes the set of all remaining links. The Haar measure for $SU(2)_k$ is indicated by the operator $d^{(k)}$ while the link $U_\mu^k(x)$ is defined via:

$$U_\mu^k(x) = a_k U_\mu^{k-1}(x) \quad \text{and} \quad U_\mu^0(x) = U_\mu(x). \tag{6.18}$$

It is convenient to choose a block diagonal form for the subgroups $SU(2)_k$

$$a_k = \begin{pmatrix} 1 & & & & \\ & \ddots & & & \\ & & \alpha_k & & \\ & & & \ddots & \\ & & & & 1 \end{pmatrix} \tag{6.19}$$

with $\alpha_k \in SU(2)$ being in the fundamental representation. The distribution function (6.17) is rewritten by isolating the part of the action S_W which depends on the subgroup $SU(2)_k$ at $x \to x + \hat{\mu}$

$$S_W(U_\mu^k(x), \hat{U}) = -\frac{\beta_L}{N} ReTr(a_k U_\mu^{k-1}(x) S_\mu(x)) + \ldots = -\frac{\beta}{N} ReTr(\alpha_k \rho_k) + \ldots \tag{6.20}$$

where the sum of *staples* along $x \to x + \hat{\mu}$ is defined as (see figure 6.2):

$$S_\mu(x) = \sum_{|\nu| \neq \mu} U_\nu(x + \hat{\mu}) U_\mu^+(x + \hat{\nu}) U_\nu^+(x). \tag{6.21}$$

ρ_k is defined by decomposing $U_\mu^{k-1}(x) S_\mu(x)$ into $SU(2)$ subgroups, using the fact that the sum of two arbitrary $SU(2)$ matrices in the fundamental representation will always be proportional to another $SU(2)$ matrix. The proportionality factor is $|\rho_k| = \sqrt{det(\rho_k)}$. The distribution function for the matrix α_k can thus be written in the following form:

$$dP(\alpha_k) \sim d\alpha_k \exp \frac{\beta}{N} Tr \alpha_k \rho_k. \tag{6.22}$$
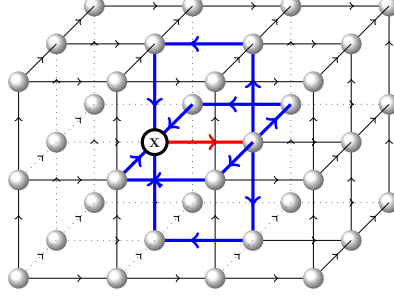
Figure 6.2: Illustration of staples (Wilson lines highlighted in blue) belonging to the link $x \to x + \hat{1}$ (red) on a 3-dimensional lattice. The matrix $S_1(x)$ is defined as the sum of all staples along this link.

To take advantage of the gauge invariance of the Haar measure the matrix transformation $\alpha_k \to \alpha = \alpha_k(|\rho_k|\rho_k^{-1})$ is introduced choosing the parametrization

$$\alpha = \alpha_0 \mathbf{1} + i \sum_i \alpha_i \boldsymbol{\sigma}_i \quad \text{where} \quad \sum_{j=0}^{4} \alpha_j^2 = 1 \tag{6.23}$$

and $\boldsymbol{\sigma}_i, i \in [1, 2, 3]$ are the Pauli matrices. The distribution function is thus given by $[\beta'_L = 2\beta_L/N]$:

$$dP(a_k) \sim d\alpha_0 \sqrt{1 - \alpha_0^2} \exp\left(\beta'_L \alpha_0 |\rho_k|\right) d\Omega \sim dy \left[1 - \left(\frac{\log y}{\beta'_L |\rho_k|}\right)^2\right]^{\frac{1}{2}} d\Omega. \tag{6.24}$$

The variable y introduced in the second step is defined as $y = \exp\left(\beta'_L \alpha_0 |\rho_k|\right)$. $d\Omega$ is the angular integration measure for the vector $\boldsymbol{\alpha} = (\alpha_1, \alpha_2, \alpha_3)$. To generate this distribution y is drawn from the interval $[e^{-\beta'_L |\rho_k|}, e^{\beta'_L |\rho_k|}]$ with uniform probability and accepted according to its statistical weight with probability $P_A(y) = [\ldots]^{1/2}$. The direction of $\boldsymbol{\alpha}$ is chosen randomly. The new link $U^k_\mu(x) = a_k U^{k-1}_\mu(x)$ is finally obtained via $\alpha_k = \alpha \rho_k/|\rho_k|$. A single update of all subgroups and all links with this method is called a *heatbath trial*.

Since subsequent configurations $\{U\}_i \in \Omega, i \in \{1, \ldots n\}$ of the generated Markov chain will not be fully decorrelated the number of actually independent measurements of a function $f : \Omega \to \mathbb{R}$ of the links is expressed as $n/2\tau_f$ where τ_f is called the (integrated) *auto-correlation time* of f:

$$\tau_f = \frac{1}{2} \sum_{t=-\infty}^{\infty} \frac{f(\{U\}_i) f(\{U\}_{i+t})}{f(\{U\}_{i+t})^2} \tag{6.25}$$

The autocorrelation time of any observable can be significantly reduced by the use of *overrelaxation* techniques. It is clear that the transformation $U'_\mu(x) = U_T U^+_\mu(x) U_T$ where $U_T \in \mathrm{SU}(N)$ satisfies detailed balance if the action S_W remains unchanged since $U_\mu(x) = U_T U'^+_\mu(x) U_T$ and thus $P(U' \leftarrow U) = P(U \leftarrow U')$. By choosing $U'_\mu(x)$ as far away as possible from the original link and alternating between heatbath trials and overrelaxation steps a fast decorrelation of field configurations is achieved. When updating block diagonal SU(2) subgroups, it is natural to choose the fundamental transformation matrix

$$U_{Tk} = |\rho_k|\rho_k^{-1} \tag{6.26}$$

to "mirror" the respective subgroup at the minimum of the action.

6.4   Green- Karsch Effective Theory

Before turning to lattice Yang-Mills theory at finite temperature, it is instructive to consider a simple mean-field model [62] for the SU(2) theory obtained using strong coupling techniques. For a more detailed review see [63]. As a starting point the Wilson action is decomposed into the contribution of individual plaquettes $P(U)$:

$$S_W(U) = \sum_P S_P(U) \quad \text{where} \quad S_P(U) = \frac{4}{g^2}\left(1 - \frac{1}{2}\text{ReTr}P(U)\right).$$

(6.27)

Using harmonic analysis on group manifolds [61] the exponential $\mathrm{e}^{-S_P} : SU(2) \to \mathbb{R}$ is rewritten as a series of the group characters $\chi_r(P)$ of the plaquette $P \in SU(2)$ in all representations r of the group:

$$\mathrm{e}^{-S_P} = Z_0\left(\frac{1}{g^2}\right)\left\{1 + \sum_r d_r z_r\left(\frac{1}{g^2}\right)\chi_r(P)\right\}$$

(6.28)

$d_r = r + 1$ is the dimension of the representation while $z_r(1/g^2) = I_{r+1}(4/g^2)/I_1(4/g^2)$ and $Z_0 = g^2 I_1(4/g^2)/2$. The modified Bessel functions are denoted as I_r. Note that the lattice spacing has been absorbed into the coupling $ag^2 \to g^2$. An effective theory is constructed by making the following approximations:

1. *No Magnetic Interactions*
   Magnetic interactions are neglected by discarding the contribution of space-like plaquettes. The motivation is that any deconfinement phase transition in the purely electric effective theory will translate into a phase transition in the full theory since space-like plaquettes tend to reduce the string tension.

2. *Strong Coupling*
   A strong coupling $\beta_L = 4/g^2 \ll 1$ is assumed which, clearly, is motivated by the use of strong coupling techniques. Despite being contradictory to the aim of studying the transition into a weak coupling regime the model successfully captures some essential aspects of the deconfinement transition in the full theory

The partition function of the effective theory thus takes the form [temporal plaquettes are denoted as P_τ]:

$$Z_{GK} = \int [\mathrm{D}U] \prod_{P_\tau}\left\{1 + \sum_r d_r z_r\left(\frac{1}{g^2}\right)\chi_r(P_\tau)\right\}.$$

(6.29)

By integrating out spatial links the effective action can be expressed by characters of Polyakov loops

$$W_{\boldsymbol{x},0\to\beta} = \prod_{\tau=1}^{N_\tau} U_\tau(\boldsymbol{x},\tau),$$

(6.30)

where $\boldsymbol{x}$ is the spatial component of the lattice coordinate and temporal links are denoted as U_τ. The partition function takes the dimensionally reduced form

$$Z_{GK} = \int \prod_x \mathrm{d}W_{\boldsymbol{x},0\to\beta} \prod_{x,i}\left\{1 + \sum_r z_r^{N_\tau}\left(\frac{1}{g^2}\right)\chi_r(W_{\boldsymbol{x},0\to\beta})\chi_r(W_{\boldsymbol{x}+\hat{i},0\to\beta})\right\}$$
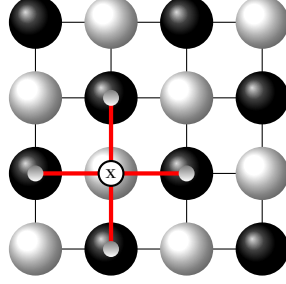
(6.31)

Figure 6.3: Polyakov loop interactions in the Green-Karsch effective theory at leading order in the inverse coupling are shown on the left for a $2d$-lattice. An even-odd partitioning of the lattice facilitates the numerical evaluation of the model.

where neighboring Polyakov loops are coupled via their characters in all representations r. At strong coupling $\beta_L \ll 1$ higher representations are suppressed due to the prefactor z_r and only the contribution of the fundamental representation $r = 1$ is retained. By choosing the following parametrization for the fundamental representation

$$W = e^{\frac{i}{2}\phi \boldsymbol{n}\cdot\boldsymbol{\tau}} = \left(\cos\frac{\phi}{2}\right)\mathbf{1} + i\left(\sin\frac{\phi}{2}\boldsymbol{n}\cdot\boldsymbol{\tau}\right), \quad dW = \frac{1}{4\pi^2}d\phi d\Omega(\boldsymbol{n})\left(\sin\frac{\phi}{2}\right)^2 \tag{6.32}$$

where $\boldsymbol{n}$ is an arbitrary unit vector and noting that the fundamental character is given by

$$L_{\boldsymbol{x}} = \chi_1(W_{\boldsymbol{x},0\rightarrow\beta}) = 2\left(\cos\frac{\phi}{2}\right) \tag{6.33}$$

the partiton function of the Green-Karsch effective theory for SU(2) is brought into an exceedingly simple form reminiscent of the partition function for a lattice of continuous Ising spins

$$Z_{GK} = \prod_x \int dL_{\boldsymbol{x}}\sqrt{1 - L_{\boldsymbol{x}}^2} \, \exp\beta' \sum_i L_{\boldsymbol{x}}L_{\boldsymbol{x}+\boldsymbol{i}}. \tag{6.34}$$

where $\beta' = 4z_1^{N_\tau} \simeq 4(\beta/4)^{N_\tau}$. It is straightforward to implement this model numerically using the Metropolis algorithm. The update of a single site $\boldsymbol{x}$ consists in drawing the new character $L_{\boldsymbol{x}}'$ from a uniform probability distribution defined on the interval $[-1, 1]$ and accepting the suggested change with probability:

$$P_A(L_{\boldsymbol{x}}' \leftarrow L_{\boldsymbol{x}}) = \min\left(1, \frac{w(L_{\boldsymbol{x}}')}{w(L_{\boldsymbol{x}})}\right) = \min\left(1, \sqrt{\frac{1 - (L_{\boldsymbol{x}}')^2}{1 - (L_{\boldsymbol{x}})^2}}\exp\left\{\beta'(L_{\boldsymbol{x}}' - L_{\boldsymbol{x}})\sum_{\pm i}L_{\boldsymbol{x}+\boldsymbol{i}}\right\}\right). \tag{6.35}$$

An iteration of the algorithm consists in performing a successive update of the characters at all lattice sites. A parallel implementation of this algorithm is realized by alternating between even and odd lattice sites. As illustrated in figure 6.3, different elements belonging to the same set of lattice sites are decoupled in the action making it possible to perform a parallel update of all sites belonging to the same set. Both actions were simulated on 3-dimensional lattices with volumes $V/a^3 = 20^3, 40^3$ and 100^3. Up to 100 000 iterations of the Metropolis algorithm were performed
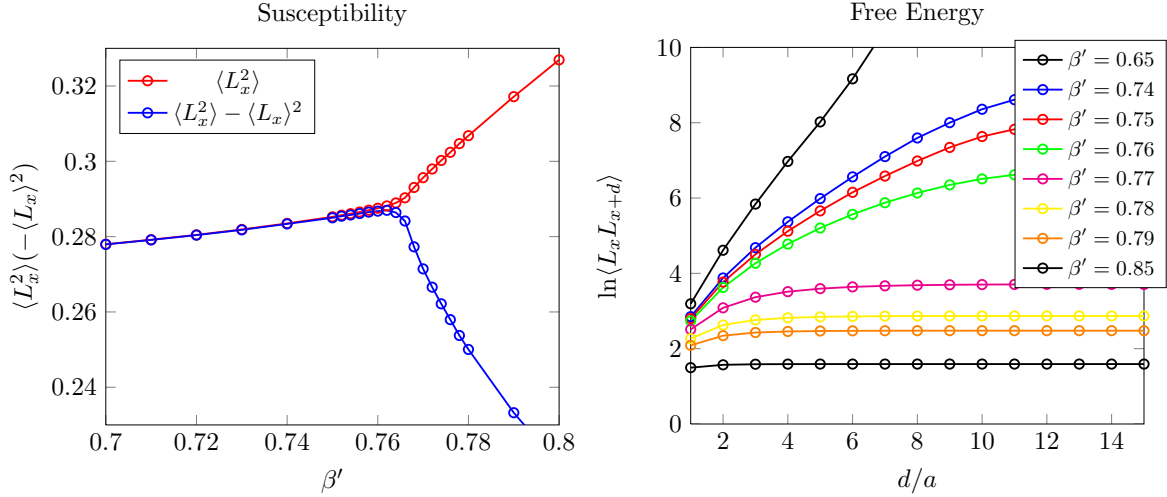
Figure 6.4: Polyakov loop susceptibility in dependence of the lattice coupling β' (left) and free energy in dependence of the distance d for various couplings (right) in the Green-Karsch effective theory on a lattice with volume $V/a^3 = 40^3$.

on each lattice for different choices of β'. A measurement was performed every 20 iterations of the algorithm. The first 200 measurements were omitted to reduce errors introduced by the burn-in of the Monte-Carlo. The results for this simple model are briefly summarized in the following to prepare the ground for a measurement of free energies in full Yang-Mills theory.

- The *Polyakov Loop Susceptibility* χ_P is defined as [$\langle \ldots \rangle_M$ indicates an averaging over the Markov chain and $\langle \ldots \rangle_V$ an averaging over the lattice volume]:

$$\chi_P = \langle \langle L_{\boldsymbol{x}}^2 \rangle_V - \langle L_{\boldsymbol{x}} \rangle_V^2 \rangle_M \tag{6.36}$$

  As discussed in the first chapter the expectation value of the Polyakov loop $\langle L_{\boldsymbol{x}} \rangle_V$ is expected to become finite beyond the critical temperature due to the spontaneous breaking of the Z(2) symmetry in the full theory. These expectations are confirmed with the susceptibility χ_P showing a peak at the critical coupling $\beta'_c \simeq 0.765$. This corresponds to a critical coupling $\beta_{Lc} = 1.75$ on a coarse $N_\tau = 2$ lattice which is close to the observed value of $\beta_{Lc} = 1.875$ [63] in full Yang-Mills theory.

- The (average) *free energy* $F(r)$ is defined as the logarithm of the Polyakov loop correlator

$$\beta' F(r) = \ln \langle L_{\boldsymbol{x}} L_{\boldsymbol{x}+r} \rangle \tag{6.37}$$

  where r is the distance between both loops (see the next section). As expected in full Yang-Mills theory the free energy rises linearly with the distance r in the confined phase. Above β'_c the free energy takes the form of a Debye screened potential. (4.2).

These initial observations confirm an analogous behavior of the Polyakov loop in the Green-Karsch effective theory and full Yang-Mills theory. For a more detailed analysis see [64]. The statistical

error of *primary quantities* like χ_P, which are obtained by averaging over the elements of a Markov chain, can be estimated by calculating the standard deviation and taking into account the respective autocorrelation time. The error of *secondary quantities* like F_3, defined as functions of primary quantities, is obtained using *Jacknife analysis*. Let $g : \Omega \to \mathbb{R}$ be a primary quantity and $f(g) : \Omega \to \mathbb{R}$ be a function of g. The statistical variance $\sigma^2_{f(g)}$ of f is then defined by the relation [g_i is the measurement i of g]:

$$\sigma^2_{f(g)} = \frac{m-1}{m} \sum_{i=1}^{m} \left(f(\langle g \rangle_i) - f(\langle g \rangle) \right)^2 \quad \text{where} \quad \langle g \rangle_i = \sum_{j=1}^{b} g_{(i-1)b+j}. \tag{6.38}$$

$n = mb$ is the number of measurements and $b \in \mathbb{N}$ is called the *bin size*. The errors for the previously discussed results are negligable.

6.5   Free Energy in Lattice Yang-Mills Theory

The aim of the measurement presented in this section is to determine the thermodynamic free energy of a static charge pair consisting of a fundamental color charge q and an anti-fundamental charge $\bar{q}$ located at the set of positions $\{\boldsymbol{x}, \boldsymbol{y}\} \in \mathbb{R}^3$. The measurement is part of an ongoing project to determine the electric screening mass m_D. It is included in this thesis to supplement the perturbative picture of heavy quark bound states developed in previous chapters with a numerical study of the corresponding thermodynamic free energy. Note that this quantity is *not* identical to the binding energy defined in chapter 4 as has been pointed on various occasions. The partition function of thermal Yang-Mills theory in the presence of the static $q\bar{q}$-pair takes the following form (for full QCD see McLerran,Svetitsky [65]):

$$\frac{Z_{q\bar{q}}}{Z} = \frac{1}{Z} \int [\mathrm{D}A] \mathrm{e}^{-S_{YM}} W^+_{0\to\beta,\boldsymbol{x}} W_{0\to\beta,\boldsymbol{y}} \quad \text{where} \quad Z = \int [\mathrm{D}A] \, \mathrm{e}^{-S_{YM}}. \tag{6.39}$$

S_{YM} is the action of Yang-Mills theory formulated on a euclidean space with a compactified temporal dimension of extent $\beta = 1/T$. $W_{0\to\beta,\boldsymbol{x}}$ is a Polyakov loop at the position $\boldsymbol{x} \in \mathbb{R}^3$. The trace of the Polyakov loop is denoted as

$$L_{\boldsymbol{x}} = \frac{1}{N} \mathrm{Tr} \, W_{0\to\beta,\boldsymbol{x}} \tag{6.40}$$

continuing the notation introduced in chapter 2. Following Brown, Weisberger [66] and Nadkarni [67] the partition function is often decomposed into color channels

$$Z_{q\bar{q}} = Z^S_{q\bar{q}} P^C_S + Z^A_{q\bar{q}} P^C_A \tag{6.41}$$

where the projectors P^C_X on singlet (S) and adjoint (A) components are defined as:

$$P^C_S = \frac{1}{N^2} 1 \times 1 - \frac{2}{N} \overline{T^a} \times T^a, \quad P^C_A = \frac{N^2-1}{N^2} 1 \times 1 + \frac{2}{N} \overline{T^a} \times T^a, \quad \overline{T^a} = T^{a*} \tag{6.42}$$

Both components of the partition function are obtained by projection on the respective charge sector

$$\frac{Z^X_{q\bar{q}}}{Z} = \frac{1}{Z} \frac{\mathrm{Tr} \, P^C_X Z^X_{q\bar{q}}}{\mathrm{Tr} \, P^C_X} \tag{6.43}$$

which yields the following representations:

$$
\begin{aligned}
\frac{Z_{q\bar{q}}^{S}}{Z} &= \frac{1}{N}\mathrm{Tr}\langle W_{0\rightarrow\beta,\boldsymbol{x}}^{+}W_{0\rightarrow\beta,\boldsymbol{y}}\rangle \\
\frac{Z_{q\bar{q}}^{A}}{Z} &= \frac{1}{N^{2}-1}\langle L_{\boldsymbol{x}}^{+}L_{\boldsymbol{y}}\rangle - \frac{1}{N(N^{2}-1)}\mathrm{Tr}\langle W_{0\rightarrow\beta,\boldsymbol{x}}^{+}W_{0\rightarrow\beta,\boldsymbol{y}}\rangle.
\end{aligned}
\tag{6.44}
$$

The contribution of the Polyakov loop correlator is referred to as the average component (AV):

$$
\frac{Z_{q\bar{q}}^{AV}}{Z} = \frac{1}{N^{2}}\langle L_{\boldsymbol{r}}L_{\boldsymbol{0}}^{+}\rangle.
\tag{6.45}
$$

Contrary to the expectation that this decomposition yields the partition functions for singlet and adjoint states, it was shown by Philipsen and Jahn [68] that both components receive only contributions from the singlet state. To illustrate this in a lattice formalism the transfer matrix in the presence of a static $q\bar{q}$ pair is introduced

$$
\hat{T} = \hat{T}_{0}\hat{P}^{S,A}, \qquad \hat{T}_{0} = \mathrm{e}^{-a\hat{H}_{0}},
\tag{6.46}
$$

where $\hat{T}_{0}$ is the transfer matrix [69, 70] for lattice Yang-Mills theory in a temporal gauge and $\hat{H}_{0}$ the Kogut-Susskind Hamiltonian [71]. The projection operators $\hat{P}^{S,A}$, used here, annihilate Hilbert space states not transforming in the singlet or adjoint representation under a gauge transformation acting on the charge positions $\{\boldsymbol{x},\boldsymbol{y}\}\in\mathbb{Z}^{d}$. Both projection operators are listed in the following

$$
\hat{P}_{\alpha\beta\mu\nu}^{S} = \int[\mathrm{D}g]g_{\alpha\beta}^{+}(\boldsymbol{x})g_{\mu\nu}(\boldsymbol{y})\hat{R}(g),
\tag{6.47}
$$

$$
\hat{P}_{\alpha\beta\mu\nu ab}^{A} = \int[\mathrm{D}g]g_{\alpha\beta}^{+}(\boldsymbol{x})g_{\mu\nu}(\boldsymbol{y})D_{ab}^{A}(g(\boldsymbol{x}_{0}))\hat{R}(g),
\tag{6.48}
$$

where $g\in\mathbb{Z}^{d+1}\times\mathrm{SU}(N)$ is a gauge transformation imposed by the operator $\hat{R}(g)$ and $\boldsymbol{x}_{0}\in\mathbb{Z}^{d}$ is referred to as location of the adjoint state. The representation matrices of the adjoint representation are
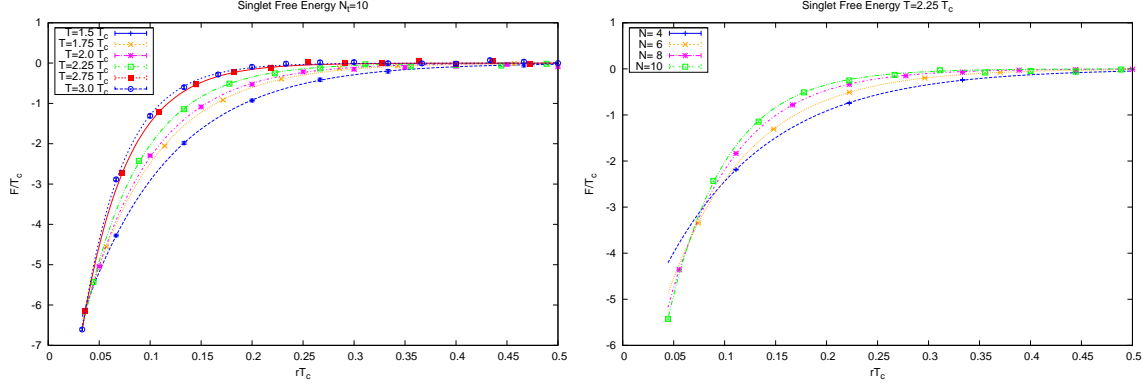
$$
D_{ab}^{A}(g) = 2\mathrm{Tr}(g^{+}T^{a}gT^{b}).
\tag{6.49}
$$

Using these projectors the average component of the partition function can now be written as [72]

$$
\frac{1}{N^{2}}\langle L_{\boldsymbol{x}}^{+}L_{\boldsymbol{y}}\rangle = \frac{1}{N^{2}Z}\sum_{\alpha\beta}\mathrm{Tr}\left\{\hat{T}_{0}^{N_{\tau}}\hat{P}_{\alpha\alpha\beta\beta}^{S}\right\}
\tag{6.50}
$$

where N_{τ} is the temporal lattice extent. Let $\psi_{\alpha\beta}(U)$ be a superposition of field eigenstates which is referred to as the *wavefunction*. The Hilbert space projector on singlet eigenstates annihilates all wavefunctions not transforming as $\psi_{\beta\mu}(U^{g}) = g(\boldsymbol{x})_{\beta\gamma}\psi_{\gamma\delta}(U)g_{\delta\mu}^{+}(\boldsymbol{y})$ where U^{g} is the transformed field eigenstate. Using the fact that the Kogut Susskind Hamiltonian commutes with the projector the average component of the partition function can be rewritten as a trace over singlet energy eigenstates

$$
\frac{1}{N^{2}}\langle L_{\boldsymbol{x}}^{+}L_{\boldsymbol{y}}\rangle = \frac{1}{N^{4}}\sum_{n\alpha\beta}|\langle n_{\alpha\beta}|n_{\beta\alpha}\rangle|^{2}\mathrm{e}^{-E_{n}/T} = \frac{1}{N^{2}}\sum_{n}\mathrm{e}^{-E_{n}/T}.
\tag{6.51}
$$

N_τ	$T/T_c = 1.5$	$T/T_c = 1.75$	$T/T_c = 2.0$	$T/T_c = 2.25$	$T/T_c = 2.5$	$T/T_c = 2.75$	$T/T_c = 3.0$
4	5.877	5.960	6.038	6.111	6.181	6.246	6.307
6	6.127	6.231	6.325	6.410	6.486	6.554	6.614
8	6.328	6.439	6.535	6.616	6.687	6.747	6.800
10	6.490	6.598	6.688	6.762	6.825	6.879	6.925

Figure 6.5: *Top left:* The temperature dependence of the singlet free energy for $N_\tau = 10$. The screening mass, obtained by fitting the free energy against an exponential, depends linearly on the temperature. *Top right:* The N_τ dependence of the result is shown for $T = 2.25T_c$. The free energy vanishes increasingly for finite r due to the diverging self energy of Wilson lines. *Bottom:* The temperature dependent lattice couplings as obtained from the non-perturbative $\beta-$ function (6.53).

The correlator of traced Polyakov loops, thus, does *not* parametrize contributions of adjoint states to the partition function. Note also that the correlator defining the 'singlet' component of the partition function is not gauge invariant. A gauge invariant representation for the singlet component is obtained by connecting the Polyakov loops with the Wilson line $W_{0,\boldsymbol{x}\to\boldsymbol{y}}$ to arrive at a periodic Wilson loop [68]:

$$\text{Tr}\langle W_{0\to\beta,\boldsymbol{x}}^+ W_{0\to\beta,\boldsymbol{y}}\rangle \to \text{Tr}\langle W_{0\to\beta,\boldsymbol{x}}^+ W_{0,\boldsymbol{x}\to\boldsymbol{y}} W_{0\to\beta,\boldsymbol{y}} W_{0,\boldsymbol{x}\to\boldsymbol{y}}^+\rangle. \tag{6.52}$$

To measure the correlators, associated with the would be singlet and average components of the partition function, on the lattice a suitable scheme is required which relates the physical temperature in the continuum to the lattice coupling β_L of the discretized system. The scheme used in the

N_τ	4	6	8	10
β_{Lc}	5.690(5)	5.89(1)	6.055(6)	6.201(5)

Table 6.1: Critical coupling for N=3 lattice Yang-Mills theory with Wilson action in 3+1 dimensions [73].

following relies on the following relation obtained in [73] using non-perturbative renormalization techniques

$$\log\frac{T}{T_c} = 1.7139(\overline{\beta}_L - \overline{\beta}_{Lc}) - 0.8155(\overline{\beta}_L^2 - \overline{\beta}_{Lc}^2) + 0.6667(\overline{\beta}_L^3 - \overline{\beta}_{Lc}^3) \tag{6.53}$$
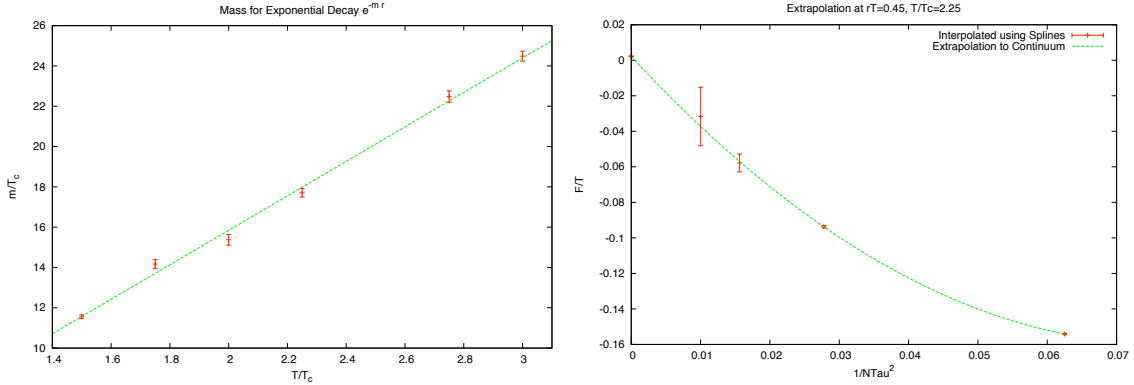
Figure 6.6: *Left:* At first sight the screening masses, obtained on $N_\tau = 10$ lattices by fitting the free energy against an exponential decay, show the desired linear temperature dependence. *Right:* A continuum extrapolation of the free energy has been attempted by fitting the r-dependence of the free energy at a given temperature with splines for each N_τ. The results indicate that the free energy vanishes in the continuum limit due to a diverging screening mass.

where $\overline{\beta} = \beta - 6$. This β-function was obtained on lattices with a temporal extent of $N_\tau \in \{4, 6, 8, 10\}$ and three spatial dimensions of extent $N_i = 3N_\tau, i \in \{1, 2, 3\}$ in the physical temperature range $0.5T_c < T < 3T_c$. This layout has also been used in the measurements presented in the following. The critical lattice couplings entering the β-function are listed in table 6.1 and where obtained by measuring the triplet loop susceptibility [73]. To measure the so called singlet and average free energies

$$F_S(r) = \ln\mathrm{Tr}\langle W^+_{0\to\beta,\boldsymbol{x}} W_{0\to\beta,\boldsymbol{y}}\rangle, \quad F_{AV}(r) = \ln\langle L^+_{\boldsymbol{x}} L_{\boldsymbol{y}}\rangle, \tag{6.54}$$

where $r = |\boldsymbol{x} - \boldsymbol{y}|$, the physical temperature is varied from $T = 1.5T_c$ to $T = 3.0T_c$ in steps of $\Delta_T = 0.25T_c$ on lattices with temporal extent $N_\tau \in \{4, 6, 8, 10\}$. The β-function (6.53) has been solved for β_L to obtain the corresponding lattice couplings listed in figure 6.5. 15000 iterations of the previously described Cabbibo-Marinari heatbath algorithm were performed for each lattice configuration with a measurement taken every 10 configurations. The first 1000 configurations were omitted. Since the average component of the free energy has been extensively analyzed, the following discussion will focus on the singlet free energy as obtained by taking the logarithm of the expectation value of the periodic Wilson loop. The free energy is normalized by demanding $F(r \to \infty) = 0$. The Debye screened potential (4.2) does not provide an acceptable fit to lattice data for the periodic Wilson loop. Instead an exponential decay is observed with the screening mass having the expected linear temperature dependence as shown in figure 6.5. A continuum extrapolation of the free energy has been attempted by fitting the r-dependence of the free energy at a given temperature with splines for each N_τ. The singlet free energy, as obtained here from the periodic Wilson loop, is found to vanish in the continuum limit due to a diverging screening mass. This behavior is caused by a diverging self energy of the Wilson lines [74] which needs to be properly renormalized to extract physical screening masses. Suitable schemes are discussed in [74]. The measurements presented here are part of an ongoing project and serve to supplement previous discussions of $q\bar{q}$-states with a non-perturbative point of view and as an illustration of lattice techniques. The interested reader is referred to [75] for final results.

7 CLASSICAL LATTICE MODEL FOR HIGH TEMPERATURE QCD

Simplicity is the ultimate sophistication.

Leonardo da Vinci

This chapter focuses on the construction of a simple lattice model for the dynamics of soft gauge fields in the Yang-Mills plasma and discusses the matching of this model to the full continuum theory. Significant advances in the numerical implementation of this model were made in the course of the research leading to this thesis and will be highlighted in later parts of this chapter.

7.1 Classical Approximation of Quantum Fields

To discuss the classical limit of bosonic quantum field theory a general system with the d-dimensional partition function

$$Z = \mathrm{Tre}^{-\beta \hat{H}(\{\hat{\phi}_i, \hat{\pi}_i\})} \tag{7.1}$$

is considered, where the Hamiltonian $\hat{H}$ is a function of the set of bosonic field operators $\{\phi_i(x)\}, i \in \{1, \ldots, n\}$ and conjugate momentum operators $\{\pi_i(x)\}$ in the Heisenberg picture satisfying the commutation relations:

$$[\hat{\phi}_i(x), \hat{\pi}_j(y)] = \mathrm{i}\hbar \delta_{ij}\delta(x - y). \tag{7.2}$$

As discussed in chapter 3, the thermal nature of the system manifests itself in the bare real-time propagators of the fields by the appearance of a symmetric component proportional to the Bose distribution:

$$n_B(\omega) + \frac{1}{2} = \frac{T}{\hbar\omega} + \frac{1}{12}\frac{\hbar\omega}{T} + \ldots \tag{7.3}$$

The reduced Planck constant $\hbar = 6.582 \times 10^{-25} GeVs$ is shown explicitly in the high temperature Laurent expansion of the Bose distribution. The expansion parameter for the perturbative series is $\hbar g^2$. For quantities insensitive to the energy region $\omega \geq T$ the perturbative series can thus be rearranged into a systematic expansion in $\hbar$ with the tree level contribution obtained in the limit $\hbar \to 0$ consisting of the sum of all terms proportional to

$$g^{2m}\prod_{j=1}^{m}\left(\frac{T}{\omega_j}\right), \quad m \in \mathbb{N} \quad \text{(Classical Contributions).} \tag{7.4}$$

The classical theory resums all diagrams with $2m$ internal vertices and the maximal number of m insertions of the symmetric propagator. To derive a complete set of equations describing the time evolution of the system in the classical limit, the Heisenberg picture equations of motion for the field operators and conjugate momentum operators are evaluated:

$$\frac{\mathrm{d}}{\mathrm{d}t}\hat{\varphi}_i(x) = \frac{\mathrm{i}}{\hbar}[\hat{H}, \hat{\varphi}_i(x)] \quad \text{and} \quad \frac{\mathrm{d}}{\mathrm{d}t}\hat{\pi}_i(x) = \frac{\mathrm{i}}{\hbar}[\hat{H}, \hat{\pi}_i(x)]. \tag{7.5}$$

The commutators can be evaluated in the classical limit $\hbar \to 0$ by expanding the Hamiltonian in the field and momentum operators and subsequently employing the following convenient set of

relations

$$\lim_{\hbar \to 0} \frac{i}{\hbar} [\hat{\pi}_i^n(x), \hat{\varphi}_j(y)] = n\hat{\pi}_i^{n-1}(x)\delta_{ij}\delta(x-y) \quad \text{and} \quad \lim_{\hbar \to 0} \frac{i}{\hbar} [\hat{\varphi}_i^n(x), \hat{\pi}_j(y)] = -n\hat{\varphi}_i^{n-1}(x)\delta_{ij}\delta(x-y),$$
(7.6)

where $\in \mathbb{N}$ is the order parameter of the series. The commutators (7.5) in the classical limit are therefore identical to functional derivatives of the operator function $\hat{H}(\{\varphi_i(x), \pi_i(x)\})$ with respect to individual field or momentum operators:

$$\lim_{\hbar \to 0} \frac{i}{\hbar} [\hat{H}, \hat{\varphi}_i(x)] = \frac{\delta \hat{H}}{\delta \hat{\pi}_i(x)} \quad \text{and} \quad \lim_{\hbar \to 0} \frac{i}{\hbar} [\hat{H}, \hat{\pi}_i(x)] = -\frac{\delta \hat{H}}{\delta \hat{\varphi}_i(x)}.$$
(7.7)

The Heisenberg equations are therefore identical to the classical Hamiltonian equations of motion in an operator form in the limit $\hbar \to 0$:

$$\frac{d}{dt}\hat{\varphi}_i(x) = \frac{\delta \hat{H}}{\delta \hat{\pi}_i(x)} \quad \text{and} \quad \frac{d}{dt}\hat{\pi}_i(x) = -\frac{\delta \hat{H}}{\delta \hat{\varphi}_i(x)}.$$
(7.8)

To complete the transition to a classical theory a phase space must be introduced. In the limit $\hbar \to 0$ the operators $\hat{\varphi}, \hat{\pi}$ commute and field eigenstates $|\varphi\rangle \in \mathscr{H}_\varphi$ are orthogonal to momentum eigenstates $|\pi\rangle \in \mathscr{H}_\pi$:

$$[\hat{\varphi}_i(x), \hat{\pi}_j(y)] = 0 \quad \text{and} \quad \langle \varphi | \pi \rangle = 0.$$
(7.9)

The Hilbert spaces $\mathscr{H}_\varphi = span\{|\varphi\rangle\}$ and $\mathscr{H}_\pi = span\{|\pi\rangle\}$ spanned by field and momentum eigenstates have become distinct. Since the set of operator $\{\hat{\varphi}_i(x), \hat{\pi}_i(x)\}$ forms a complete set of commuting hermitian operators characterizing the system the Hilbert space of the classical theory is the Fock space:

$$\mathscr{F}_{cl} = \mathscr{H}_\varphi \times \mathscr{H}_\pi.$$
(7.10)

This space defined at some inital time $t = 0$ is the space of all initial conditions to the classical time evolution. By acting on individual states $\mathscr{F}_{cl}$ with the Heisenberg equations (7.8) a classical phase space trajectory obeying the Hamiltonian equations of motion is obtained. To summarize the following observations have been made:

- The tree level contribution in a systematic expansion of the quantum theory in $\hbar$ is identical to the classical theory defined by the respective Lagrangian.

- The physics at soft energy scales $\omega \ll T$ is predominantly classical. All Feynman diagrams with a maximal number of thermal (symmetric) insertions are resummed by the classical theory.

- A theory where soft and hard scales are cleanly separated is purely classical in the low energy regime.

The last remark indicates that a classical approximation of Yang-Mills theory must be applied with caution due to the interdependence of hard and soft momentum scales. A detailed discussion of the approximation will be given in the following sections.

7.2   Application to Soft Scales in the Yang-Mills Plasma

As a starting point for the construction of a classical model for Yang-Mills theory at temperatures $T \gg T_c$ the characteristic gluon momentum scales are briefly reviewed again in the following:

1. *Hard Momentum Scale: $k \sim T$*

   The characteristic momentum scale for gluons in a Yang-Mills plasma corresponds to the temperature T of the medium. The corresponding length scale $1/T$ is the average inter particle spacing.

2. *Electric Scale: $k \sim gT$*

   The thermal mass of soft longitudinal gluons is given by the Debye mass $m_D \sim gT$. The exchange of longitudinal gluons is significantly suppressed below this threshold which translates into a suppression of electrical interactions at distances larger than $1/m_D$.

3. *Magnetic Scale: $k \sim g^2T$*

   Magnetic interactions, which are the most far reaching interaction in the Yang-Mills plasma, thus experience a dynamical screening over distances larger than $1/g^2T$.

The electric and magnetic scales are collectively referred to as *soft scales.* By choosing the separation scale $gT < \Lambda_{cl} < T$ momentum space is partitioned into regions with high and low gluon occupation numbers. Due to the thermal screening of longitudinal and transverse gluon modes, the physics remains weakly coupled at low energies. The soft scales in the Yang-Mills plasma can, however, not be decoupled from the hard momentum scale, since the internal loops of diagrams with soft external momenta are often dominated by the exchange of hard gluons [18], where the hard scale serves as a natural cutoff. Many quantities are insensitive to the exact nature of the thermal cutoff however and can be reproduced in the context of a classical theory with sharp momentum cutoff $\Lambda_{cl} \ll T$. The partition function of d-dimensional classical Yang-Mills theory at finite temperature has the following form

$$Z_{cl} = \int [\mathrm{D}A][\mathrm{D}E]\delta(\mathrm{D}_i E^i)\mathrm{e}^{-\beta H_{YM}}, \tag{7.11}$$

where a temporal gauge has been chosen to introduce a canonical formalism, where gauge fields A_i are accompanied by conjugate momenta E_i and classical statistical mechanics can be applied in a straightforward manner. The gauge is imposed by the non-abelian Gauss constraint $D_i E^i = 0$. All fields are defined at the Minkowskian time $t = 0$. The Hamiltonian H_{YM} of the theory is given by

$$H_{YM} = \int \mathrm{d}^3x \mathrm{Tr}\left\{-E_i E^i + \frac{1}{2}F_{ij}F^{ij}\right\}, \tag{7.12}$$

where color electrical fields appear as the conjugate momenta to gauge fields. Time dependent correlation functions are obtained by evolving ensemble configurations with the Euler-Lagrange equations of motion:

$$\dot{E}_i = -\mathrm{D}^j F_{ji} \quad \text{and} \quad \dot{A}_i = E_i. \tag{7.13}$$

The model will be extended in the next chapter to take into account leading order interactions with hard (sparsely populated) modes in a generic non-equilibrium setting. In the remaining part of this chapter the classical model is discussed choosing a hypercubic momentum cutoff to facilitate a numerical implementation of the model. Techniques of this type were pioneered by Grigoriev and Rubakov [76].
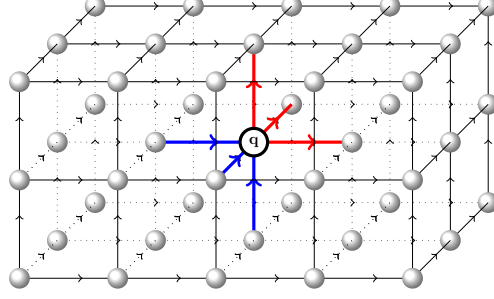
Figure 7.1: Illustration of Gauss's law on the lattice. The difference between the electric flux into a lattice site (blue) and the electric flux leaving a lattice site (red) is given by the charge $q(t) = j^0(x, t)$.

7.3   Formulation on a Hamiltonian Lattice

By restricting momenta to a Brillouin zone $k_i < \Lambda_{cl}$ a d-dimensional classical lattice model with uniform lattice spacing $a = \pi/\Lambda_{cl}$ in each spatial direction and the following partition function is obtained:

$$Z_L = \int [\mathrm{D}U] \int [\mathrm{D}E] \ \delta(G) \ \mathrm{e}^{-\beta H_L}. \tag{7.14}$$

The Hamiltonian H_L of the lattice model is chosen to take the form

$$H_L(t) = \sum_x \left\{ a^3 \mathrm{Tr} E_i(x, t) E_i(x, t) + \beta_L \sum_{i<j} \left\{ 1 - \frac{1}{N} \mathrm{Re} \ \mathrm{Tr} U_{ij}(x, t) \right\} \right\}, \tag{7.15}$$

where $\beta_L = 2N/ag^2$. Spatial gauge fields $\{A_i(x, t)\}$ are discretized as lattice links $U_i(x, t)$ in the fundamental representation according to (6.1). The magnetic part of the Hamiltonian H_L corresponds to a d-dimensional Wilson action (6.6). Since the time coordinate t remains continuous the color electric field $E_i(x, t) = E_i^a(x, t) T^a \in \mathrm{su}(N)$ is discretized as an element of the fundamental Lie algebra defined at each lattice site from the relation:

$$\dot{U}_i(x, t) = \mathrm{i} g a E_i(x, t) U_i(x, t). \tag{7.16}$$

It is straightforward to show that this relation reduces to $E_i = \dot{A}_i$ in the continuum limit $a \to 0$. The generators T^a are normalized according to the lattice convention (6.2). The partition function is defined at the time $t = 0$ and the integration is performed over all gauge links $\{U_i(x, 0)\}$ using the Haar measure and over the adjoint components of all electrical fields $\{E_i(x, 0)\}$. A temporal gauge is enforced by requiring a discretized analogue of Gauss law (2.15) to hold (see figure 7.1)

$$G(x, t) = \sum_i \left\{ E_i(x, t) - U_{-i}(x, t) E_i(x - \hat{i}, t) U_{-i}^+(x, t) \right\} = j^0(x, t). \tag{7.17}$$

The color current $j_\mu(x, t)$ is defined at each lattice site and vanishes in the absence of external charges. The Gauss constraint on the lattice forces the difference between the (parallel transported) electric flux flowing towards and away from a lattice site site to equal the charge residing at the respective site. The lattice setup discussed in this section corresponds to the Hamiltonian lattice formulation [71].

7.4   Classical Equations of Motion

The Euler-Lagrange equations of motion for the electrical fields of the classical lattice model [77] are obtained by varying the action of the lattice model

$$S_L = \int \mathrm{d}t \sum_x \mathscr{L}(x,t) \tag{7.18}$$

where $\mathscr{L}(x,t)$ is the Lagrangian density

$$\mathscr{L}(x,t) = \frac{a}{g^2 T} \mathrm{Tr} \dot{U}_i^+(x,t)\dot{U}_i(x,t) - \beta_3 \sum_{i<j} \left\{ 1 - \frac{1}{N} Re Tr U_{ij}(x,t) \right\} \tag{7.19}$$

with respect to the complex components $U_{i(ab)}$ and $U_{i(ab)}^*$ of link matrices under the unitarity constraint $U_i U_i^+ = 1$. By parametrizing the infinitesimal variation of a link matrix in the form

$$\mathrm{d}U_i(x,t) = \mathrm{i}T^a \mathrm{d}\tilde{A}_i^a(x,t)U_i(x,t) \tag{7.20}$$

the following Euler-Lagrange equation is derived as a solution of the variational problem $\delta S_L = 0$:

$$\mathrm{Tr}\left\{ \left(\frac{\mathrm{d}}{\mathrm{d}t}\frac{\partial \mathscr{L}}{\partial \dot{U}_i} - \frac{\partial \mathscr{L}}{\partial U_i} \right)^T T^a U_i - \left(\frac{\mathrm{d}}{\mathrm{d}t}\frac{\partial \mathscr{L}}{\partial \dot{U}_i^*} - \frac{\partial \mathscr{L}}{\partial U_i^*} \right) U_i^+ T^a \right\} = 0. \tag{7.21}$$

Throughout this section the notation $(\partial f/\partial U^{(*)})_{ab} = \partial f/\partial U_{ab}^{(*)}$ will be used to write the derivative of a function $f : SU(N) \to \mathbb{R}$ with respect to the components of a link $U \in \mathrm{SU}(N)$ in a matrix form. Using the definition (7.16) of electric fields the following expressions are obtained

$$\left(\frac{\mathrm{d}}{\mathrm{d}t}\frac{\partial \mathscr{L}}{\partial \dot{U}_i} \right)^T = -\mathrm{i}\frac{a^2}{gT}\frac{\mathrm{d}}{\mathrm{d}t}(U_i^+ E_i), \quad \frac{\mathrm{d}}{\mathrm{d}t}\frac{\partial \mathscr{L}}{\partial \dot{U}_i^*} = \mathrm{i}\frac{a^2}{gT}\frac{\mathrm{d}}{\mathrm{d}t}(E_i U_i) \tag{7.22}$$

which introduce the time derivative of color electric fields into the Euler Lagrange equation. Derivatives of the Lagrangian density with respect to individual links $U_i(x,t)$ reduce to the sum of staples $S_i(x,t)$ (6.21) multipliying this link in the Wilson part of the action:

$$\frac{\partial \mathscr{L}}{\partial U_i} = \frac{\beta_L}{2N}S_i \quad \text{and} \quad \frac{\partial \mathscr{L}}{\partial U_i^*} = \frac{\beta_L}{2N}S_i^*. \tag{7.23}$$

Upon inserting the preceding expressions into the Euler-Lagrange equation the following intermediate result is obtained

$$\frac{2a^2}{g}\left\{ \mathrm{Tr}(T^a \dot{E}_i) + \mathrm{Re}\ \mathrm{Tr}(T^a \dot{U}_i^+ E_i) \right\} = \frac{\beta_L}{N}\sum_{|j|\neq i} \mathrm{Im}\ \mathrm{Tr}(T^a U_{ij}), \tag{7.24}$$

where the sum of staples has been closed to a sum over plaquettes U_{ij} by multiplication with the missing link. From the identity

$$\mathrm{Re}\ \mathrm{Tr}(T^a U_i U_i^+ E_i) = ga E_i^b E_i^c \mathrm{Im}\ \mathrm{Tr}(T^a T^b T^c) \tag{7.25}$$
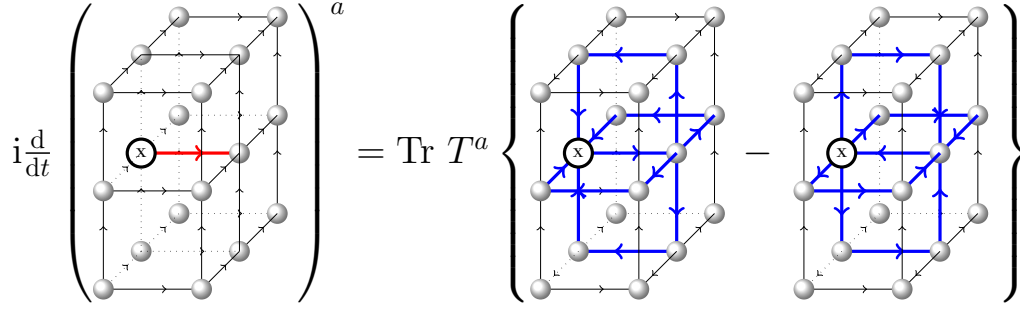
Figure 7.2: The equation of motion for the color electric field $E_1(x)$ (red) on a 3-dimensional lattice. The trace is taken over the difference of the sum of all plaquettes including the link $U_1(x)$ (blue) circled in opposite directions.

it is evident that the second component of the bracketed expression vanishes as the contraction of a symmetric and antisymmetric tensor. The following equation of motion is thus obtained for color electric fields:

$$a^3 g \dot{E}_i^a(x,t) = 2 \sum_{|j| \neq i} \text{Im Tr}(T^a U_{ij}(x,t)). \qquad (7.26)$$

For practical purposes it is desirable to scale out the lattice spacing as well as gauge coupling by introducing the following rescalings

$$a^2 g E_i \to E_i \quad \text{and} \quad \frac{t}{a} \to t \qquad (7.27)$$

which need to be taken into account in the construction of any observable to be investigated in the context of this model. To summarize classical Yang-Mills theory on a Hamiltonian lattice is characterized by the equations of motion

$$\dot{U}_i(x,t) = iE_i(x,t)U_i(x,t) \qquad \text{(Faraday's law of induction)} \qquad (7.28)$$

$$\dot{E}_i^a(x,t) = 2 \sum_{|j| \neq i} \text{Im Tr} \{T^a U_{ij}(x,t)\} \qquad \text{(Ampere's circuital law)} \qquad (7.29)$$

under a Gauss constraint which needs to be satisfied by the initial lattice configurations at $t = 0$:

$$\sum_i \left\{ E_i(x,t) - U_{-i}(x,t)E_i(x - \hat{i},t)U_{-i}^+(x,t) \right\} = 0. \qquad (7.30)$$

It is important to note that the Gauss constraint remains satisfied during the time evolution of the system if fulfilled by the initial field configuration of the lattice system. Upon expanding the fields in the lattice spacing a it is readily shown that deviations from Gauss law in the continuum appear at $\mathcal{O}(a^2)$ in the resulting series. Since the equations of motion are obtained directly from a variation of the $\mathcal{O}(a)$ correct Wilson action any deviations of the lattice model from classical Yang-Mills theory in the continuum will appear at $\mathcal{O}(a^2)$ in a systematic expansion in the lattice spacing.

7.5   Matching to the Quantum Theory in the Continuum

To match the classical theory to quantum Yang-Mills theory with spatial momenta restricted to the Brillouin zone $k_i < \Lambda_{cl} = \frac{\pi}{a}, gT \ll \Lambda_{cl} \ll T$, a perturbative scheme briefly outlined in this section and referred to as Hard Classical Loop (HCL) perturbation theory [78, 79] is used. Spatial momenta appearing in the denominators of Greens functions are deformed by the introduction of a cubic momentum cutoff which breaks the translation invariance of the theory. To account for this situation the following notation is introduced:

$$\tilde{p}_i = \frac{2}{a}\sin\left(\frac{ap_i}{2}\right), \ \ \mathring{p}_i = \frac{1}{a}\sin\left(ap_i\right) \ \text{and} \ \ \int \mathrm{d}\boldsymbol{p} = \prod_{i=1}^{d}\int_{-\pi/a}^{\pi/a}\frac{\mathrm{d}p_i}{2\pi} \tag{7.31}$$

Here $\tilde{p}_i$ is the lattice momentum and a the lattice spacing. Correlators are calculated analogous to HTL perturbation theory [18] with ordinary momenta appearing in the resummed propagators and vertices replaced by their lattice counterparts. The ensuing modification of dispersion relations of the resummed gluon propagator results in the following hierarchy of length scales:

1. *Hard Scale a*

   Most energy resides at the cutoff scale $\sim \pi/a$ where the thermal energy distribution is cut off artificially. The lattice spacing corresponds to the typical inter-particle spacing.

2. *Electric Scale $\sqrt{a/g^2T}$*

   Beyond this length scale electrical interactions are screened due to the longitudinal gluon mass $m_{D,L}$ (see below).

3. *Magnetic Scale π/g^2T*

   Magnetic interactions, which remain the most far reaching interactions in the lattice model, are screened dynamically at this length scale. The non-perturbative physics beyond this length scale is accounted for in the classical approximation.

Since the lattice spacing is presumed to be $a \sim 1/T$ for the classical model the scale hierarchy of thermal Yang-Mills theory is reproduced. To supplement this argument with a more precise scale relation the Debye masses of the continuum and lattice theory can be equated

$$m_D^2 = \frac{N}{3}g^2T^2, \ \ \ \ m_{D,L}^2 = \frac{N\Sigma}{2\pi}\frac{g^2T}{a} \tag{7.32}$$

where $\Sigma = 3.175911536\ldots$ to fix the lattice spacing to

$$a = \frac{3}{2}\frac{\Sigma}{\pi T}. \tag{7.33}$$

The physics at the soft electric and magnetic scales matches the physics at the corresponding scales in the continuum for quantities insensitive to the hard scale. Close to the momentum cutoff the physics of the classical lattice model differs drastically from the hard scale in the continuum. The lattice counterpart to hydrodynamics is affected dramatically by the maximal deformation of momenta at this scale invalidating any measurement of the shear viscosity or related quantities. It is therefore again necessary to emphasize that the classical approximation relies on a separation of hard and soft scales which must be established for individual observables in Yang-Mills theory. Techniques to remedy this situation are discussed in chapter 9.

7.6   Statistical Ensemble as Lattice Yang-Mills Theory with adjoint Higgs

The task of implementing this model in a numerical simulation consists of generating a statistical ensemble of initial lattice configurations according to the partition function (7.14) and integrating the equations of motion for each ensemble configuration. To address the first part of the problem the partition function (7.11) of the classical model in the continuum shall serve as a starting point. The Gauss constraint can be reexpressed using the identity

$$\delta(\mathrm{D}_i E^i) = \int [\mathrm{D}\varphi] \, \exp\left\{ i\beta \int \mathrm{d}^3x \mathrm{Tr}[E^i \mathrm{D}_i\varphi] \right\}, \tag{7.34}$$

where $\varphi = \varphi^a T^a$ is a suitably scaled adjoint scalar field and $D_i\varphi = \partial_i\varphi - ig[A_i, \varphi]$ is the usual covariant derivative in the adjoint representation. A partial integration has been performed in the exponent to remove the covariant derivative from the color electric field. The partition function (7.11) is rewritten as:

$$Z_{cl} = \int [\mathrm{D}A][\mathrm{D}E][\mathrm{D}\varphi] \, \exp\left\{ -\beta \int \mathrm{d}^3\boldsymbol{x} \mathrm{Tr}\left[\frac{1}{2}F_{ij}F^{ij} - E^i(E_i + i\mathrm{D}_i\varphi) \right] \right\}. \tag{7.35}$$

Upon performing the Gaussian integrations over the adjoint components of color electric fields the partition function of a 3-dimensional Yang-Mills theory coupled to a massless adjoint Higgs field results up to a prefactor which is irrelevant for the calculation of observables:

$$Z_{cl} = \int [\mathrm{D}A][\mathrm{D}\varphi] \, \exp\left\{ -\beta \int \mathrm{d}^d\boldsymbol{x} \mathrm{Tr}\left[\frac{1}{2}F_{ij}F^{ij} - \frac{1}{4}\mathrm{D}_i\varphi \mathrm{D}^i\varphi \right] \right\}. \tag{7.36}$$

By introducing the momentum space cutoff $k_i < \Lambda_{cl}$ the partition function for the classical lattice model (7.14) is reexpressed as

$$Z_L = \int [\mathrm{D}U][\mathrm{D}\varphi] \, \mathrm{e}^{-\beta H_L}, \tag{7.37}$$

where the lattice Hamiltonian is chosen as [80, 81]:

$$H_L = \sum_x \left[\beta_L \sum_{i<j} \left\{ 1 - \frac{1}{N}\mathrm{Re} \, \mathrm{Tr}U_{ij} \right\} + \frac{\beta_L}{N}\mathrm{Tr}\left\{ \phi(x)\phi(x) - \kappa\sum_i \phi(x)U_i(x)\phi(x+\hat{i})U_i^+(x) \right\} \right]. \tag{7.38}$$

The adjoint Higgs φ is defined at every lattice site and has been rescaled to lattice units $a^2g\varphi \leftrightarrow 2\sqrt{\kappa}\varphi$. The coupling constant between the scalar and gauge field is $\kappa = 1/3$. To generate gauge field configurations according to this partition function the heatbath algorithm and overrelaxation techniques described in chapter 6 for pure lattice Yang-Mills theory must be adapted to this model. Note that the adjoint Higgs is merely an auxiliary field to generate an ensemble of gauge field configurations according to the partition function (7.37). The electrical fields, required for the real-time evolution of the lattice system, are drawn from a Gaussian distribution and projected onto the hypersurface of field configurations satisfying the Gauss constraint in a subsequent step [82]. The algorithm is designed to make the extensive and time-consuming thermalization procedures previously required in classical lattice simulations redundant. Note that the duality of the classical statistical theory to a Yang-Mills theory with an adjoint Higgs is not exact on the

lattice. Conventional thermalization techniques [82] can be used in a final phase of the thermalization to approach the equilibrium distribution to arbitrary precision. The heatbath algorithm for d-dimensional SU(N)-Yang-Mills theory with an adjoint massless Higgs is implemented as follows:

1. *Scalar Update*

   The heatbath update for the scalar field is introduced by noting that the adjoint components of the shifted scalar field

   $$\varphi'(x) = \varphi(x) - \frac{\kappa}{2} \sum_\varphi U_i(x)\varphi(x+\hat{i})U_i^+(x) \tag{7.39}$$

   are Gaussian. The distribution for the scalar field can thus be generated exactly by drawing the adjoint components of φ' from a Gaussian of standard deviation $\sigma = \sqrt{N/\beta_L}$ and performing the shift to the original field φ. An even-odd preconditioning is necessary for parallel implementation.

2. *Gauge Update*

   To account for the coupling term between the gauge and Higgs field an additional accept/reject step is introduced. Gauge links suggested by an update of all SU(2) subgroups with the Cabbibo-Marinari heatbath described in chapter 6 are now accepted with probability:

   $$P_A(U_i'(x) \leftarrow U_i(x)) = min\left(1, \frac{w(U_i'(x))}{w(U_i(x))}\right) \tag{7.40}$$

   where

   $$w(U_i(x)) = \exp\left\{\frac{\kappa\beta_L}{NT}\mathrm{Tr}\left[\phi(x)U_i(x)\phi(x+\hat{i})U_i^+(x)\right]\right\}. \tag{7.41}$$

The interaction term between the scalar and gauge field can also be accounted for in the overrelaxation of gauge fields by supplementing the Metropolis accept/reject step after each overrelaxation trial. As aluded to previously the function of this algorithm is merely to generate a properly distributed ensemble of gauge field configuration $\{U_i(x)\}$. The electrical fields are generated for each ensemble configuration by drawing their adjoint components from a Gaussian of standard deviation $\sigma = \sqrt{2N/\beta_L}$. To take into account Gauss law (7.17) the electrical fields are projected onto the hypersurface of field configurations satisfying this constraint by repeated use of the projection step

$$E_i(x) \rightarrow E_i(x) + \gamma(U_i(x)C(x+\hat{i})U_i^+(x) - C(x)) \tag{7.42}$$

where $C(x)$ is the violation of Gauss's law and the parameter $\gamma < 1/6$ is typically chosen as $\gamma = 0.12$. Note that the electrical fields remain Gauss distributed according to (7.14) during the projection procedure. Typically several hundred subsequent iterations of this projection step are required to reduce the violation of the Gauss constraint to a negligable order of magnitude. Techniques for the generation of an ensemble of field configurations according to the partition function (7.14) found in the literature [82] rely on repeatedly drawing electrical fields from a Gaussian distribution, projecting on the Gauss hypersurface and distributing the injected energy to the gauge fields using the equations of motion. The overall time required for generating initial field configurations typically exceeds the actual measurement time and is virtually eliminated by the procedure described in this section. *A significant performance gain has been achieved in comparison with previous techniques.*

7.7   Integration of the Equations of Motion

Before discussing the numerical integration of the equations of motion of the lattice system a general classical system is considered characterized by a set of coordinates $\{\phi_i\}, i \in \{1, \ldots, n\}$ and conjugate momenta $\{\pi_i\}$. The associated phase space is denoted as $\Lambda = \{\phi_i, \pi_i\}$. The classical equations of motions (shown in a Hamiltonian form with $H : \Lambda \to \mathbb{R}$)

$$\dot{\pi}_i = -\frac{\partial H}{\partial \phi_i} \quad \text{and} \quad \dot{\phi}_i = \frac{\partial H}{\partial \pi_i} \tag{7.43}$$

are a *symplectomorphism* which leaves the phase space product $d\phi_i d\pi_i$ invariant. Any *integrator* $f : \Lambda \to \Lambda$, which is intended to reproduce the classical time evolution of the system over a discrete time interval, is required to satisfy the same constraint. Formally an integrator is called *symplectic*, if it has the structure of a Lie group with the Poisson bracket of transformed coordinates and momenta $\{\phi', \pi'\} = f(\{\phi_i, \pi_i\})$ serving as a Lie bracket:

$$\{\phi', \pi'\} = \sum_i \left[\frac{\partial \phi'}{\partial \phi_i} \frac{\partial \pi'}{\partial \pi_i} - \frac{\partial \phi'}{\partial \pi_i} \frac{\partial \pi'}{\partial \phi_i} \right] = \mathbf{1}. \tag{7.44}$$

Let $\psi = \{\phi_i, \pi_i\} \in \Lambda$ be a phase space state at time $t = 0$ which evolves in time according to

$$\dot{\psi} = \{\psi, H\} = \hat{H}\psi \;\Rightarrow\; \psi(t + \Delta_t) = e^{\Delta_t \hat{H}} \psi(t), \tag{7.45}$$

where the Poisson bracket is defined to act on all components of ψ and $\hat{H}$ is the time evolution operator. If the Hamiltonian can be decomposed into a kinetic and potential term according to $H(\{\phi_i, \pi_i\}) = T(\{\pi_i\}) + V(\{\phi_i\})$, the evolution over the discrete time interval Δ_t takes the form

$$\psi(t + \Delta_t) = e^{\Delta_t(\hat{T} + \hat{V})} \psi(t) = \prod_{i=1}^m e^{a_i \Delta_t \hat{V}} e^{b_i \Delta_t \hat{T}} + \mathcal{O}(\Delta_t^{m+1}) \tag{7.46}$$

where m is called the *order of the integrator* and the coefficients $\{a_i, b_i\}$ are determined from the *Baker-Campbell-Hausdorff formula*. The operators $\hat{T}$, $\hat{V}$ are the time evolution operators for the coordinates $\{\phi_i\}$ and conjugate momenta $\{\pi_i\}$ and are defined by the time derivative of the respective quantity in analogy to (7.45).

For the integration of the Euler-Lagrange equations (7.28,7.29) of the classical lattice system the second order *Verlet integrator*, called *leapfrog*, with coefficients $a_1 = a_2 = 1/2, b_1 = 1$ and $b_2 = 0$ is used. The color electric fields $E_i(x, t)$ are consequently defined at times $(k + 1/2)\Delta_t$ while gauge fields are defined at times $k\Delta_t$ where $k \in \mathbb{N}$. The discretized equations of motion take the following form $[t = k\Delta_t, k \in \mathbb{N}]$:

$$U_i(x, t + \Delta_t) = \exp(i\Delta_t E_i(x, t + \frac{\Delta_t}{2}))U_i(x, t) \tag{7.47}$$

and

$$E_i(x, t + \frac{\Delta_t}{2}) = E_i(x, t - \frac{\Delta_t}{2}) + 2\Delta_t T^a \text{Im Tr} \left\{ T^a \sum_{|j| \neq i} U_{ij}(x, t) \right\}. \tag{7.48}$$

Note that the initial time step in the leapfrog evolution is of length $\Delta_t/2$ with both color electric and gauge fields generated by the algorithm described in the previous section defined at time $t = 0$. Since this time step can not be symmetrized and Δ_t is defined in lattice units, it is the only source of $\mathcal{O}(a)$ errors in the entire simulation.
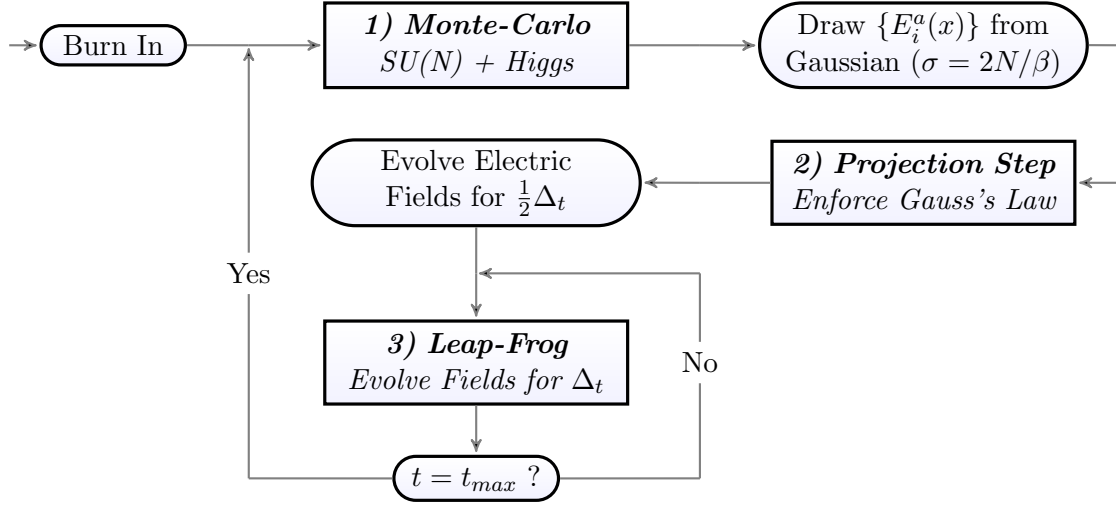
Figure 7.3: Flow chart illustrating the general structure of the classical lattice simulation.

7.8   Summary of the Algorithm

The general structure of the classical lattice simulation is shown in figure 7.3. In the preceeding chapter the following parts of the algorithm required a detailed discussion:

1. *Generation of Gauge Fields*

   An ensemble of link configurations distributed according to (7.14) is generated by coupling the gauge fields to an auxiliary adjoint Higgs field. An overrelaxed Cabbibo-Marinari heatbath supplemented by an accept/reject step to take into account the Higgs field is used for gauge updates. The scalar update relies on an overrelaxed adaption of Bunks algorithm [83].

2. *Projection on Gauss Hypersurface*

   Since field configurations are required to satisfy Gauss's law electrical fields need to be projected on the hypersurface defined by this constraint after being drawn from a Gaussian. A single iteration of the projection algorithm consists in the update

   $$E_i(x) \rightarrow E_i(x) + \gamma(U_i(x)C(x+\hat{i})U_i^+(x) - C(x)), \qquad (7.49)$$

   where $C(x)$ is the violation of Gauss's law and the parameter $\gamma < 1/6$ is chosen as $\gamma \simeq 0.12$.

3. *Classical Time Evolution*

   The Euler-Lagrange equations (7.28,7.29) of the classical lattice system are implemented using a leapfrog scheme which consists of the subsequent update steps

   $$U_i(x, t + \Delta_t) = \exp(\mathrm{i}\Delta_t E_i(x, t + \frac{\Delta_t}{2}))U_i(x, t) \qquad (7.50)$$

   and

   $$E_i(x, t + \frac{\Delta_t}{2}) = E_i(x, t - \frac{\Delta_t}{2}) + 2\Delta_t T^a \mathrm{Im}\ \mathrm{Tr}\left\{ T^a \sum_{|j|\neq i} U_{ij}(x, t) \right\}. \qquad (7.51)$$

8 APPLICATION: DIFFUSION AND DECONFINEMENT

He who seeks for methods without having a definite problem
in mind seeks in the most part in vain.

David Hilbert

In this chapter the classical lattice model will be used to assess the extent of non-perturbative to real-time quantities inaccessible to ordinary lattice simulations. In the first part of this chapter, where many physical and technical aspects of the classical lattice model will be highlighted, the momentum diffusion of heavy quarks is investigated . In the second part of this chapter a measurement of the imaginary part of the real-time static potential, introduced in chapter 4, is presented.

8.1 Momentum Diffusion of Heavy Quarks

One of the simplest quantities to be evaluated in this context is the momentum diffusion coefficient for a heavy non-relativistic quark with mass $M \gg T$. Since the typical quark momentum $p_q \sim \sqrt{MT}$ is much larger than the typical gluon momentum $p_q \sim T$, the diffusion occurs by the accumulation of small kicks and can be described by a Langevin equation of the form:

$$\frac{\mathrm{d}p_i}{\mathrm{d}t} = -\eta_D p_i + \xi_i(t), \quad \langle \xi_i(t)\xi_j(t')\rangle = \kappa \delta_{ij}\delta(t-t'). \tag{8.1}$$

The random force ξ experienced by the quark is gaussian with the diffusion constant κ related to the relaxation rate η_D by a fluctuation dissipation relation:

$$\eta_D = \frac{\kappa}{2MT}. \tag{8.2}$$

It is therefore sufficient to calculate the diffusion constant to parametrize the momentum diffusion of a heavy quark in the quark-gluon plasma. The diffusion constant is defined by the mean squared momentum transfer per unit time. It was shown in [84] that in the limit of infinite quark mass it can be calculated from the correlator of two electric fields separated in time and connected by a straight fundamental Wilson line $W_{0\to t}$:

$$\kappa(\omega) = \frac{g^2}{3N} \int \mathrm{d}t e^{i\omega t} \, Tr\langle W_{0\to t}^+ E_i(t) W_{0\to t} E_i(0)\rangle. \tag{8.3}$$

The diffusion constant $\kappa = \kappa(0)$ is obtained as the electric field correlator integrated against time. Chromo-magnetic forces are neglected due to the vanishing speed of the quark. This coefficient is of a particular interest since a considerable elliptic flow and energy suppression of heavy quarks is observed in heavy ion collisions which indicates a rapid thermalization of c- and b-quarks. The experimental evidence, showing a strong interaction of these high momentum particles with the surrounding medium, is surprising and hard to accommodate with weak-coupling calculations of the diffusion coefficient. It must therefore be expected that the perturbative result discussed in the following will be significantly enhanced by non-perturbative processes. It is straightforward to
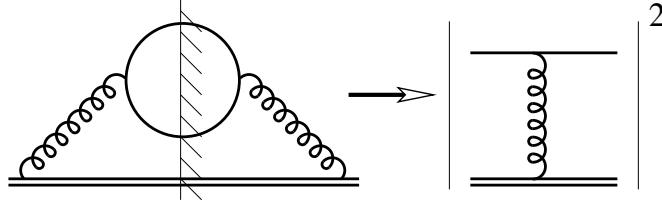
Figure 8.1: The Wightman propagator (left) representing the correlator of A_0 fields along the Wilson line shown as a double line corresponds to the squared matrix element (right) for scattering between a static quark and a gluon or ghost indicated by a solid line.

obtain the diffusion constant $\kappa(\omega = 0)$ to leading order by using the definition $E_i = F_{0i}$ of the chromo-electric field. In a Coulomb or covariant gauge the following expression must be evaluated [85]:

$$\kappa = \frac{C_F g^2}{3} \int \frac{\mathrm{d}^3\boldsymbol{p}}{(2\pi)^3} \, p^2 \tilde{G}_{21}^{00}(\omega = 0, \boldsymbol{p}). \tag{8.4}$$

To remove logarithmically divergent contributions the Wightman propagator is evaluated as the squared matrix element of t-channel scattering process involving the heavy quark (see figure 8.1). Contributions from Compton like processes are ignored in the static limit. The following expression is obtained:

$$\kappa = \frac{8\pi g^4 C_F N}{3} \int_{p \ll T} \frac{\mathrm{d}^3\boldsymbol{p}}{(2\pi)^3} \frac{p^2}{(p^2 + m_D^2)^2} \int \frac{\mathrm{d}^3\boldsymbol{q}}{(2\pi)^3} \delta((p-q)^2 - q^2) q n_B(q)(1 + n_B(q)). \tag{8.5}$$

The heavy quark diffusion constant to leading order is therefore given by:

$$\kappa \simeq \frac{g^2 C_F T m_D^2}{6\pi} \left(\ln \frac{T}{m_D} + \dots \right). \tag{8.6}$$

To match the continuum result to lattice measurements discussed in the next section the HCL-formalism introduced in the previous chapter is used. The lattice regularized result in the limit $\hbar \to 0$ is obtained by replacing the statistical factors $n_B(q)$, $1 + n_B(q)$ with their classical limit T/q and introducing the lattice momenta $\tilde{p}$ defined in (7.31). By approximating the argument of the δ-function via

$$\widetilde{(p-q)}^2 - \tilde{q}^2 = 2\tilde{\boldsymbol{p}} \cdot \mathring{\boldsymbol{q}} + \mathcal{O}(p_i^2) \tag{8.7}$$

the following expression for the heavy quark diffusion constant is obtained in the classical lattice model:

$$\kappa_L \simeq \frac{4\pi g^4 T^2 C_F N}{3} \int \mathrm{d}\boldsymbol{p} \frac{\tilde{p}^2}{(\tilde{p}^2 + m_{D,L}^2)^2} \int \mathrm{d}\boldsymbol{q} \frac{\delta(\tilde{\boldsymbol{p}} \cdot \mathring{\boldsymbol{q}})}{\tilde{q}}. \tag{8.8}$$

The δ-function is removed by viewing the momentum $\boldsymbol{p}$ as a continuum variable $p \sim m_{D,L} \ll 1/a$ and carrying out the angular integration:

$$\kappa_L \simeq \frac{g^4 T^2 C_F N}{3\pi} \int \mathrm{d}\boldsymbol{q} \frac{1}{\sqrt{\tilde{q}^2 \mathring{q}^2}} \left(\ln \frac{1}{a m_{D,L}} + \dots \right) \tag{8.9}$$

The constant obtained by the momentum integral over the Brillouin zone is found to be 1.8313(2) (see [55]).
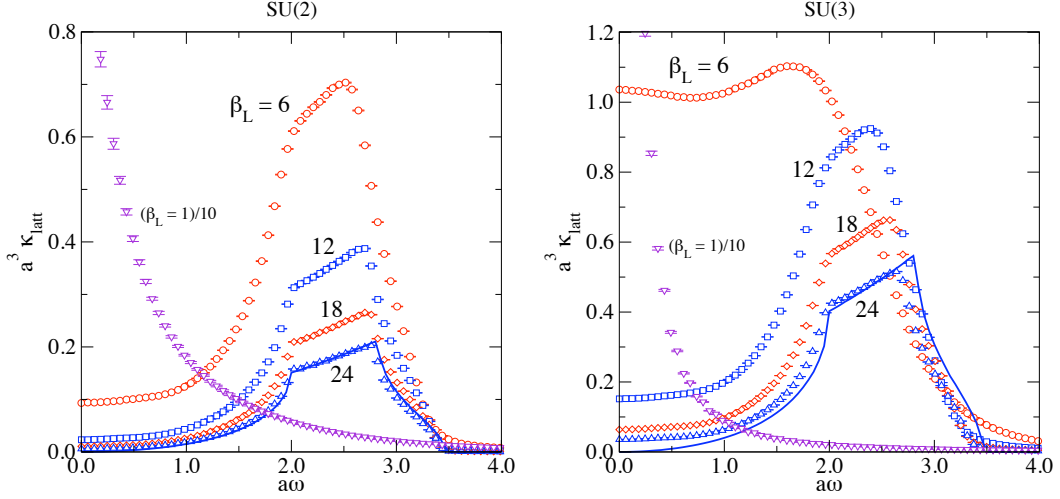
Figure 8.2: Shape of the correlator $\kappa(\omega)$ as obtained in the classical lattice simulations for SU(2) (left) and SU(3) (right). The solid line is the analytical prediction from lattice regularized perturbation theory for $\beta_L = 24$.

8.2 Measurement of the Electric Field Correlator

Due to the temporal gauge the Wilson lines, connecting the electrical fields are fixed to unity in the classical lattice model, and the electric field correlator $\kappa_j(t)$ is defined by the following expression for an arbitrary initial configuration j:

$$a^4\kappa_j(t) = \frac{1}{3N} \; \text{Tr}\langle E_i(t' + t)E_i(t')\rangle. \tag{8.10}$$

Note that the electrical fields on the lattice are related to the electrical fields in the continuum via $E_i \rightarrow a^2 g E_i$. The measurement for a given initial configuration j is performed by storing the electric field at a set of starting times $\{t'_k\}$ and measuring the correlator (8.10) in each subsequent time step of length $a\Delta_t$. To make optimal use of each initial configuration, the correlator is averaged over all starting times $\{t'_k\}$. To obtain the spectrum of the correlator a subsequent Discrete Fourier Transform (DFT) of the correlator is performed

$$\kappa_j(\omega) = a\Delta_t \sum_{t=-Nt}^{N_t} e^{i\Delta_t\omega t} \; \kappa_j(t) \tag{8.11}$$

where N_t is the number of time-steps for the measurement and the frequency $\omega \rightarrow a\omega$ is given in lattice units. The time dependence of $\kappa(t)$ for $t < 0$ is obtained by mirroring the correlator to negative times using the symmetry of (8.10) with respect to time reversal. The diffusion constant is finally obtained by averaging over all N_{conf} ensemble configurations

$$\kappa(\omega) = \frac{1}{N_{conf}} \sum_j \kappa_j(\omega), \tag{8.12}$$

and reading of the static limit $\kappa(\omega = 0)$. The Jacknife error (6.38) of $\kappa(\omega)$ is obtained in the usual fashion by omitting subsets of configurations forming the statistical ensemble. The time step
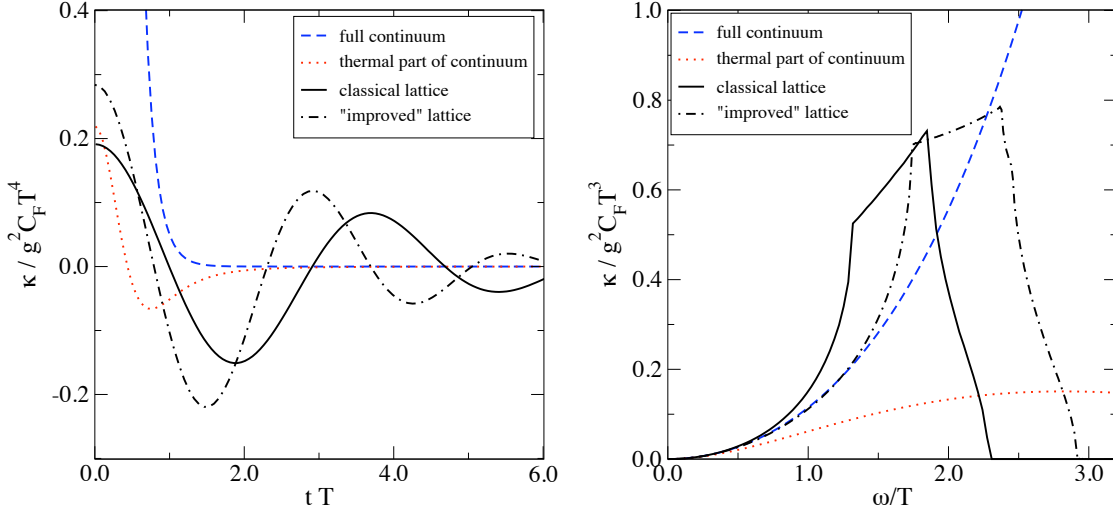
Figure 8.3: The correlator $\kappa(t)$ (left) at leading order and its Fourier transform $\kappa(\omega)$ (right) in the continuum and on the lattice with ordinary and improved [86] action.

was chosen as $\Delta_t = 0.05$ to minimize discretization effects. The lattice volume V and number of ensemble configurations N_{conf} for each measurement at a fixed β were chosen as $V > (20a)^3$ and $N_{conf} \simeq 200$. The spectrum of the correlator as obtained from the classical lattice simulation is shown in figure 8.2 for different values of β_L. A solid line in figure 8.2 shows the tree level spectrum of the correlator in HCL perturbation theory for $\beta_L = 24$. The prediction is obtained by taking the classical limit of the tree level correlator in the continuum

$$\kappa(\omega) = \frac{2\pi g^2 C_F T}{3} \int \frac{d^3 p}{(2\pi)^3} \left[\delta(p - \omega) + \delta(p + \omega)\right] \tag{8.13}$$

and replacing the momenta p by their lattice counterparts $\tilde{p}$ with the momentum integration restricted to the Brillouin zone as usual. The lattice regularized result in the classical limit therefore takes the form:

$$\kappa_L(\omega) = \frac{2\pi g^2 C_F T}{3} \int d\boldsymbol{p} \left[\delta(\tilde{p} - \omega) + \delta(\tilde{p} + \omega)\right] \tag{8.14}$$

As illustrated in figure 8.3 the cusps appearing in the lattice spectra towards large ω are *van Hove singularities* arising from the modified dispersion relation

$$\omega^2(p) = \tilde{p}^2 \tag{8.15}$$

which has vanishing slopes at the edges of the Brillouin zone $\boldsymbol{p} = (n_1, n_2, n_3)\pi/a$ where $n_i = \pm 1$. The cusps in the correlator are therefore discretization artifacts which have little impact on the behavior of the correlator at small ω, where the diffusion constant is defined. Here the lattice regularized spectrum is identical to the continuum expression. The flatness of the spectrum around the origin, where the heavy quark diffusion constant is defined, indicates that this quantity can, in principle, be reliable measured in an ordinary lattice simulation. It is therefore a realistic prospect to analyze the puzzle of the rapid thermalization of heavy quarks in a quark-gluon plasma in the context of the full quantum theory [87].
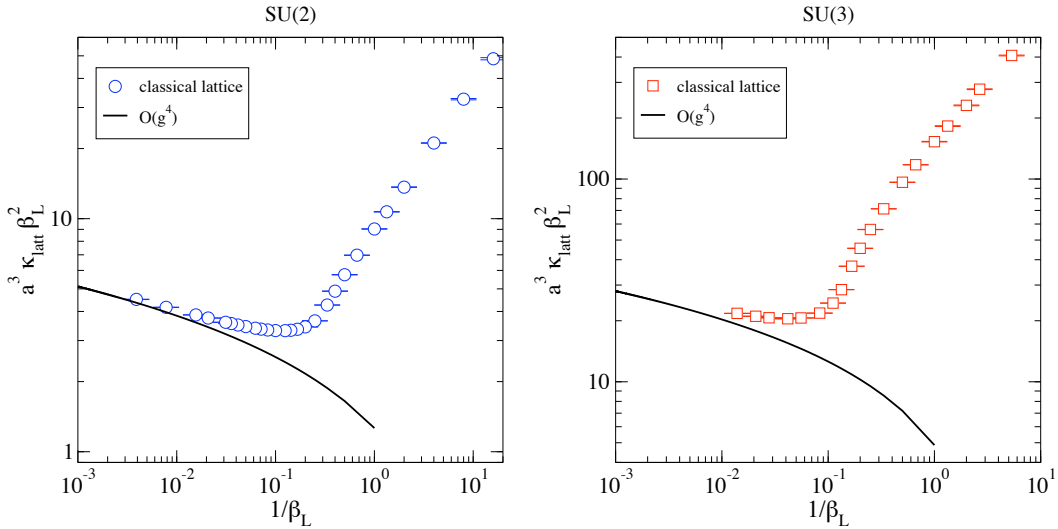
Figure 8.4: The heavy-quark diffusion constant κ_L plotted against the inverse lattice coupling β_L for SU(2) (left) and SU(3) (right).

8.3   Physical Result

The heavy quark diffusion constant as obtained from the classical lattice simulations for SU(2) and SU(3) is compared to the perturbative prediction (8.14) obtained in the HCL framework in figure 8.4. While the lattice results are in perfect agreement with the perturbative prediction towards vanishing lattice coupling, the slope with which the diffusion constant decreases towards higher lattice coupling is smaller than predicted in perturbation theory. A significant difference is observed at intermediate couplings, where the classical theory is still expected to capture the non-perturbative behavior of soft gauge fields correctly. It is important to point out that in this parametrical regime the plaquette expectation value

$$\langle P \rangle = \langle 1 - \frac{1}{N} \text{Tr} \sum_{i<j} U_{ij} \rangle \tag{8.16}$$

which is proportional to the magnetic energy density changes significantly. Since the physics at the magnetic scale is non-perturbative, it is not surprising to see a difference between the weak-coupling prediction and the classical result arising towards the phase transition. The result therefore seems to indicate a significant enhancement of the diffusion of heavy color charges in the Yang-Mills plasma due to non-perturbative physics. A drastic change in the β_L-dependence of the correlator is observed upon entering the strong coupling regime at $\beta_L \approx \frac{1}{2N}$, with the diffusion constant κ becoming proportional to $\beta_L^{-5/2}$. The behavior of κ in this regime is expected to be shaped by discretization effects as will be shown in detail in the following section. As discussed in [87] the vanishing slope of the correlator $\kappa(\omega)$ for small ω indicates that it is possible to obtain a reliable estimate for the diffusion constant in ordinary lattice simulations from an analogous correlator in euclidean space. The expected shape of the correlator is confirmed in the classical lattice simulations, indicating the possibility of solving the puzzle of the rapid thermalization of $c-$ and $b-$ quarks in the quark-gluon plasma in the context of full QCD.
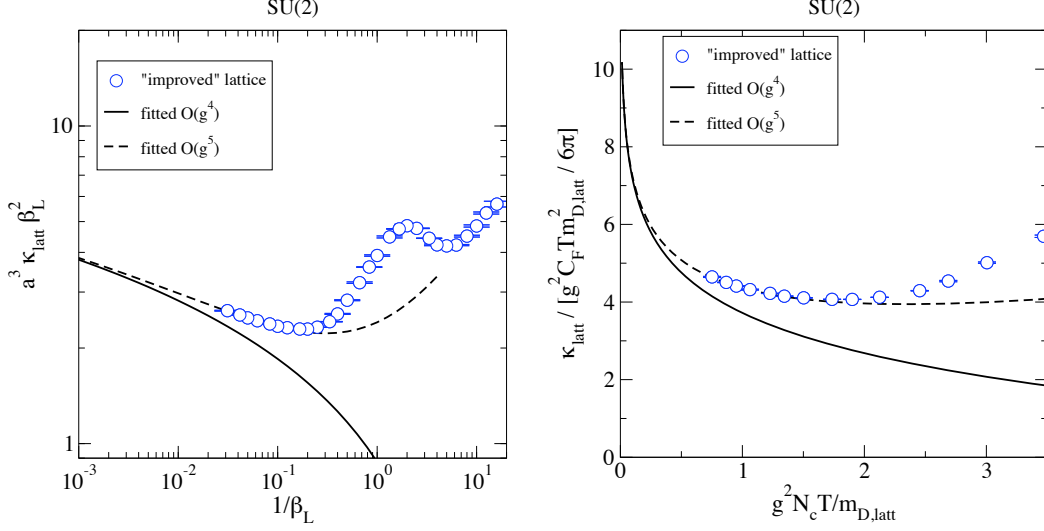
Figure 8.5: The heavy-quark diffusion constant κ_L obtained from a classical lattice with improved action plotted against β_L and $g^2 NT/m_{D,L}$ for SU(2).

8.4   Lessons for the Strong Coupling Regime

In the strong coupling regime $\beta_L^{-1} \to \infty$ the diffusion constant diverges as $\beta_L^{-5/2}$ as shown in figure 8.5. Since the lattice coupling is $\beta_L^{-1} = a(g^2 T/2N)$ it is natural to expect discretization effects to dominate in this regime and to assume that the behavior of the correlator can not be related to Yang-Mills theory in the continuum. This point is illustrated by a measurement of the correlator with an alternative lattice action [86, 55]. While the behavior of both discretizations agrees in the weak coupling regime, the results in the strong coupling are incompatible even on a qualitative level. To understand the behavior of the correlator for the standard action in this regime, it is instructive to look at the classical equations of motion

$$\dot{U}_i(x,t) = \mathrm{i}E_i(x,t)U_i(x,t), \qquad \dot{E}_i^a(x,t) = 2\sum_{|j|\neq i} \mathrm{Im}\,\mathrm{Tr}\left\{T^a U_{ij}(x,t)\right\}. \tag{8.17}$$

Spatial links are compact and the time derivative of E_i in the second equation is therefore bounded. In the strong coupling regime $\beta_L^{-1} \to \infty$ the link matrices become random elements of $SU(N)$ and the mean squared value of the electrical field increases $\langle|E_i^a|^2\rangle$ linearly with β_L^{-1}. The electrical field therefore evolves by Langevin dynamics with the random force appearing as the products of four randomly rotating links forming the associated plaquettes. The time scale for a link to rotate by an $\mathscr{O}(1)$ angle is $t/a \sim 1/|E_i^a| \sim \beta_L^{-1/2}$. A random variable E_i^a with $\langle|E_i^a|^2\rangle \sim \beta_L^{-1}$ experiencing a random force of magnitude ~ 1 with coherence time $\sim \beta_L^{1/2}$ behaves as

$$\langle E_i^a(t)E_i^a(0)\rangle = \langle|E_i^a|^2\rangle \exp\left(-t\beta_L^{3/2}\right). \tag{8.18}$$

Performing the time integration the diffusion constant is identified as $\kappa \sim \beta_L^{-5/2}$ for $\beta_L^{-1} \to \infty$. The argument given here is based on the fact that the time derivative of the electrical field is bounded on the lattice which is not the case in the continuum. The result obtained in the strong coupling limit is therefore an artifact of the lattice discretization.
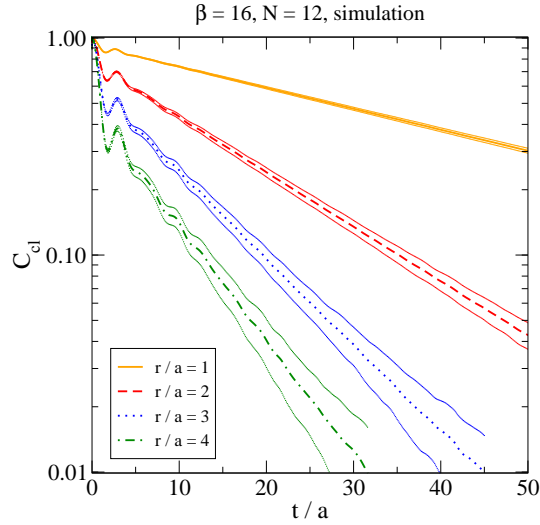
Figure 8.6: A measurement of the absolute value of the Wilson-Loop $C_{cl}(t,r)$ for SU(3) on a small lattice with $V = 12^3$ and lattice coupling $\beta_L = 16$.

8.5   Imaginary Part of the Real-Time Static Potential

In this section I will discuss a measurement of the imaginary part of the real-time static potential introduced in chapter 4. As discussed in that chapter this quantity is associated with the Landau damping phenomenon induced diagrammatically by the symmetric component of the gluon propagator. A measurement of this quantity is therefore of particular interest, since this aspect of thermal physics is captured particularly well by the classical model (see chapter 7). In addition, the imaginary part of the real-time static potential receives no UV-contributions requiring a regularization of the result and can therefore be expected to be insensitive to the nature of the hard scale. The lattice study consists in measuring a rectangular Wilson loop $C_{\mathrm{cl}}(t,r)$ of spatial extent $r = |\mathbf{r}|$ and temporal extent t

$$C_{\mathrm{cl}}(t,r) = \frac{1}{N}\mathrm{Tr}\langle W_{t',r'\to r'+r}W^+_{t'+t,r'\to r'+r}\rangle \tag{8.19}$$

in the classical simulations. Note that temporal Wilson lines are fixed to unity due to the temporal gauge. The fall-off of the correlator, which becomes exponential at large times as illustrated in figure 8.6, is parametrized by the real-time potential

$$V_{\mathrm{cl}}(t,r) = \frac{\mathrm{i}\partial_t C_{\mathrm{cl}}(t,r)}{C_{\mathrm{cl}}(t,r)}. \tag{8.20}$$

To match the numerical results from the classical lattice model to the lattice regularized quantum theory the time-dependence of the Wilson-Loop (8.19) was calculated in HCL-perturbation theory. The calculation is technically difficult and was performed in [29]. The leading order time dependence of the potential in the continuum serves as a starting point for the calculation:

$$V(t,r) = -\frac{g^2 C_F \hbar}{4\pi}\left[m_D + \frac{\mathrm{e}^{-m_D r}}{r}\right] + \delta V(t,r) \tag{8.21}$$

Figure 8.7: Integration contour for the classical real-time static potential.

The Debye-screened part of the potential has been separated off with the remainder of the potential taking the form:

$$
\begin{aligned}
\delta V(t,r) \;=\; & g^2 C_F \hbar \int \frac{\mathrm{d}^3 \boldsymbol{p}}{(2\pi)^3} (1 - \cos p_3 r) \int_{-\infty}^{\infty} \frac{\mathrm{d}p^0}{\pi} p^0 \left[\mathrm{e}^{-\mathrm{i}|p^0|t} + n_B(|p^0|) \left(\mathrm{e}^{-\mathrm{i}|p^0|t} - \mathrm{e}^{\mathrm{i}|p^0|t} \right) \right] \times \\
& \times \; \left[\left(\frac{1}{\boldsymbol{p}^2} - \frac{1}{(p^0)^2} \right) \rho_L(p^0, \boldsymbol{p}) + \left(\frac{1}{p_3^2} - \frac{1}{\boldsymbol{p}^2} \right) \rho_T(p^0, \boldsymbol{p}) \right].
\end{aligned}
\tag{8.22}
$$

The expression was obtained in a euclidean setup in [28] and analytically continued to Minkowski space with ρ_L and ρ_T being the spectral functions of the longitudinal and transverse components of the resummed gluon propagator $\tilde{G}_R$. In the HCL formalism the result takes the form

$$
\begin{aligned}
V_{cl}(t,r) \;=\; & g^2 C_F T \lim_{\hbar \to 0} \int d\boldsymbol{p} (1 - \cos p_3 r) \int_{-\infty}^{\infty} \frac{\mathrm{d}p^0}{\pi} \left(\mathrm{e}^{-\mathrm{i}p^0 t} - \mathrm{e}^{\mathrm{i}p^0 t} \right) \times \\
& \times \; \left[\left(\frac{1}{\tilde{\boldsymbol{p}}^2} - \frac{1}{(p^0)^2} \right) \rho_L(p^0, \tilde{\boldsymbol{p}}) + \left(\frac{1}{\tilde{p}_3^2} - \frac{1}{\boldsymbol{p}^2} \right) \rho_T(p^0, \tilde{\boldsymbol{p}}) \right],
\end{aligned}
\tag{8.23}
$$

where the spectral functions are defined in the usual manner from the longitudinal and transverse components $\Delta_{L,T}$ of the retarded HCL gluon propagator:

$$
\rho_{L,T}(p^0, \boldsymbol{p}) = \frac{1}{2\mathrm{i}} \left[\Delta_{L,T}(p^0 + \mathrm{i}\epsilon, \tilde{\boldsymbol{p}}) - \Delta_{L,T}(p^0 - \mathrm{i}\epsilon, \tilde{\boldsymbol{p}}) \right].
\tag{8.24}
$$

It is evident that the time independent Debye screened part of the potential due to single gluon exchange vanishes and only the Bose enhanced component of $\delta V(t,r)$ survives the classical limit. This component will dominate in the large time limit and is therefore the defining contribution for the imaginary part of the real-time static potential. The longitudinal and transversal components of the retarded HCL propagator for the gauge field appearing in (8.24) have the general structure

$$
\Delta_{L,T}(p^0, \tilde{\boldsymbol{p}}) = \frac{1}{\tilde{p}^2 - (p^0)^2 + \Pi_{L,T}(p^0, \tilde{\boldsymbol{p}})}
\tag{8.25}
$$

with the retarded HCL self energies obtained as [29]:

$$
\begin{aligned}
\Pi_L(p^0, \tilde{\boldsymbol{p}}) \;=\; & 2g^2 T C_A \left(1 - \frac{(p^0)^2}{\tilde{\boldsymbol{p}}^2} \right) \left(\frac{\Sigma}{4\pi a} - \int d\boldsymbol{q} \frac{1}{\tilde{\boldsymbol{q}}^2} \frac{p^0}{p^0 - \tilde{\boldsymbol{p}} \cdot \boldsymbol{v}} \right) \\
\Pi_T(p^0, \tilde{\boldsymbol{p}}) \;=\; & g^2 T C_A \left[\frac{(p^0)^2}{\tilde{\boldsymbol{p}}^2} \left(\frac{\Sigma}{4\pi a} - \int d\boldsymbol{q} \frac{1}{\tilde{\boldsymbol{q}}^2} \frac{p^0}{p^0 - \tilde{\boldsymbol{p}} \cdot \boldsymbol{v}} \right) + \int d\boldsymbol{q} \frac{\mathring{\boldsymbol{q}}^2}{(\tilde{\boldsymbol{q}}^2)^2} \frac{p^0}{p^0 - \boldsymbol{p} \cdot \boldsymbol{v}} \right].
\end{aligned}
\tag{8.26}
$$

C_A denotes the adjoint Casimir and the quantity $\boldsymbol{v}$ is defined as $v_i = \mathring{q}_i / \sqrt{\tilde{\boldsymbol{q}}^2}$. The constant $\Sigma/4\pi a = \int d\boldsymbol{q} \tilde{\boldsymbol{q}}^{-2}$ is evaluated as $\Sigma \simeq 3.175911535625$. To isolate the imaginary part of (8.23) the p^0-integration is viewed as an integration contour in the complex plane and deformed suitably. Since ρ_L is linear in p^0 around the origin, the pole in the preceeding expression is cancelled and the
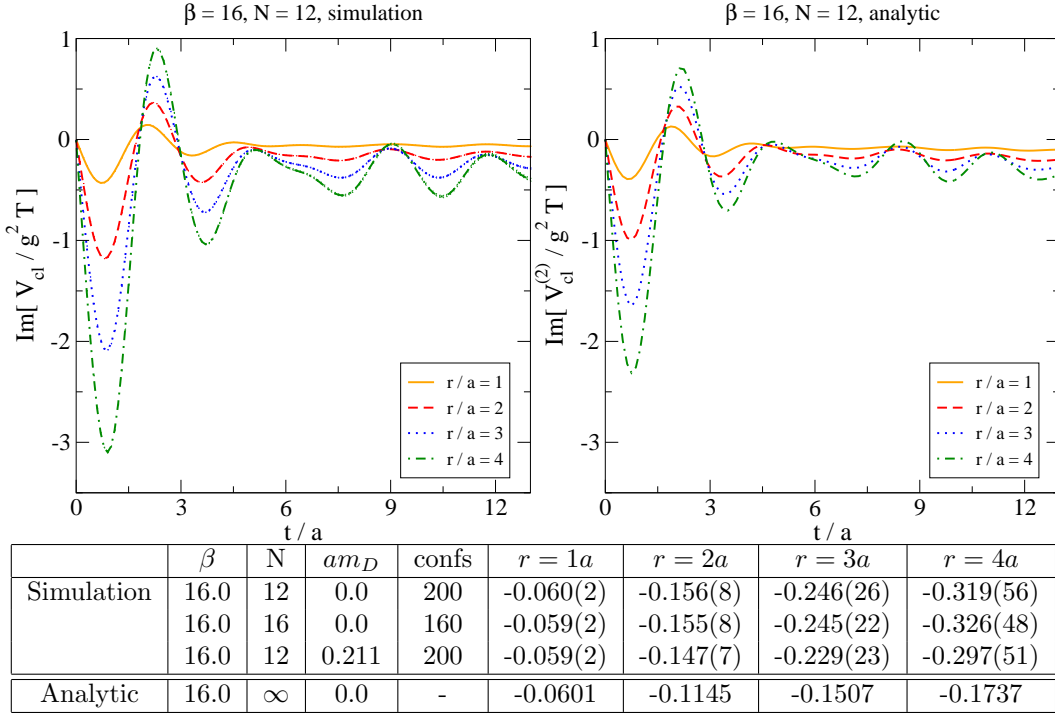
	β	N	am_D	confs	$r = 1a$	$r = 2a$	$r = 3a$	$r = 4a$
Simulation	16.0	12	0.0	200	-0.060(2)	-0.156(8)	-0.246(26)	-0.319(56)
	16.0	16	0.0	160	-0.059(2)	-0.155(8)	-0.245(22)	-0.326(48)
	16.0	12	0.211	200	-0.059(2)	-0.147(7)	-0.229(23)	-0.297(51)
Analytic	16.0	∞	0.0	-	-0.0601	-0.1145	-0.1507	-0.1737

Figure 8.8: Time-dependence of the imaginary part of $V(t, \mathbf{r})$ as obtained from lattice-regularized perturbation theory and classical simulations. Below is an overview of the results in the large-time limit for $\beta = 16$. Results from classical and full HTL-improved simulations ($am_D > 0$) agree within error bars.

expression is finite at $p^0 = 0$. From (8.24) the integration contour on the left of figure is identified and deformed as indicated. There are no poles outside of the real axis and ϵ may therefore be chosen arbitrarily large without altering the result. As a consequence all terms multiplied by $\exp(\pm i(p^0 \pm i\epsilon)t)$ must vanish at for $t > 0$. The imaginary part is finally obtained as:

$$
\mathrm{Im}\left[\frac{V_{cl}(t, r)}{g^2 T}\right] = 2C_F \int d\boldsymbol{p}(1 - \cos p^3 r)\left\{t\Delta_L(0, \tilde{\boldsymbol{p}}) - \int_{-\infty}^{\infty} \frac{dp^0}{2\pi} e^{-i(p^0 + i\epsilon)t} \times \right.
$$
$$
\times \left. \left[\left(\frac{1}{\tilde{\boldsymbol{p}}^2} - \frac{1}{(p^0 + i\epsilon)^2}\right)\Delta_L(p^0 + i\epsilon, \tilde{\boldsymbol{p}}) + \left(\frac{1}{\tilde{p_3}^2} - \frac{1}{\tilde{\boldsymbol{p}}^2}\right)\Delta_L(p^0 + i\epsilon, \tilde{\boldsymbol{p}})\right]\right\} \quad (8.27)
$$

The time dependence of the imaginary part of the potential measured in the classical lattice simulations is compared to the lattice-regularised perturbative result in figure 8.8. All simulations were performed with a time step of $\Delta = 0.02a$ and ensemble-sizes > 100. Non-perturbative corrections were found to amplify the imaginary part of the real-time static potential, which is extracted according to (8.20) in the large time limit, by up to 100%, widening the quarkonium peak in figure 4.1 but leaving the qualitative structure unchanged. To assess the extent to which this quantity receives corrections from physics at the hard scale so-called hard-thermal loop improved simulations were performed which are described in detail in the next section. The modifications were found to be small for reasonable values of the Debye mass am_D in lattice units.

KINETIC THEORY

9 KINETIC THEORY

*Understanding is, after all, what science is all about - and
science is a great deal more than mindless computation.*

Roger Penrose

In this chapter the inclusion of leading order quantum effects in a classical framework is discussed. The Yang-Mills Vlasov equations serve as a starting point and are subsequently transformed into a form suitable for implementation in a semi-classical lattice model. The equations of motion on the lattice are derived for a general (non-)equilibrium system and an algorithm for the generation of an ensemble of initial configurations in thermal equilibrium is discussed. The algorithm relies on the Monte-Carlo techniques previously introduced for the classical lattice model and virtually eliminates spurious thermalization times required by conventional techniques. The chapter is concluded by a schematic description of the simulation of kinetic theory in thermal equilibrium.

9.1 Yang-Mills Vlasov Equations

Leading order hard-mode contributions can be taken into account in the context of an effective classical theory by integrating out the hard scale, i.e momenta of order T, and subsequently taking the classical limit. The hard scale is parametrized by an effective hard mode distribution $f^a(\mathbf{x}, \mathbf{p})$ which influences soft classical fields by the associated color current. The time evolution of $f^a(\mathbf{x}, \mathbf{p})$ is found to be governed by a Boltzmann type equation and the effective theory can thus be interpreted as describing a distribution of hard particles moving in the background of soft classical fields. The non-abelian Yang-Mills Vlasov equations of the effective theory are given by the set of relations [88, 89, 90]

$$(\mathrm{D}_\mu F^{\mu\nu})^a = (j^\nu)^a = g \int \frac{\mathrm{d}^3 \boldsymbol{p}}{(2\pi)^3} v^\nu f^a \tag{9.1}$$

$$(v^\mu \mathrm{D}_\mu f)^a + g v^\mu F^a_{\mu i} \frac{\partial \bar{f}}{\partial p^i} = 0, \tag{9.2}$$

where the first equation is the classical Yang-Mills field equation. The second equation describes the time evolution of the adjoint component of the momentum distribution of hard gluonic modes

$$\mathbf{f}(\mathbf{x}, \mathbf{p}) = \bar{f}(\mathbf{p})\mathbf{1} + f^a(\mathbf{x}, \mathbf{p})T^a + ... \tag{9.3}$$

which have been ignored in the purely classical model introduced in chapter 7. The singlet component $\bar{f}$ of the hard mode distribution does not interact directly with soft fields and is expected to evolve on much longer time and length scales than the adjoint component. It is therefore introduced as a homogeneous and time independent background distribution. The ultra-relativistic nature of the plasma is accounted for by restricting hard mode momenta $v_p = (1, \mathbf{p}/p)$ to the light-cone. By integrating over the absolute momentum $p = |\mathbf{p}|$ in the second equation and defining the angular distribution function

$$W^a(\mathbf{x}, \mathbf{v}) = 4\pi g \int_0^\infty \frac{\mathrm{d}p p^2}{(2\pi)^3} f^a(\mathbf{x}, \mathbf{p}) \tag{9.4}$$

the Yang-Mills Vlasov equations take a more convenient form. Choosing a temporal gauge the following set of equations is obtained which has been substituted by the equation of motion for the magnetic field following from the relation $\dot{A}_i = E_i$,

$$
\begin{aligned}
\dot{\boldsymbol{B}} &= -\mathbf{D} \times \boldsymbol{E}, \\
\dot{\boldsymbol{E}} &= \mathbf{D} \times \boldsymbol{B} - \boldsymbol{j}, \\
\mathbf{D} \cdot \boldsymbol{E} &= -j^0
\end{aligned}
\tag{9.5}
$$

and

$$
\dot{W} = -(\boldsymbol{v} \cdot \boldsymbol{D})W - m^2(\boldsymbol{E} + (\boldsymbol{v} \times \boldsymbol{B})) \cdot \boldsymbol{U}(v),
\tag{9.6}
$$

where the hard mode current j is defined as:

$$
j^\mu = \int \frac{\mathrm{d}\Omega_v}{4\pi} v^\mu W.
\tag{9.7}
$$

The first two relations are just the Yang-Mills field equations with an additional change in the electric field induced by a possible anisotropy of hard-modes along the direction i. Gauss's law (9.5) introduces the overall adjoint charge of hard modes at each point as a source for the chromo-magnetic field. The Vlasov equation (9.6) finally describes the motion of hard modes in the background of soft electric and magnetic fields. The quantity $m^2 U^i(\mathbf{v})$ is defined by the following integral:

$$
m^2 U^i(\mathbf{v}) = -4\pi g^2 \int_0^\infty \frac{\mathrm{d}p p^2}{(2\pi)^3} \frac{\partial \bar{f}(p\mathbf{v})}{\partial p^i}
\tag{9.8}
$$

The effective mass m^2, which has been introduced in the previous equation, corresponds to the classical Debye mass in thermal equilibrium. It is defined by the relation:

$$
m^2 = \int \mathrm{d}\Omega_v M \quad \text{where} \quad M = 4\pi g^2 \int_0^\infty \frac{\mathrm{d}p p^2}{(2\pi)^3} \frac{\bar{f}(p\mathbf{v})}{p}|_{v=1}.
\tag{9.9}
$$

Note that classical Yang-Mills theory suffers from a Rayleigh-Jeans type divergence of the energy density analogous to the divergence encountered in statistical electrodynamics. It has therefore not been attempted to define any continuum limit in the classical lattice model introduced in chapter 7. This problem is remedied by the inclusion of leading order quantum effects. The set of kinetic equations introduced in this section is free of ultraviolet divergences facilitating the definition of a continuum limit in the corresponding lattice model.

9.2   Expansion in Spherical Harmonics

In the following the Yang-Mills Vlasov equations (9.5,9.6) will be transformed into a form suitable for implementation in a semi-classical lattice simulation. The scheme outlined in the following section is motivated by the need to find a suitable discretization for the unit sphere of directions $\boldsymbol{v}$. Several schemes have been put forward to tackle this issue and the approach outlined in the following sections will rely on an expansion of the hard mode distribution W in spherical harmonics. This approach is suitable for the purposes of a numerical implementation since the expansion can be truncated at some finite order. As usual a temporal gauge will be chosen for the numerical

implementation. No restriction will be made on the form of the background distribution $\bar{f}$ or initial conditions for the hard mode distribution W. By expanding the adjoint components of the hard mode distribution in spherical harmonics $W^a(\mathbf{x}, \mathbf{v}) = W^a_{lm}(\mathbf{x}) Y_{lm}(\mathbf{v})$ the equation of motion for the electrical field as well as Gauss's law (9.5) take the form

$$\dot{\boldsymbol{E}} = \mathrm{D} \times \boldsymbol{B} - \frac{W^a_{1m}}{4\pi} \boldsymbol{v}^*_m, \quad \mathrm{D} \cdot \boldsymbol{E} = -\frac{1}{2\sqrt{\pi}} W^a_{00} \tag{9.10}$$

where the following constants have been introduced:

$$\boldsymbol{v}_m = \int \mathrm{d}\Omega Y^*_{lm} \boldsymbol{v} = \begin{pmatrix} -\delta_{m1}\sqrt{\frac{2\pi}{3}} + \delta_{m,-1}\sqrt{\frac{2\pi}{3}} \\ i\delta_{m1}\sqrt{\frac{2\pi}{3}} + i\delta_{m,-1}\sqrt{\frac{2\pi}{3}} \\ \delta_{m0}\sqrt{\frac{4\pi}{3}} \end{pmatrix}. \tag{9.11}$$

It is a more difficult task to derive a similar expansion of the Vlasov equation (9.6). In a first step the coupling of the angular distribution to the singlet component $\bar{f}$ is rewritten in a more convenient form. Using the operator identity

$$\nabla_p \bar{f} = \frac{1}{p} \nabla_v \bar{f} + \mathbf{v} \frac{\partial \bar{f}}{\partial p} \tag{9.12}$$

the quantity $m^2 \mathbf{U}(\mathbf{v})$ is related to the angular mass M by partial integration:

$$m^2 \mathbf{U}(\mathbf{v}) = -(\nabla_v - 2\mathbf{v}) M \tag{9.13}$$

The Vlasov equation can now be rewritten to take the following form:

$$\partial_t W^a = -v^i (\mathrm{D}_i W)^a + (E^a_i + \epsilon_{ijk} v^j B^k)(2\boldsymbol{v} - \nabla_v)^i M, \tag{9.14}$$

where the chromo-electric and -magnetic fields are obtained from the usual relations $E_i = \dot{A}_i$ and $-\epsilon_{ijk} B_k = F_{ij}$ respectively. The hard mode distribution is expanded in spherical harmonics in the next step

$$W^a = W^a_{lm} Y_{lm}, \quad W^a_{l,-m} = (-1)^m W^{a*}_{lm}, \tag{9.15}$$

where the additional restriction on the right follows from the necessity to constrain the distribution function $W^a \in \mathbb{R}$ to the set of real numbers. By performing a subsequent angular integration of the Yang-Mills Vlasov equation against $Y^*_{l'm'}$ a set of coupled Vlasov equations for the individual spherical components W^a_{lm} is obtained:

$$\partial_t W^a_{lm} = -C^i_{lml'm'}(\mathrm{D}_i W_{l'm'})^a + m^2 E^{aE}_i X^i_{lm} + m^2 B^{aB}_i X^i_{lm}. \tag{9.16}$$

The constants $^E X^i_{lm}$ and $^B X^i_{lm}$ parametrizing the influence of chromo-electric and -magnetic fields on the evolution of the hard mode distribution are defined as

$$\begin{aligned} ^E X^i_{lm} &= \int \mathrm{d}\Omega_v Y^*_{lm}(2v^i - \nabla^i_v)\Omega, \\ ^B X^i_{lm} &= \epsilon_{ijk} \int \mathrm{d}\Omega_v Y^*_{lm} v^j \nabla^k_v \Omega, \end{aligned} \tag{9.17}$$

where the antisymmetry of ϵ_{ijk} has been used to obtain the last expression. The distribution Ω is defined as the normalized angular mass:

$$\Omega = \frac{1}{m^2}M. \tag{9.18}$$

The constants $C^i_{lml'm'}$ parametrize the coupling between the Vlasov equations for individual spherical components:

$$C^i_{lml'm'} = \int d\Omega_v Y^*_{lm} v^j Y_{l'm'} \tag{9.19}$$

The constants have been evaluated in [93] and can be expressed in the following form for $l' = l+1$

$$C^i_{lml'm'} = \begin{pmatrix} \frac{1}{\sqrt{2}}\left[\delta_{m',m-1}A(l,-m) - \delta_{m',m+1}A(l,m)\right] \\ \frac{i}{\sqrt{2}}\left[-\delta_{m',m-1}A(l,-m) + \delta_{m',m+1}A(l,m)\right] \\ \delta_{m,m'}B(l,m) \end{pmatrix} \tag{9.20}$$

where the coefficient $A(l,m)$ and $B(l,m)$ are defined via

$$A(l,m) = \sqrt{\frac{(l+2+m)(l+1+m)}{2(2l+1)(2l+3)}} \quad \text{and} \quad B(l,m) = \sqrt{\frac{(l+1-m)(l+1+m)}{2(2l+1)(2l+3)}}. \tag{9.21}$$

For $l' = l-1$ the following form is obtained:

$$C^i_{lml'm'} = \begin{pmatrix} \frac{1}{\sqrt{2}}\left[-\delta_{m',m-1}A(l',m') + \delta_{m',m+1}A(l',-m')\right] \\ \frac{i}{\sqrt{2}}\left[\delta_{m',m-1}A(l',m') - \delta_{m',m+1}A(l',-m')\right] \\ \delta_{m,m'}B(l',-m') \end{pmatrix}. \tag{9.22}$$

If $|l'-l| \neq 1$, the constants vanish. For many practical purposes it will be desirable to obtain the constants ${}^EX^i_{lm}$ and ${}^BX^i_{lm}$ which parametrize the influence of the background distribution Ω form a suitably truncated series of spherical coefficients Ω_{lm}. An expansion in spherical harmonics is greatly facilitated by expressing the gradient appearing in (9.17) using the angular momentum operator $\mathbf{L} = -i\mathbf{v} \times \nabla_v$. By calculating the commutator $[\mathbf{v}, \mathbf{L}^2]$ with the light-cone velocity the following general identity is obtained:

$$[\mathbf{v}, \mathbf{L}^2]|_{v=1} = 2\left(\nabla_{\mathbf{v}} - \mathbf{v}\left[1 + \frac{\partial}{\partial v}\right]\right) \tag{9.23}$$

The commutator acts on Ω in a similar way as the differential operator appearing in (9.17)

$$[\mathbf{v}, \mathbf{L}^2]\Omega = 2\left(\nabla_{\mathbf{v}} - \mathbf{v}\right)\Omega - 2\mathbf{v}\frac{\partial}{\partial v}\Omega = 2(\nabla_{\mathbf{v}} + \mathbf{v})\Omega \quad \Rightarrow \quad \boldsymbol{\nabla}_v\Omega = \frac{1}{2}[\boldsymbol{v}, \boldsymbol{L}^2] - \boldsymbol{v}. \tag{9.24}$$

The identity is again derived by partial integration:

$$\frac{\partial}{\partial v}\Omega = \frac{4\pi g^2}{m^2}\int_0^\infty \frac{dp\, p^2}{(2\pi)^3}\frac{\partial \bar{f}}{\partial p} = -2\Omega \tag{9.25}$$

9.3 Hilbert Space Representation

For practical applications it will be useful to obtain the constants $^{E}X^{i}_{lm}$ and $^{B}X^{i}_{lm}$ from a spherical representation of the singlet background. To present the corresponding relations in a compact form it is convenient to choose a Hilbert space representation. Let $\mathscr{H}$ be a Hilbert space spanned by a base of orthonormal states $\{|l,m\rangle\}, l \in \mathbb{N}, m \in \{-l, \dots, l\}$. Any function $\phi : \mathscr{H} \to \mathbb{C}$ defined on the 2-sphere is related to a state $|\phi\rangle \in \mathscr{H}$ in an unambiguous and consistent manner by introducing the following dictionary:

$$\phi = \phi_{lm}Y_{lm} \quad \leftrightarrow \quad \hat{\phi}|l,m\rangle = \phi_{lm}|l,m\rangle, \quad \phi^{*} = \phi^{*}_{lm}Y^{*}_{lm} \quad \leftrightarrow \quad \langle l,m|\hat{\phi} = \langle l,m|\phi^{*}_{lm}$$

and

$$\langle a|b\rangle \quad \leftrightarrow \quad \int d\Omega \; a^{*}b. \tag{9.26}$$

The spherical harmonics are thus seen as the basis of a Hilbert space with a vector product defined by a unit sphere integration over the product of the associated functions. Using this dictionary the constants $C^{i}_{lml'm'}$ are translated into the Hilbert space representation

$$C^{i}_{l'm'lm} = \langle l'm'|v^{j}|lm\rangle. \tag{9.27}$$

This relation as well as the following property of the squared angular momentum operator

$$\boldsymbol{L}^{2}|lm\rangle = l(l+1)|lm\rangle \tag{9.28}$$

can be used to obtain a representation of the constants $^{E}X^{i}_{lm}$:

$$
\begin{aligned}
^{E}X^{i}_{lm} &= \sum_{l'm'} \Omega_{l'm'}\langle lm| - \frac{1}{2}[v^{i}, L^{2}] + 3v^{i}|l'm'\rangle \\
&= \sum_{l'm'} \Omega_{l'm'}\left(3 + \frac{l(l+1) - l'(l'+1)}{2}\right) C^{i}_{lml'm'}.
\end{aligned} \tag{9.29}
$$

In a final step the constants $^{B}X^{i}_{lm}$ are related to the set of coefficient $\{\Omega_{lm}\}$ representing the singlet background:

$$^{B}X^{k}_{lm} = -\frac{1}{2}\epsilon_{ijk}\sum_{l'm'}\Omega_{l'm'}\langle lm|v^{i}\boldsymbol{L}^{2}v^{j}|l'm'\rangle. \tag{9.30}$$

The antisymmetry of ϵ_{ijk} has again been used to represent the constants in a compact form. By inserting unity in form of a sum over the set of vectors $\{|lm\rangle\}$, which forms an orthonormal base of the Hilbert space, the constants can be evaluated to take the final form:

$$
\begin{aligned}
^{B}X^{k}_{lm} &= -\frac{1}{2}\sum_{ab}\epsilon_{ijk}\sum_{l'm'}\Omega_{l'm'}\langle lm|v^{i}\boldsymbol{L}^{2}|ab\rangle\langle ab|v^{j}|l'm'\rangle \\
&= -\frac{1}{2}\sum_{abl'm'}\Omega_{l'm'}\epsilon_{ijk}a(a+1)C^{i}_{lmab}C^{j}_{abl'm'}
\end{aligned} \tag{9.31}
$$

9.4   Equations of Motion

The results of the previous sections are summarized below. The complete set of Yang-Mills Vlasov equations in a temporal gauge is shown after rescaling the fields according to $W^a \to m^2 W^a$ and using contravariant indices to facilitate a transition to the lattice:

$$
\begin{aligned}
\partial_t B_i^a &= -\epsilon_{ijk} \mathrm{D}_j E_k^a, \\
\partial_t E_i^a &= \epsilon_{ijk}(\mathrm{D}_j B_k)^a + \frac{m^2}{4\pi}(v_m^i)^* W_{1m}^a, \\
\partial_t W_{lm}^a &= -(\mathrm{D}_i W_{l'm'})^a C_{lml'm'}^i + E_i^{aE} X_{l'm'}^i + B_i^{aB} X_{l'm'}^i, \\
\mathrm{D}_i E_i^a &= \frac{m^2}{2\sqrt{\pi}} W_{00}^a.
\end{aligned}
\tag{9.32}
$$

The time evolution for the magnetic field is obtained from the definition $E_i = \dot{A}_i$. The background distribution Ω_{lm} enters the kinetic equations via the constants $^E X, ^B X$ which are listed here again for convenience:

$$
\begin{aligned}
^E X_{l'm}^i &= \int \mathrm{d}\Omega_v Y_{lm}^*(2v^i - \nabla_v^i)\Omega = \sum_{l'm'} \Omega_{l'm'}\left(3 + \frac{l(l+1) - l'(l'+1)}{2}\right) C_{lml'm'}^i, \\
^B X_{lm}^i &= \epsilon_{ijk} \int \mathrm{d}\Omega_v Y_{lm}^* v^j \nabla_v^k \Omega = -\frac{1}{2} \sum_{abl'm'} \Omega_{l'm'} \epsilon_{ijk} a(a+1) C_{lmab}^j C_{abl'm'}^k.
\end{aligned}
\tag{9.33}
$$

To gain an intuitive understanding of these equations, the reader should be aware that the first two equations are just the ordinary Yang-Mills field equations with an additional change in the electrical field E_i induced by the anisotropy of the hard mode distribution in the direction i. The additional term corresponds to the hard mode distribution integrated against the unit vector $\boldsymbol{v}$. Gauss's law in the last equation constrains the change in the electrical flux through an arbitrary volume element to be equal to the overall adjoint charge of hard modes contained in this volume element. It is no more difficult to gain an understanding of the Vlasov equation in the third line which has been rewritten as an infinite set of inter-dependent equations for the spherical components W_{lm} of the angular distribution of hard gluonic modes. Individual equations are directly coupled via the gradient of the distribution. The effect of soft chromo-electric and magnetic fields on the evolution of the momentum distribution is introduced by two additional terms relating the change in the momentum distribution directly to the force exerted by the respective fields. In an isotropic medium where $\Omega_{lm} = \delta_{l0}\delta_{m0}$ the constants $^B X_{lm}^i$ vanish and the momentum distribution W is only affected by electrical fields. The kinetic equations in the special case of thermal equilibrium are obtained by setting the effective mass m equal to the Debye mass m_D and choosing an isotropic momentum distribution $\Omega_{lm} = \delta_{l0}\delta_{m0}$. As a consequence of isotropy the constants $^B X_{lm}^i$ are set to zero and the constants coupling the momentum distribution to the electrical field are reduced to the form $^E X_{lm}^i = \delta_{l1} v_m^i$. The Vlasov equation in thermal equilibrium is therefore significantly simplified:

$$
\partial_t W_{l'm'}^a = -(\mathrm{D}_i W_{lm})^a C_{l'm'lm}^i + \delta_{l1} v_m^i E_i^a.
\tag{9.34}
$$

Note that this form also applies for a general isotropic medium, where only the effective mass m in the second equation of (9.32) needs to be reevaluated.
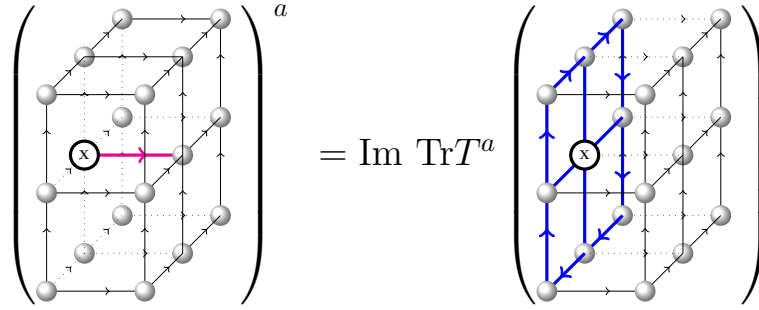
Figure 9.1: Lattice representation of the chromo magnetic field $B_i(x)$ (highlighted in magenta). The field is obtained as a sum of all plaquettes (blue) transverse to the orientation of the magnetic field and including the site x as indicated in the illustration.

9.5   Kinetic Theory on the Lattice

To solve the previously introduced set of equations use will be made of the discretization of the classical Yang-Mills field equations introduced in the two preceding chapters. The additional fields W_{lm}^a representing the hard mode distributions are independent of any direction and will therefore be placed at lattice sites. It is convenient to rescale the fields according to $W \leftrightarrow agW$. By coupling the classical equation of motion for the electrical field on the lattice to the discretized hard mode current j the following relation ensues in correspondence to (9.32)

$$\dot{E}_i(x) = 2T^a \text{Im Tr} \left(T^a \sum_{|j| \neq i} U_{ij}(x) \right) + \frac{1}{2}\big(j_i(x) + U_i(x)j_i(x + \hat{i})U_i^+(x)\big). \qquad (9.35)$$

Note that the expression has been symmetrized by averaging the current over the beginning and end of the link $x \to x + \hat{i}$. The hard mode current j at every lattice site is defined via

$$j_0(x) = \frac{m^2}{2\sqrt{\pi}}W_{00}(x) \quad \text{and} \quad j_i(x) = \frac{m^2}{4\pi}v_m^{i*}W_{1m}(x). \qquad (9.36)$$

where the effective mass appears in lattice units $m \leftrightarrow am$. Since the chromo-magnetic field does not couple directly to the hard mode current the equation of motion for the links $\dot{U} = iE_iU_i$ and thus the definition for the chromo-electric field remain unchanged. The Gauss constraint takes the following form upon taking the adjoint charge j^0 of hard modes at every lattice site into account (see figure 7.17):

$$\sum_i \Big(E_i(x) - U_{-i}(x)E_i(x - \hat{i})U_{-i}^+(x) \Big) = j_0(x). \qquad (9.37)$$

Using the scaling relations $E \leftrightarrow a^2gE$, $W \leftrightarrow agW$, $m \leftrightarrow am$ and $t \leftrightarrow t/a$ between continuum quantities and their lattice counterparts, it is straightforward to show that these equations reduce to the corresponding kinetic equations in the continuum upon taking the limit $a \to 0$. The discretization of the Vlasov equation (9.6) is also straightforward and complicated only by the term
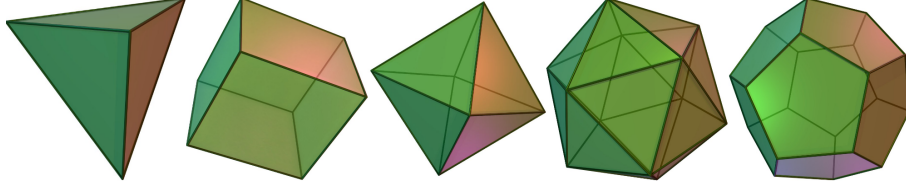
Figure 9.2: An alternative scheme for the discretization of the unit sphere of directions $\boldsymbol{v}$ relies an platonic solids. The scheme fully respects the symmetries of the lattice upon choosing the correct orientation for the solids.

involving the chromo-magnetic field $B_i(x)$ which vanishes in thermal equilibrium:

$$
\begin{aligned}
\dot{W}_{lm} \;=\; & -C^i_{lml'm'}\frac{1}{2}\left(U_i(x)W_{l'm'}(x+i)U^+_i(x) - U_{-i}(x)W_{l'm'}(x-i)U^+_{-i}(x)\right) + \qquad (9.38) \\
& + {}^E X^i_{lm}\frac{1}{2}\left(E_i(x) + U_{-i}(x)E_i(x-i)U^+_{-i}(x)\right) + {}^B X^i_{lm}\frac{1}{2}\left(B_i(x) + U_{-i}(x)B_i(x-i)U^+_{-i}(x)\right).
\end{aligned}
$$

The chromo-magnetic field on the lattice appearing in this equation can be discretized in the following form which is illustrated in figure 9.1

$$
B^a_i(x) = \operatorname{Im} \operatorname{Tr} T^a \left(U_{i,j}(x) + U_{j,-i}(x) + U_{-i,-j}(x) + U_{-j,i}(x)\right) \qquad (9.39)
$$

By using the Baker-Campbell Haussdorff formula to expand plaquettes in the lattice spacing it is straightforward to show that this expression will reduce to the chromo-magnetic field in the continuum limit up to a rescaling to lattice units $B_i \leftrightarrow agB_i$. There exist different less general discretization schemes to simulate the Yang-Mills Vlasov equations (9.5,9.6) on the lattice in thermal equilibrium. The problem to discretize the unit sphere of directions S^2 for the hard-mode distribution $W(x,v) : \mathbb{R}^{3+1} \times S^2 \to \mathbb{R}$, while respecting the symmetries of the lattice, has also been solved by replacing S^2 with suitably oriented platonic solids [95]. In this scheme every vertex $\mathbf{v}_n$ of the platonic solid p at an arbitrary lattice position x is associated with a field $W(x,\mathbf{v}_n)$. Spherical integrals are represented as sums over the vertices of the solid with the area $A_p = \frac{4\pi}{N_p}$ assigned to every vertex. N_p is the number of vertices of the used solid p. Since there are only 5 platonic solids, the precision with which the hard modes can be simulated is limited. The approach respects the symmetries of the lattice upon choosing a suitable orientation for the solid however and facilitates the implementation of fast kinetic algorithms. The hard mode current takes the following form on the lattice

$$
j^\mu(x) = \frac{(am_D)^2}{N_p}\sum_n v^\mu_n W(x,\mathbf{v}_n), \qquad (9.40)
$$

where the sum runs over all vertices of the platonic solid and $v_n = (1,\mathbf{v}_n)$. The equations of motion for magnetic and electric fields (9.35) as well as the Gauss constraint (9.37) are formally unchanged. It is straightforward to derive the appropriate equation of motion for the hard mode distribution in thermal equilibrium:

$$
\partial_t W_n(x) = v^i_n(E_i(x) - \frac{1}{2}[U_i(x)W_n(x+i)U^+_i(x) - U_{-i}(x)W_n(x-i)U^+_{-i}(x)]). \qquad (9.41)
$$

To study non-equilibrium situations an expansion in spherical harmonics should be preferred due to the higher precision with which the unit sphere of directions can be approximated. Independent

of the chosen discretization scheme it is important to point out that the physics of electric and magnetic gauge fields remains shaped by discretization artifacts at the hard scale. Quantities defined at the hard scale are thus shaped by the intricacies of the discretization scheme, and the hydrodynamics of the lattice system consequently remains inconsistent with continuum physics. The purpose of the introduction of effective hard mode fields is instead to lessons the impact of these discretization artifacts on the physics at the soft scale and to introduce the leading order contributions of hard thermal loops which shape the structure of perturbation theory in thermal media. In addition, as alluded to in the first section of this chapter, the introduction of hard mode fields allows to safely take the continuum limit without encountering a divergence in the energy density.

9.6 Leap-Frog Integrator

For a numerical integration of the kinetic equations on the lattice some care must be taken to ensure that the update step for a discrete time difference Δ_t is symplectic and respects the symmetries of the equations of motion in continuous time (9.5,9.6). It is particularly important to ensure a symmetry with respect to parity and time reversal to minimize discretization artifacts and avoid instabilities. The symmetrization described in this section is used to update the chromo-electric, -magnetic and hard mode fields on the lattice in the context of a leap-frog scheme. Electric fields $E_i(x)$ will be defined at half time steps while links $U_i(x)$ and hard mode fields $W_{lm}(x)$ are defined at full time steps. The link update remains unchanged with respect to the purely classical simulations:

$$U_i(x + \Delta_t) = \exp(i\Delta_t E_i(x + \frac{1}{2}\Delta_t))U_i(x) \tag{9.42}$$

The hard mode current $j_i(x)$ must be taken into account when updating electric fields and the corresponding update for the purely classical theory is therefore modified to take the following form

$$
\begin{aligned}
E_i(x + \frac{1}{2}\Delta_t) &= E_i(x - \frac{1}{2}\Delta_t) + 2\Delta_t T^a \text{Im Tr}[T^a \sum_{|j|\neq i} U_{ij}(x)] + \\
&\quad + \frac{1}{2}\Delta_t \left[j_i(x) + U_i(x)j_i(x+i)U_i^+(x) \right].
\end{aligned}
\tag{9.43}
$$

The Gauss constraint can be expressed in a symmetrized form as:

$$\sum_i \left(E_i(x + \frac{1}{2}\Delta t) - U_{-i}(x)E_i(x - i + \frac{1}{2}\Delta t)U_{-i}^+(x) \right) = \frac{(am_D)^2}{4\sqrt{\pi}} \left(W_{00}(x) + W_{00}(x + \Delta_t) \right). \tag{9.44}$$

A more subtle scheme is required to update hard mode fields while respecting the original symmetries of (9.6) with respect to parity and time reversal. The following update scheme is used

$$
\begin{aligned}
W_{lm}(x + \Delta_t) &= W_{lm}(x - \Delta_t) + 2\Delta_t(^E X_{lm}^i E_{ave,i}(x) + {}^B X_{lm}^i \left(B_i(x) + U_{-i}(x)B_i(x-i)U_{-i}^+(x) \right) \\
&\quad - \frac{1}{2}C_{lml'm'}^i[U_i(x)W_{l'm'}(x+i,t)U_i^+(x) - U_{-i}(x)W_{l'm'}(x-i)U_{-i}^+(x)]) \tag{9.45}
\end{aligned}
$$

where the symmetrized electric field $E_{ave,i}$ is defined as:

$$
\begin{aligned}
E_{ave,i}(x,t) &= \frac{1}{4}[E_i(x-\frac{1}{2}\Delta_t)+U_{-i}(x)E_i(x-i-\frac{1}{2}\Delta_t)U_{-i}^+(x) \\
&\quad +E_i(x+\frac{1}{2}\Delta_t)+U_{-i}(x)E_i(x-i+\frac{1}{2}\Delta_t)U_{-i}^+(x)].
\end{aligned}
\tag{9.46}
$$

Note that the hard mode fields defined at subsequent time steps are updated independently of each other and that a potential problem with *doublers* exists. These doublers are discussed in some detail in [91].

9.7   Generating the Ensemble in Thermal Equilibrium

To obtain thermal averages of time dependent quantities the problem of generating an ensemble of field configurations according to the classical partition function Z_{cl} must be solved. In this section a generalization of the thermalization procedure previously introduced for the purely classical lattice model is suggested. The partition function for the classical theory supplemented with the effective hard mode distribution takes the following form in the continuum:

$$
Z_{cl} = \int [DA][DE][DW]\ \delta(D_i E^i + \frac{m_D^2}{2\sqrt{\pi}}W_{00})\ e^{-\beta H_{kin}}.
\tag{9.47}
$$

The δ-function restricts the partition function to include only field configurations satisfying Gauss's law. The spherical components are constrained by the demand that the momentum distribution is real

$$
W_{l,-m}(x) = (-1)^m W_{l,m}^+(x)
\tag{9.48}
$$

and the integration over the W-fields is therefore defined as an integration over a complete subset of independent adjoint components of the fields W_{lm} at each point in space. The Hamiltonian for kinetic theory was derived in [92] and takes the following form:

$$
H_{kin} = \int d^3x\ \mathrm{Tr}\left[-E_i E^i + \frac{1}{2}F_{ij}F^{ij} + \frac{m_D^2}{4\pi}W_{lm}W_{lm}\right].
\tag{9.49}
$$

To extend the Monte Carlo techniques for the generation of the partition function to kinetic theory the Gauss constraint is again reexpressed using the identity

$$
\delta(D_i E^i + \frac{m_D^2}{2\sqrt{\pi}}W_{00}) = \int [D\varphi]\ \exp\left\{i\beta\int d^3x \mathrm{Tr}\left[\left(E^i D_i - \frac{m_D^2}{2\sqrt{\pi}}W_{00}\right)\varphi\right]\right\},
\tag{9.50}
$$

where $\varphi = \varphi^a T^a$ is an appropriately scaled adjoint scalar field corresponding to the component A_0 of the gauge field. The covariant derivative is again removed from the electrical field in the exponent by partial integration. The partition function (9.47) can now be rewritten as:

$$
\begin{aligned}
Z_{cl} &= \int [DA][DE][DW][D\varphi]\ \exp\left\{-\beta\int d^3x \mathrm{Tr}[\frac{1}{2}F_{ij}F^{ij} - E^i(E_i + iD_i\varphi)\right. \\
&\quad \left. +i\frac{m_D^2}{2\sqrt{\pi}}W_{00}\varphi + \frac{m_D^2}{4\pi}W_{lm}W_{lm}]\right\}.
\end{aligned}
\tag{9.51}
$$

Upon performing the Gaussian integrations over the adjoint components of color electric fields as well as the components of the hard mode distribution the partition function of a Yang-Mills theory coupled to an adjoint Higgs field is obtained:

$$Z_{cl} = \int [\mathrm{D}A][\mathrm{D}\varphi] \ \exp\left\{ -\beta \int \mathrm{d}^3x \mathrm{Tr}\left[\frac{1}{2}F_{ij}F^{ij} - \frac{1}{4}\mathrm{D}_i\varphi\mathrm{D}^i\varphi + \frac{m_D^2}{4}\phi^2 \right] \right\}. \tag{9.52}$$

In contrast to the partition function for the purely classical theory the Higgs field is now massive with a scalar mass proportional to the Debye mass m_D. Upon making the transition to the lattice the partition function takes the form

$$Z_L = \int [\mathrm{D}U][\mathrm{D}\varphi] \ \mathrm{e}^{-\beta H_L}, \tag{9.53}$$

where the lattice Hamiltonian is:

$$H_L = \sum_x \left[\beta_L \sum_{i<j}\left\{ 1 - \frac{1}{N}ReTrU_{ij} \right\} + \frac{\beta_L}{N}Tr\left\{ \phi(x)\phi(x) - \kappa\sum_i \phi(x)U_i(x)\phi(x+\hat{i})U_i^+(x) \right\} \right]. \tag{9.54}$$

The adjoint Higgs φ, defined at every lattice site, is expressed in lattice units $a^2 g\varphi \to 2\sqrt{\kappa}\varphi$. The Hamiltonian is formally identical to the one used to represent the partition function for the purely classical lattice theory. The only practical difference consists in the choice of the hopping parameter which is now defined as [80, 81]

$$\kappa^{-1} = \frac{am_D^2}{8} + 3. \tag{9.55}$$

The adjoint Higgs again serves an auxiliary field to generate an ensemble of gauge field configurations according to the partition function (9.53). The electrical as well as hard mode fields are drawn subsequently from Gaussian distributions and projected onto the hypersurface of field configurations satisfying the Gauss constraint. A caveat of the thermalization procedure outlined here is that the relation between the partition function of the semi-classical theory and Yang-Mills theory with an adjoint Higgs has been established in the continuum and is not exact for the lattice theory. It is however again possible to combine this technique with conventional thermalization techniques [91] which can subsequently be applied to approach the exact equilibrium distribution to arbitrary precision.
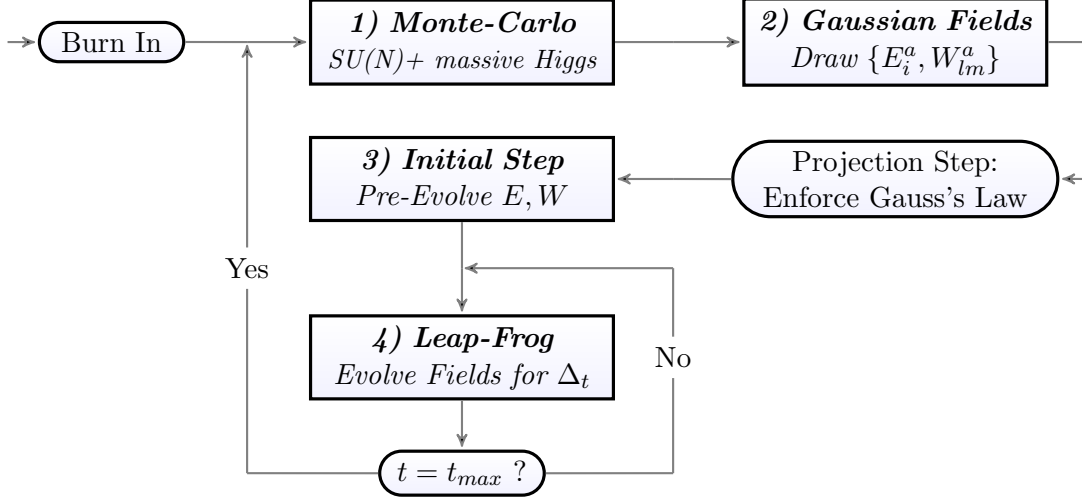
Figure 9.3: Flow chart illustrating the structure of the kinetic theory simulations in thermal equilibrium. The general layout is similar to layout of the purely classical simulation introduced in chapter 7.

9.8   Structure of the Simulation for Thermal Equilibrium

The general structure of the classical lattice simulation is shown in figure 9.3. The following parts of the algorithm require a detailed discussion:

1. *Generation of Gauge Fields*

    To generate an ensemble of link configurations according to (9.53) the overrelaxed heatbath algorithm for the purely classical theory is used. The hopping parameter is now chosen as:

    $$\kappa^{-1} = \frac{am_D^2}{8} + 3. \tag{9.56}$$

2. *Generation of Electrical and Hard-Loop Fields*

    The electrical fields $\{E_i(x)\}$ as well as Hard-Loop fields $\{W_{lm}(x)\}$ can be drawn from a Gaussian according to (9.53). While the electrical fields are drawn from a Gaussian with variance $\sigma_E^2 = 2N/\beta_L$, the adjoint components of Hard-Loop fields W_{lm} are drawn from Gaussians with variance $\sigma_{m>0}^2 = 4N\pi/am_D^2\beta_L$ for $m > 0$. The real parts of W_{l0} are drawn from Gaussians with variance $\sigma_{m=0}^2 = 8N\pi/am_D^2\beta_L$.

3. *Initial Time Step of the Leapfrog Integrator*

    To perform the first step of the leap-frog integrator electrical fields are evolved for $1/2\Delta_t$ and hard mode fields subsequently for a full time-step Δ_t.

4. *Classical Time Evolution*

    The leap-frog integrator for the purely classical theory has been modified to take the presence of the effective hard mode fields into account. The properly symmetrized update steps consist of the set of equations (9.43),(9.45) and (9.42) executed in the order of appearance.

10 Non-Abelian Plasma Instabilities

In any field, find the strangest thing and then explore it.

John Archibald Wheeler

Hydrodynamic simulations have been shown to provide an excellent fit to the experimental data from heavy-ion collisions at RHIC assuming that a hydrodynamic behavior sets in at a very early stage of the collision. The necessary rapid establishment of a local thermal equilibrium is puzzling from a theoretical point of view and resists an explanation by perturbative techniques which yield significantly larger thermalization times. In QED the rapid formation of a plasma in the presence of an anisotropic background current is known to be driven by the so called Weibel instability, and it has been argued by Mrowczinski [56] that analogous non-abelian instabilities might also drive the formation of a quark-gluon plasma in heavy ion collisions. These instabilities will be investigated numerically in the following for a strongly anisotropic SU(2) and SU(3) medium.

10.1 Weibel-Instability

This section will serve as an introduction to the Weibel instability in classical electrodynamics to provide a solid foundation for the discussion of non-abelian plasma instabilities in the rest of this chapter. The Weibel instability is well known to drive the formation of a plasma in the presence of an anisotropic background current. The discussion will follow the lines of the original article by Erich S. Weibel from 1959 [96]. The physical system that will be investigated in the following consists of freely moving electrons with charge e and mass m which interact via an electromagnetic field described by the set of homogeneous

$$\dot{\boldsymbol{B}}(x) = -\nabla \times \boldsymbol{E}(x), \quad \dot{\boldsymbol{E}}(x) = \nabla \times \boldsymbol{B}(x) - \boldsymbol{j}(x) \tag{10.1}$$

and inhomogeneous Maxwell equations:

$$\nabla \cdot \boldsymbol{E}(x) = -j^0(x), \quad \nabla \cdot \boldsymbol{B} = 0. \tag{10.2}$$

The space-time position is denoted as $x \in \mathbb{R}^{3+1}$ while j is the 4-current of electrons. The Boltzmann transport equation for the phase space distribution of electrons $f(x, \boldsymbol{p})$ takes the following form neglecting the collision term

$$\partial_t f = -\boldsymbol{v} \cdot \nabla_x f - \frac{\mathrm{e}}{m} \left[\boldsymbol{E} + \boldsymbol{v} \times \boldsymbol{B} \right] \cdot \nabla_v \bar{f}, \tag{10.3}$$

where $\bar{f}(\boldsymbol{p})$ is the distribution of background charges and $v_p = (1, \boldsymbol{p}/p)$ is defined as usual. Note that the reasoning for omitting the collision term is that since $T \gg \mathrm{e}^2/\bar{r}$, where $\bar{r} \sim T^{-1}$ is the average inter-particle spacing, the plasma is *rarefied*, i.e. collisions can be neglected since the average energy of a particle is much higher than the potential between two particles [18]. The 4-current j is obtained from the electron distribution f via:

$$j^\mu = \mathrm{e} \int \mathrm{d}^3\boldsymbol{p} \, v^\mu f. \tag{10.4}$$

The background distribution $\bar{f}$ is assumed to evolve on time and length scales much larger than those relevant for the electron distribution and is therefore treated as static and homogeneous. An example for such a slowly evolving background distribution is the distribution of nuclei in an ionization plasma. The set of homogeneous Maxwell equations and the Boltzmann equation combined with Gauss law are the abelian counterpart to the Yang-Mills Vlasov equations as defined in (9.1). Note that there is no counterpart to $\nabla \times \boldsymbol{B} = 0$ in the Yang-Mills Vlasov equations since this would require a complete gauge fixing. Since the purpose of fixing to a temporal gauge merely consists in establishing a canonical formalism with electrical fields forming the conjugate momenta to spatial gauge fields, a complete gauge fixing is not necessary. The aim of the following discussion is to illustrate the existence of unstable modes in the presence of a non-isotropic background distribution. As a first step in the derivation of the dispersion relations for the medium a Fourier transform of the Boltzmann equation with respect to the spatial coordinate is performed

$$\mathrm{i}(\omega + \boldsymbol{k} \cdot \boldsymbol{v})f = -\frac{\mathrm{e}}{m\omega}\left\{\omega \boldsymbol{E} \cdot \nabla_v \bar{f} + [\boldsymbol{k} \times \boldsymbol{E}] \cdot [\boldsymbol{v} \times \nabla_v \bar{f}]\right\}, \tag{10.5}$$

where the magnetic field has been eliminated using the homogeneous Maxwell equations. The anisotropic background distribution is again assumed to have a cylindrical symmetry with respect to the z-axis

$$\bar{f} = \bar{f}(v_0, v_3), \tag{10.6}$$

where the radial coordinate $v_0^2 = v_1^2 + v_2^2$ has been introduced. The general solution of the Boltzmann equation for a cylindrically symmetric system is known and given by the expression:

$$f(K, v_0, v_3) = -\mathrm{i}\frac{\mathrm{e}}{m\omega}\frac{v_1 E_1 + v_2 E_2}{v_0(\omega + kv_3)}\left\{kv_0\frac{\partial \bar{f}}{\partial v_3} - (\omega + kv_3)\frac{\partial \bar{f}}{\partial v_0}\right\}. \tag{10.7}$$

Using the inhomogeneous Maxwell equations Faradays law of induction is rewritten as

$$(\omega^2 - \boldsymbol{k}^2)\boldsymbol{E} = \boldsymbol{k}j^0 - \omega\boldsymbol{j}. \tag{10.8}$$

The electrical field can now be eliminated from (10.7) by summing over the x- and y- components of this relation to obtain the general dispersion relation:

$$k^2 - \omega^2 = \frac{\mathrm{e}^2}{m}\pi \int_0^\infty \mathrm{d}v_0 \int_{-\infty}^\infty \mathrm{d}v_3 \frac{v_0^2}{\omega + kv_3}\left\{(\omega + kv_3)\frac{\partial \bar{f}}{\partial v_0} - kv_0\frac{\partial \bar{f}}{\partial v_3}\right\} \tag{10.9}$$

To illustrate the appearance of unstable modes a more specific form of the background distribution is assumed

$$\bar{f}(\boldsymbol{v}) = \frac{n}{u_0^2 u_3 (2\pi)^{\frac{3}{2}}}\exp\left[-\frac{v_0^2}{2u_0^2} - \frac{v_3^2}{2u_3^2}\right] \tag{10.10}$$

where the parameters u_i are arbitrary. The dispersion relation for this medium takes the form

$$k^2 - \omega^2 = \frac{n\mathrm{e}^2}{m}\left\{c - \left([c+1]\frac{\omega}{u_3 k}\right)\varphi\left(\frac{\omega}{u_3 k}\right)\right\} \tag{10.11}$$

where

$$c = \left(\frac{u_0}{u_3}\right)^2 - 1 \quad \text{and} \quad \varphi(z) = \exp(-\frac{1}{2}z^2)\int_{-\mathrm{i}\infty}^z \mathrm{d}\xi \ \exp(\frac{1}{2}\xi^2). \tag{10.12}$$
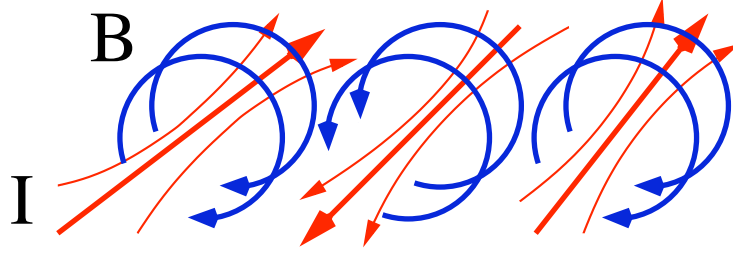
Figure 10.1: Illustration of the Weibel instability. The anisotropic background distribution induces a magnetic field in the transverse plane which causes a filamentation of the electron current. This filamentation in turn increases the magnetic field leading to a self-energizing process.

In the limit where $\omega/u_3 k$ is large the dispersion relation has a solution of the form

$$\omega \simeq \mathrm{i} u_0 \left(\frac{n e^2}{m} \right) \frac{k}{\sqrt{\left(\frac{n e^2}{m} \right)^2 + k^2}} \tag{10.13}$$

which is purely imaginary. The existence of imaginary solutions for ω with appropriate sign indicate the presence of exponentially growing plasma modes upon performing the Fourier transform back to a space-time representation. The presence of an anisotropic background distribution will therefore lead to a rapid growth of magnetic and electric energy densities. The associated physical process is illustrated in the upper part of figure 10.1. The anisotropic background distribution induces a magnetic field in the transverse plane which causes initial inhomogenities of the electron current. A filamentation ensues which increases magnetic fields in the transverse plane as illustrated in figure 10.1 leading to further filamentation. The effect of this mechanism is a self-energizing process which leads to a rapid growth of the energy density of the magnetic field as well as the induction of an electric field along the direction of the symmetry axis. The filamentation of the electron current has been verified experimentally in high intensity laser experiments [97].

10.2   Non-Abelian Instability and Plasma Formation

To illustrate that the results derived in the previous section for QED in the classical limit are of relevance to the kinetics of QCD encountered in heavy-ion collisions, it is instructive to focus on the initial phase of plasma formation. For magnetic and electric fields of low intensity the Yang-Mills equations in a temporal gauge can be expanded in the set of fields $\{A_i^a, E_i^a\}$ to arrive at the following field equations:

$$\begin{aligned}
\partial_t \boldsymbol{E}^a(x) &= \nabla \times \boldsymbol{B}^a(x) - \boldsymbol{j}^a(x) \\
\partial_t \boldsymbol{B}^a(x) &= -\nabla \times \boldsymbol{E}^a(x), \\
\nabla \cdot \boldsymbol{E}^a(x) &= -(j^0)^a(x).
\end{aligned} \tag{10.14}$$

The classical Yang-Mills field equations are therefore identical to a set of Maxwell equations for $N^2 - 1$ independent electromagnetic fields . A similar observation is made for the Vlasov equation for the distribution of hard plasma modes

$$\partial_t f^a = -\boldsymbol{v} \cdot \nabla_x f^a + g(\boldsymbol{E}^a + \boldsymbol{v} \times \boldsymbol{B}^a) \cdot \nabla_p \overline{f} \tag{10.15}$$
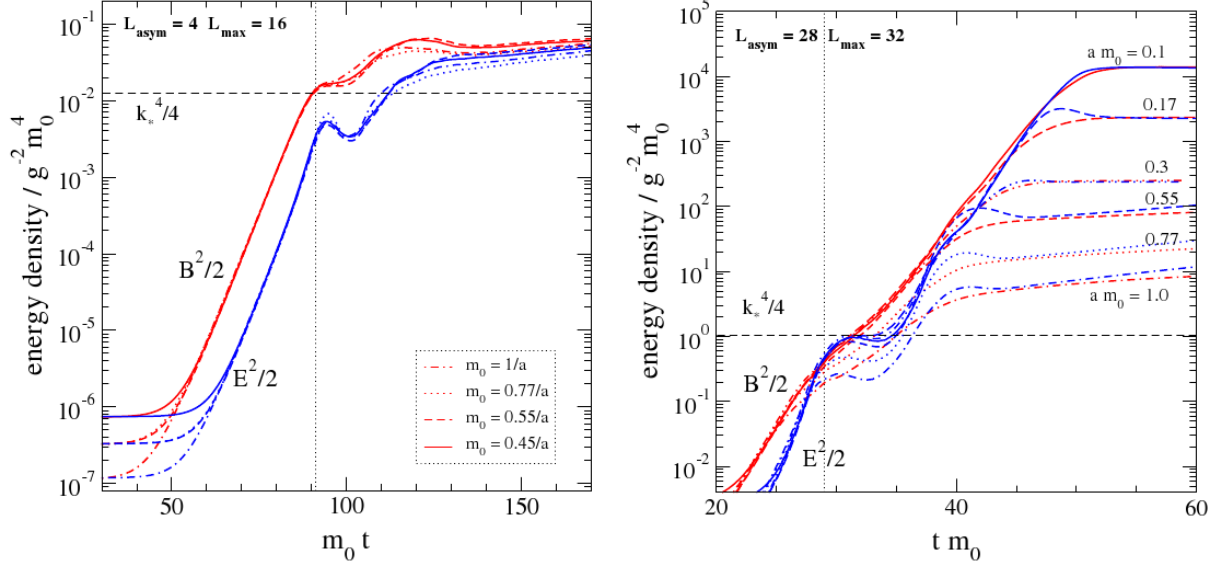
Figure 10.2: Growth rate of the electric and magnetic energy densities in the presence of an anisotropic background distribution for SU(2) as obtained by Rummukainen and Bödecker [99].

which is identical to its abelian counterpart with the quotient $-e/m$ replaced by the gauge coupling g. The adjoint components of the Yang-Mills fields as well as the corresponding components of the hard mode distribution are therefore fully decoupled for weak fields and evolve according to the same set of equations that applies for a QED plasma. The analysis from the previous section can therefore also be applied to QCD at weak fields. It is therefore expected from a classical analysis that an anisotropic hard mode background, as it is present in heavy-ion collision will induce a rapid field growth in the initial phase of the collision. The difference to the QED case is, however, that as soon as the fields have grown to a sufficient strength, the non-linear terms, representing the gluon self-interaction, become relevant. At this point the analysis from the previous section is compromised which is of particular importance, since only at sufficiently high occupation numbers a classical analysis can be expected to capture the physics of the full quantum theory correctly. It is precisely at this point, where the classical picture of the Weibel instability, discussed in the previous section, breaks down. Several studies were performed to investigate the fate of the Weibel instability in the non-abelian regime. The initial results for a 3-dimensional system were disappointing [98] and indicate that the field growth is curbed in the non-abelian regime and the initially exponential growth rates of energy densities become increasingly damped. The existence of a second phase of field growth was observed as well with energy densities showing a sudden exponential growth deep in the non-abelian regime. The nature of this secondary instability remains ill understood and numerous explanations have been put forward. Recent studies for SU(2) [99, 100] have shown that for extremely anisotropic background distributions a strong and sustained field growth occurs in the non-abelian regime shortly after the initial field growth caused by the Weibel instability has abated. It is the purpose of the study presented in the following to investigate this phenomenon in the context of the kinetic framework introduced in the previous section for a maximally anisotropic system. The gauge groups SU(2) and SU(3) will be studied.

10.3   Simulation of the Non-Abelian Plasma Instability

To simulate the Chromo-Weibel instability for an extremely anisotropic background distribution in the context of the semi-classical framework introduced in the previous chapter the constants $^{E}X^{i}_{lm}$ and $^{B}X^{i}_{lm}$ entering the Vlasov equation (9.38) must be determined. In addition, suitable initial conditions to simulate the onset of the instability must be chosen. The set of constants $\{^{E}X^{i}_{lm}, {}^{B}X^{i}_{lm}\}$ is determined from the angular distribution

$$\Omega = \frac{1}{m^2}M, \quad M = 4\pi g^2 \int_0^\infty \frac{\mathrm{d}p\ p^2}{(2\pi)^3} \frac{\bar{f}(p\boldsymbol{v}_p)}{p} \tag{10.16}$$

which parametrizes the hadronic background distribution. The effective mass which normalizes the distribution M is defined as:

$$m^2 = \int \mathrm{d}\Omega_v\ M. \tag{10.17}$$

In thermal equilibrium the effective mass corresponds to the Debye mass m_D. The background distribution $\bar{f}(\boldsymbol{p})$ which will be assumed in the following is the anisotropic bosonic distribution which has been introduced in chapter 5 in the limit of maximal anisotropy $\xi \to \infty$

$$\bar{f}(p) = \lim_{\xi\to\infty} \sqrt{1+\xi}n_B(p\sqrt{1+\xi(\boldsymbol{v}_p\cdot\boldsymbol{n})^2}) = \delta(\boldsymbol{v}_p\cdot\boldsymbol{n})h(p) \tag{10.18}$$

where

$$h(p) = \int_{-\infty}^{\infty} \mathrm{d}x\ n_B(p\sqrt{1+x^2}). \tag{10.19}$$

The anisotropy vector $\boldsymbol{n}$ is chosen to coincide with the unit vector in the z-direction as usual. The normalized angular distribution Ω and the effective mass therefore take the form:

$$\Omega = \frac{1}{2\pi}\delta(\boldsymbol{v}_p\cdot\boldsymbol{n}) \quad \text{and} \quad m^2 = \frac{\pi^2}{6}g^2T^2. \tag{10.20}$$

Starting with the constants $^{E}X^{i}_{lm}$ relevant for the electrical component of the Vlasov equation (9.38) the following integral (9.33) must be evaluated:

$$^{E}X^{i}_{lm} = \frac{1}{2\pi}\int \mathrm{d}\Omega_v Y^*_{lm}(v)\left(-\frac{\partial}{\partial v^i} + 2v^i\right)\delta(v^3)\bigg|_{v=1}. \tag{10.21}$$

Using the definition of the spherical harmonics

$$Y_{lm}(\vartheta,\phi) = N_{lm}e^{im\varphi}P^m_l(\cos\theta), \quad N_{lm} = \sqrt{\frac{(2l+1)(l-m)!}{4\pi(l+m)!}} \tag{10.22}$$

from the associated Legendre polynomials P^m_l as well as the identity

$$\frac{\mathrm{d}}{\mathrm{d}x}P^m_l(x) = \frac{-(l+1)xP^m_l(x) + (1+l-m)P^m_{l+1}(x)}{-1+x^2} \tag{10.23}$$

it is straightforward to obtain an explicit expression for the constants:

$$
{}^{E}\boldsymbol{X}_{lm} = N_{lm}\delta_{|m|1}P_l^m(0)\begin{pmatrix} 1 \\ -\mathrm{i}\,\mathrm{sgn}(m) \\ 0 \end{pmatrix} - N_{lm}\delta_{m0}(l+1)P_{l+1}^0(0)\begin{pmatrix} 0 \\ 0 \\ 1 \end{pmatrix}. \tag{10.24}
$$

The calculation of the corresponding constant ${}^{B}X_{lm}^i$ is performed along analogous lines. From (9.33) the following integral needs to be determined:

$$
\begin{aligned}
{}^{B}X_{lm}^i &= \frac{1}{2\pi}\epsilon_{ijk}\int \mathrm{d}\Omega_v\; Y_{lm}^*(v)v^j\frac{\partial}{\partial v^k}\delta(v^3)\Big|_{v=1} \\
&= -\frac{1}{2}\epsilon_{ij3}\delta_{|m|1}\left(\delta_{j1}-\mathrm{i}\,\mathrm{sgn}(m)\delta_{j2}\right)N_{lm}\frac{\partial}{\partial v^3}P_l^m(v^3=0) \tag{10.25}
\end{aligned}
$$

The derivative of the Legendre polynomial is again obtained using the identity (10.23) which leads to the following final expression for the constants:

$$
{}^{B}\boldsymbol{X}_{lm} = -\frac{1}{2}N_{lm}\delta_{|m|1}(1+l-m)P_{l+1}^m(0)\begin{pmatrix} \mathrm{i}\,\mathrm{sgn}(m) \\ 1 \\ 0 \end{pmatrix} \tag{10.26}
$$

It is evident that the constants vanish for $i=3$ and that the hard modes therefore couple only to magnetic fields in the transverse plane as expected. Note that the set of indices $\{l,m\}, |m|\le l$ is restricted to a finite subset by introducing a spherical cutoff $l_{max}\ll 1$ for practical applications with the set of indices contained in the subset satisfying $l\le l_{max}$. Initial field configurations for the classical time evolution are generated by formally assuming the classical system to be in a thermal equilibrium at very low temperature at the initial time and employing the Monte-Carlo techniques discussed in the preceeding chapter. Note that the purpose of this procedure is merely to generate small initial field fluctuations respecting the Gauss constraint. These fluctuations are required for a non-trivial time evolution of the system.

10.4   Physical Result

The time trajectories for electric and magnetic energy densities,

$$
\mathscr{E}_E = \frac{1}{6N}\mathrm{Tr}\langle E_i E_i\rangle \quad \text{and} \quad \mathscr{E}_B = 1 - \frac{1}{N}\mathrm{Re}\,\mathrm{Tr}\sum_{ij}\langle U_{ij}\rangle \tag{10.27}
$$

are shown in figure 10.3 for SU(2) and SU(3) at three different values of the effective mass . All results were obtained on lattices with volume $(20a)^3$ and spherical cutoff $l_{\max}=16$. A further increase of the spherical cutoff does not alter the observed growth rates significantly. It is observed however that the duration of the intermittent lapse in growth rates is reduced upon increasing $l_{\max}=16$. An increase in the lattice volume is desirable, even though no qualitative change in the result can be expected. The results confirm previous observations that the exponential growth of energy densities in the presence of a strongly anisotropic hadronic background distribution continues into the strong field regime. As illustrated in figure 10.3, an unabated growth of energy densities is observed in the limit of asymptotically strong anisotropy with initial growth rates
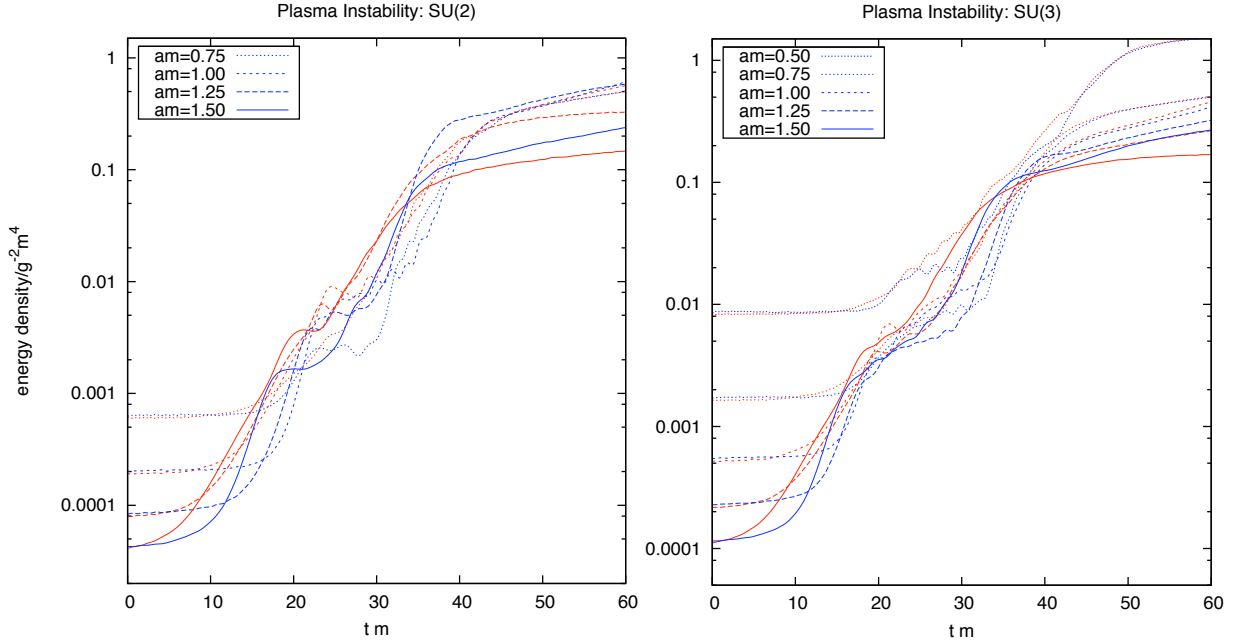
Figure 10.3: *Left:* Growth rates of the electric (blue) and magnetic (red) energy densities at extreme anisotropy for SU(2) obtained on lattices with volume $(20a)^3$ and spherical cutoff $l_{\max} = 16$. *Right:* The growth rates for SU(3) using a similar lattice layout are in astonishing agreement with the rates for SU(2) for identical effective masses m.

associated with the Weibel instability at weak fields continuing deep into the non-abelian regime. The measurements presented here are the first time that plasma instabilities for SU(3) investigated in the full framework of kinetic theory. An astonishing agreement between the growth rates for SU(2) and SU(3) is observed at identical effective masses. After the initial exponential growth phase the accretion of energy is curbed with the magnetic energy density approaching a limiting value and the electric energy density growing at a significantly reduced rate. The magnetic energy on the lattice is bounded due to the compact nature of the plaquettes entering the corresponding expression, and the growth of energy densities is stopped once this limiting value is approached. The abating growth of energy densities after the initial exponential growth phase is therefore a lattice artifact. Expectations that non-abelian plasma instabilities serve as a possible explanation for the conjectured rapid formation of a quark-gluon plasma in the presence of a sufficiently anisotropic hadronic background are confirmed.

11 Summary

*Man cannot discover new oceans unless he has the courage
to lose sight of the shore.*

Andre Gide

The research presented in this thesis is now briefly summarized and discussed. Due to the multitude of different topics and techniques touched upon in the course of this thesis the results are presented in the form of an enumeration. For a more in depth discussion the reader is referred to the respective chapters of this thesis. The description of each topic is concluded by a listing of the corresponding publications and suggestions for additional research.
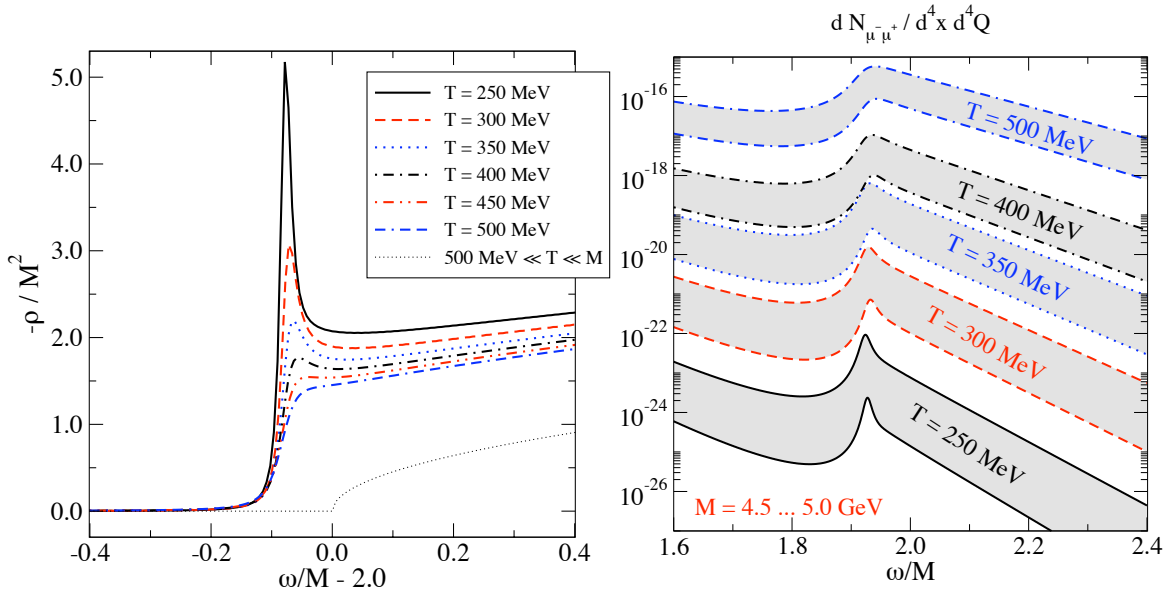
Figure 11.1: *Left:* Spectral function for bottomonium at rest($m_b = 4.5$ GeV) obtained from a numerical solution of the Schrödinger equation (4.4) using the Real-Time Static Potential [37]. *Right:* The expected quarkonium peak in the $\mu^-\mu^+$-emission spectrum from dissociation of quarkonium in the vector channel [38].

Real-Time Static Potential (Chapters 4,5,8) The Schrödinger equation describing quarkonia, i.e. the bound state of a charm or bottom quark with its anti-particle, in the vacuum is extended to generic media and used as the defining relation for a thermal quarkonium potential. The *real-time static potential*, an analogue to the QCD static potential for generic media, is obtained in the limit of infinite time and quark mass. This is the first time that an equivalent to the binding energy in the vacuum is suggested for thermal media which is rigorously defined from first principles. The real-time static potential consists of a real part which parametrizes the binding energy of the quarkonium state as well as an imaginary part parametrizing the decay width of the corresponding resonance. The potential is calculated to leading order in hard-thermal loop improved perturbation
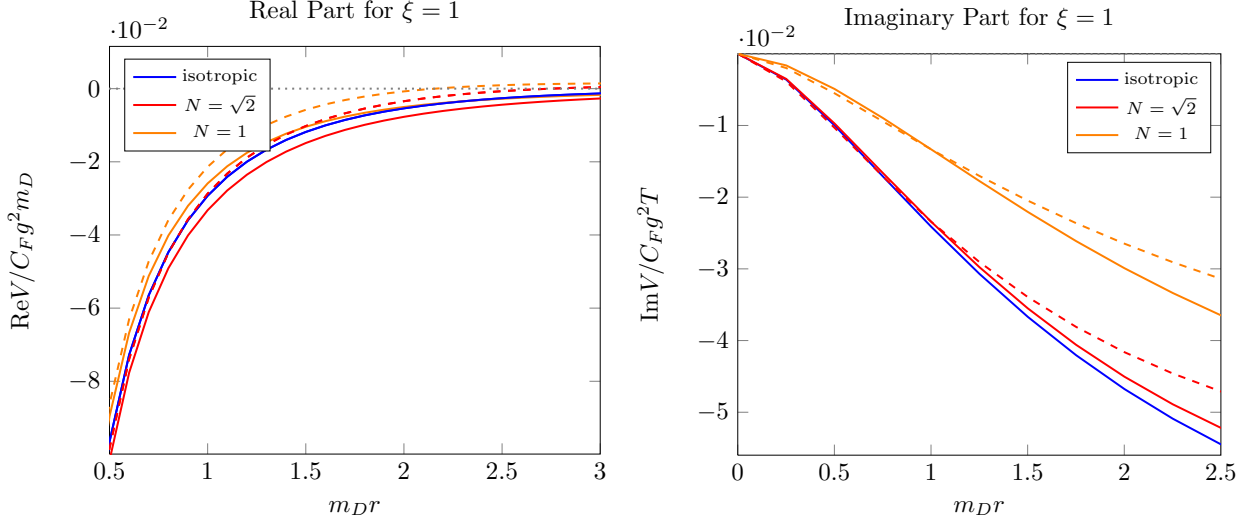
Figure 11.2: Real (left) and imaginary (right) part of the static potential. The blue curve corresponds to the isotropic plasma, $\xi = 0$, the other curves to $\xi = 1$ with normalization factor $N(\xi) = 1$ (orange) and $N(\xi) = \sqrt{1 + \xi}$ (red). The potential is evaluated for $\theta_r = \frac{\pi}{2}$ (solid) and $\theta_r = 0$ (dashed).

theory, where both components can be related directly to the retarded and symmetric components of the thermal gluon propagator. A direct relation to the quarkonium spectral function and thus the physical resonance as visible in the dilepton spectrum is established as illustrated in figure 11.1.

Suggested Research: The real-time static potential for a $q\bar{q}$-singlet, as presented here, is supplemented by a calculation of the corresponding potential for a $q\bar{q}$-pair transforming in the adjoint representation in the context of ongoing research. A calculation of the real-time static potential to second order in resummed perturbation theory is warranted.

Publications: JHEP **0703**, 054 (2007), JHEP **0709**, 066 (2007), PoS **LAT2007** 230 (2007), PoS **CONFINEMENT8** (2008) 118

Anisotropic Media (Chapters 5,10) A plasma with an anisotropy imposed on the momentum distribution of the system is considered and the real time static potential for quarkonia studied. The distribution function is normalized so as to preserve the particle number in an ideal gas as required in the Schwinger-Keldysh formalism. Contrary to recent findings without this normalization, a weak anisotropy does not lead to an increase in the melting temperature for bound states. The real time static potential obtained at weak anisotropy for different normalizations is shown in figure 11.2. To test for the maximal effect, the gluonic medium is also investigated in the limit of an asymptotically strong anisotropy. The spectral function of quarkonium is calculated for this case and found to be in remarkable qualitative agreement with the corresponding results for an isotropic medium. It is important to point out that these findings should also apply to other calculations where the normalization prefactor has been omitted. The results suggest that heavy quark observables in anisotropic media are difficult to distinguish from their counterparts in an isotropic medium. The case of asymptotically strong anisotropy is also considered in chapter 10, where the non-abelian plasma instabilities arising in such a medium are investigated in hard-loop improved lattice simulations.
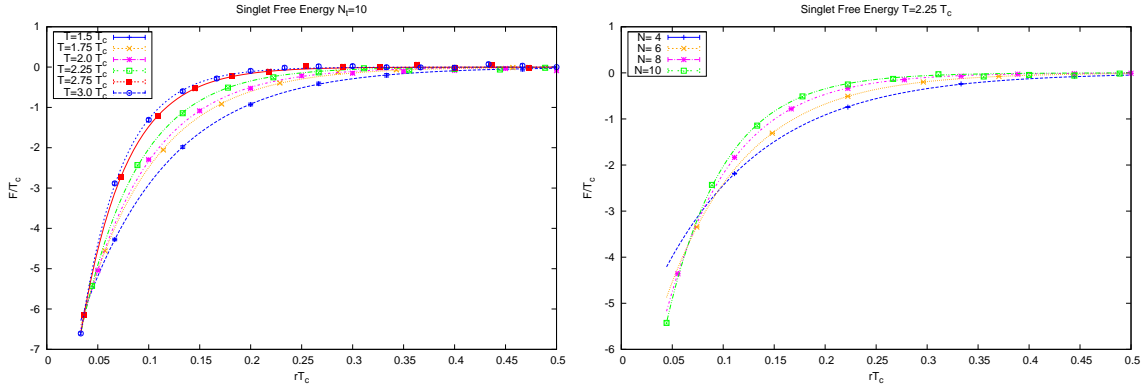
Figure 11.3: *Left:* The temperature dependence of the singlet free energy for $N_\tau = 10$. The screening mass, obtained by fitting the free energy against an exponential, depends linearly on the temperature. *Right:* The N_τ dependence of the result is shown for $T = 2.25T_c$. The free energy vanishes increasingly for finite r due to the diverging self energy of Wilson lines.

Suggested Research: Quantities calculated for anisotropic media, where the normalization prefactor has been omitted should be reconsidered. An attempt could be made to calculate the real-time static potential for arbitrary values of the anisotropy parameter.

Publications: arXiv:0908.1746 [hep-ph]

Monte Carlo Techniques (Chapters 6,7,9) An overview of Monte Carlo techniques for pure gauge theory is given in chapter 6, followed by a measurement of the singlet free energy of a static $q\bar{q}$-pair for Yang-Mills theory with gauge group SU(3) in 3 dimensions. The results are illustrated in figure **??** and supplemented by a brief lattice analysis of the Green-Karsch effective theory for SU(2) which serves as a naive toy model to capture many aspects of the thermal physics encountered in full Yang-Mills theory on coarse lattices. Monte-Carlo techniques are revisited in the context of classical and hard-loop improved lattice simulations, where they serve to generate a thermal ensemble of initial field configurations for a classical time evolution.

Note: The presented numerical analysis of the Green-Karsch effective theory as well as the measurement of singlet and adjoint components of the free energy in full Yang-Mills theory are part of ongoing research projects.

Classical Lattice Simulations and Non-Perturbative Corrections to Heavy Quark Observables (Chapters 7,8,9,10) Several chapters of this thesis are devoted to the development and analysis of a classical lattice model which captures the dynamics of soft gauge fields in a Yang-Mills plasma. The duality between the partition function of classical Yang-Mills theory and a euclidean Yang-Mills theory coupled to an adjoint Higgs is used to develop an efficient Monte-Carlo method for the generation of an ensemble of initial field configurations for the classical time evolution. The method virtually eliminates the spurious thermalization times plaguing conventional techniques. The technique is used to study the observed rapid thermalization of heavy quarks in the quark-
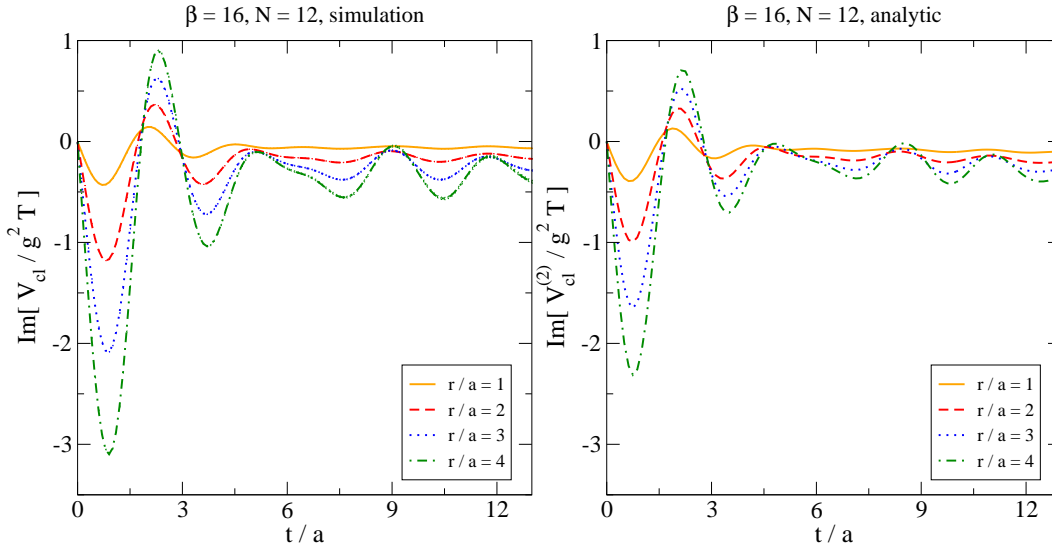
Figure 11.4: Time-dependence of the imaginary part of $V(t, \mathbf{r})$ as obtained from lattice-regularized perturbation theory and classical simulations.

gluon plasma. Non-perturbative effects due to the dynamics of soft classical fields are found to lead to a significant enhancement of the momentum diffusion of heavy quarks. It is shown that a reliable measurement of the diffusion constant in ordinary lattice simulations is feasible. The break-down of the classical lattice model in the strong coupling regime is analyzed in detail. Non-perturbative corrections to the imaginary of the real-time static potential due to classical field dynamics are measured and found to amplify the perturbative result by nearly 100%. The qualitative agreement between lattice regularized perturbation theory and results from the classical lattice simulations is illustrated in figure 11.4.

Suggested Research: Additional research is required to distinguish unphysical effects leading to a breakdown from genuine soft field dynamics at intermediate temperatures. The heavy quark diffusion constant should be measured in ordinary lattice simulations.

Publications: JHEP **0709**, 066 (2007), PoS **LAT2007** 230 (2007), PoS **CONFINEMENT8** (2008) 118, JHEP **0905**, 014 (2009)

Kinetic Theory and Non-Abelian Plasma Instabilities (Chapters 9,10) The classical lattice model is supplemented by leading order quantum corrections as obtained in hard-loop effective theory. Monte-Carlo techniques, developed to generate a thermal ensemble of field configurations for the purely classical lattice model, are extended to kinetic theory. The equations of motion in the presence of a generic hard mode background are derived. An illustration of the simulation technique is provided by a numerical analysis of non-abelian plasma instabilities. These instabilities have been suggested as a mechanism, analogous to the Weibel instability in QED, for the rapid plasma formation in heavy ion collisions. Initial investigations indicated that an anisotropic hard mode background leads to a rapid energy growth in the weak field regime which is curbed in the non-abelian regime ruling out this scenario for plasma formation. Recent research has shown, however, that the growth of energy densities continues deep into the non-abelian regime for sufficiently anisotropic backgrounds. These findings are supported by the results presented in this thesis for an
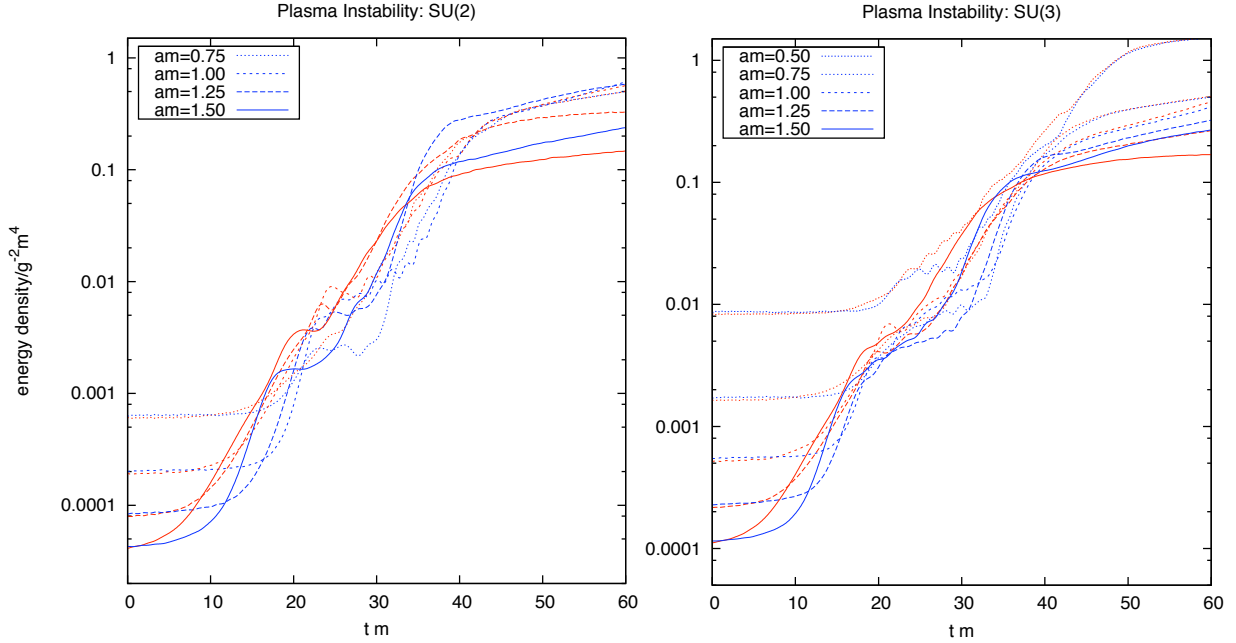
Figure 11.5: *Left:* Growth rates of the electric (blue) and magnetic (red) energy densities at extreme anisotropy for SU(2) obtained on lattices with volume $(20a)^3$ and spherical cutoff $l_{\max} = 16$. *Right:* The growth rates for SU(3) using a similar lattice layout are in astonishing agreement with the rates for SU(2) for identical effective masses m.

asymptotically strong anisotropy of the background distribution. An unabated exponential growth of energy densities is observed which is only limited by the bounded magnetic energy density on the lattice due to the compact nature of plaquettes as shown in figure 11.5. Non-abelian plasma instabilities are investigated the first time for SU(3) in the full framework of kinetic theory. An astonishing agreement between the growth rates of energy densities for SU(2) and SU(3) is observed.

Note: The results presented for the non-abelian plasma instabilities are part of ongoing research.

Suggested Research: The general framework developed in chapter 9 could, for instance, be used to study the plasma formation in non-central collisions. Additional theoretical and numerical work is required to reproduce continuum hydrodynamics on the lattice in a kinetic theory framework.

A Notation and Conventions

A.1 Notation

A.1.1 Euclidean and Minkowski Space Notation

Employing the usual Minkowski space notation covariant or contravariant space-time indices are written in greek letters while spatial indices will be indicated by latin letters. The sign convention for the metric is:

$$g^{\mu\nu} = \begin{pmatrix} 1 & 0 & 0 & 0 \\ 0 & -1 & 0 & 0 \\ 0 & 0 & -1 & 0 \\ 0 & 0 & 0 & -1 \end{pmatrix}. \tag{A.1}$$

The Lorentz indices 0 and 4 denote the temporal component in a Minkowskian and Euclidean context respectively. In general a $d+1$ dimensional Minkowski space is denoted as $\mathbb{R}^{d,1}$ while the corresponding euclidean space is $\mathbb{R}^{d+1}$. 4-momenta are denoted by a captial letter in Minkowski space, i.e. $K = (\omega, \boldsymbol{k})$. Spatial momenta are generally indicated by a bold print while the absolute size of the spatial momentum is shown in a normal print $k = |\boldsymbol{k}|$.

A.1.2 Einstein Convention

The usual summation convention according to Einstein is used implying a summation over co- and contravariant indices denoted by the same letter and appearing in the same product. Euclidean, color as well as Schwinger-Keldysh contour indices are summed over if they appear repeatedly in a product unless explicitly indicated otherwise.

A.1.3 Abbreviations

The use of abbreviations has been avoided to improve readability. A few standard acronyms have been used nevertheless and are listed here in an alphabetical order for convenience:

- AdS: Anti de Sitter
- BNL: Brookhaven National Laboratory
- CERN: European Organization for Nuclear Research
- CFT: Conformal Field Theory
- FAIR: Facility for Antiprotons and Ions Research
- HTL: Hard Thermal Loop
- KMS: Kubo-Martin-Schwinger
- LHC: Large Hadron Collider
- QCD: Quantum Chromodynamics
- QED: Quantum Electrodynamics
- QFT: Quantum Field Theory
- RHIC: Relativistic Heavy Ion Collider
- SPS: Super Proton Synchrotron

A.2   Special Matrices

A.2.1   Pauli Matrices

The Pauli matrices represent the generators for SU(2). In a lattice context these matrices need to be multiplied with $1/\sqrt{2}$ to take the normalization Tr $T^a T^b = 1/2\delta_{ab}$ into account.

$$\sigma^1 = \begin{pmatrix} 0 & 1 \\ 1 & 0 \end{pmatrix}, \quad \sigma^2 = \begin{pmatrix} 0 & -i \\ i & 0 \end{pmatrix}, \quad \sigma^3 = \begin{pmatrix} 1 & 0 \\ 0 & -1 \end{pmatrix}. \tag{A.2}$$

A.2.2   Gell-Mann Matrices

The Gell-Mann matrices represent the generators for SU(3). Just like the Pauli matrices they need to be multiplied with $1/\sqrt{2}$ in a lattice contextto take the normalization Tr $T^a T^b = 1/2\delta_{ab}$ into account.

$$\lambda^1 = \begin{pmatrix} 0 & 1 & 0 \\ 1 & 0 & 0 \\ 0 & 0 & 0 \end{pmatrix}, \quad \lambda^2 = \begin{pmatrix} 0 & -i & 0 \\ i & 0 & 0 \\ 0 & 0 & 0 \end{pmatrix}, \quad \lambda^3 = \begin{pmatrix} 1 & 0 & 0 \\ 0 & -1 & 0 \\ 0 & 0 & 0 \end{pmatrix},$$

$$\lambda^4 = \begin{pmatrix} 0 & 0 & 1 \\ 0 & 0 & 0 \\ 1 & 0 & 0 \end{pmatrix}, \quad \lambda^5 = \begin{pmatrix} 0 & 0 & -i \\ 0 & 0 & 0 \\ i & 0 & 0 \end{pmatrix}, \quad \lambda^6 = \begin{pmatrix} 0 & 0 & 0 \\ 0 & 0 & 1 \\ 0 & 1 & 0 \end{pmatrix},$$

$$\lambda^7 = \begin{pmatrix} 0 & 0 & 0 \\ 0 & 0 & -i \\ 0 & i & 0 \end{pmatrix} \quad \text{and} \quad \lambda^8 = \frac{1}{\sqrt{3}} \begin{pmatrix} 1 & 0 & 0 \\ 0 & 1 & 0 \\ 0 & 0 & -2 \end{pmatrix}. \tag{A.3}$$

A.2.3 γ- Matrices

The γ- matrices are conveniently defined from the Pauli matrices and take the form

$$\gamma^\mu = \begin{pmatrix} 0 & \sigma^\mu \\ \overline{\sigma}^\mu & 0 \end{pmatrix}, \qquad \gamma^5 = \begin{pmatrix} -\mathbf{1} & 0 \\ 0 & \mathbf{1} \end{pmatrix}. \tag{A.4}$$

where $\sigma^\mu = (\mathbf{1}, \boldsymbol{\sigma})$, $\overline{\sigma}^\mu = (\mathbf{1}, -\boldsymbol{\sigma})$ and $\mathbf{1}$ denotes a 2×2 unit matrix.

A.3   Lattice Notation

Gauge Fields and Plaquettes:

$$U_\mu(x) = W_{x \to x + \hat{\mu}} = e^{iga\tilde{A}_\mu(x)} \quad \text{and} \quad U_{\mu\nu}(x) = U_\mu(x)U_\nu(x + \hat{\mu})U_\mu^+(x + \hat{\nu})U_\nu^+(x). \tag{A.5}$$

Electrical and Magnetic Fields on a Hamiltonian Lattice:

$$\dot{U}_i(x,t) = iE_i(x,t)U_i(x,t) \quad \text{and} \quad B_i^a(x) = \text{Im Tr} T^a \left(U_{i,j}(x) + U_{j,-i}(x) + U_{-i,-j}(x) + U_{-j,i}(x) \right). \tag{A.6}$$

Scaling Conventions:

$$a^2 g E_i \leftrightarrow E_i, \quad agB_i \leftrightarrow B_i, \quad agW \leftrightarrow W, \quad \text{and} \quad \frac{t}{a} \to t. \tag{A.7}$$

B Schwinger-Keldysh Formalism

In this chapter the Schwinger-Keldysh notation and Feynman rules for Yang-Mills theory are summarized. Self-energies and resummed propagators for the special cases of thermal equilibrium and an anisotropic medium are listed.

B.1 Real-Time Correlators

Let $\hat{\varphi}(t), \psi(t')$ be two operators, which are local in time and contained in the Schwinger-Keldysh contour ζ. The real-time correlator for these operators is defined as:

$$\mathrm{i}\boldsymbol{G} = \mathrm{i} \begin{pmatrix} G_{11} & G_{12} \\ G_{21} & G_{22} \end{pmatrix} = \begin{pmatrix} \langle \mathrm{T}\hat{\psi}(t')\hat{\varphi}(t)\rangle & -\langle \hat{\varphi}(t)\hat{\psi}(t')\rangle \\ \langle \hat{\psi}(t')\hat{\varphi}(t)\rangle & \langle \tilde{\mathrm{T}}\hat{\psi}(t')\hat{\varphi}(t)\rangle \end{pmatrix}. \tag{B.1}$$

Individual components are related via the following constraint which follows from their definition:

$$G_{11} + G_{22} = G_{12} + G_{21}. \tag{B.2}$$

B.1.1 Retarded, Advanced and Symmetric Components

The constraint (B.2) is explicitly accounted for in a basis of retarded (R), advanced (A) and symmetric (S) components

$$\boldsymbol{G}' = \boldsymbol{R}^{-1} \cdot \boldsymbol{G} \cdot \boldsymbol{R} = \begin{pmatrix} 0 & G_A \\ G_R & G_S \end{pmatrix}. \tag{B.3}$$

with the following transformation matrix mediating between both representation:

$$\boldsymbol{R} = \frac{1}{\sqrt{2}} \begin{pmatrix} 1 & 1 \\ -1 & 1 \end{pmatrix} \quad \text{and} \quad \boldsymbol{R}^{-1} = \frac{1}{\sqrt{2}} \begin{pmatrix} 1 & -1 \\ 1 & 1 \end{pmatrix}. \tag{B.4}$$

Self-energies transform via:

$$\boldsymbol{\Pi}' = \boldsymbol{R}^{-1} \cdot \boldsymbol{\Pi} \cdot \boldsymbol{R} = \begin{pmatrix} \Pi_S & \Pi_R \\ \Pi_A & 0 \end{pmatrix}. \tag{B.5}$$

B.1.2 Homogeneous Systems

In a homgeneous system where the statistical operator is independent of space-time the correlator $\mathbf{G}(x, x')$ of two local operators $\hat{\varphi}(x)$ and $\hat{\psi}(x')$ depends only on the separation between both positions $\mathbf{G} = \mathbf{G}(x - x')$. A momentum space representation of the correlator is defined via:

$$\mathbf{G}(K) = \int \mathrm{d}^{d+1}x\, \mathrm{e}^{\mathrm{i}K_\mu x^\mu} \mathbf{G}(x), \quad \mathbf{G}(x) = \int \frac{\mathrm{d}^{d+1}K}{(2\pi)^{d+1}} \mathrm{e}^{-\mathrm{i}K_\mu x^\mu} \mathbf{G}(K) \tag{B.6}$$

These real-time correlators obey an additional contraint which reduces the number of independent correlator components to two:

$$G_A(K) = G_R^*(K). \tag{B.7}$$

In the special case of thermal equilibrium there is only one independent component of the correlator due to the Kubo-Martin-Schwinger condition:

$$G_{12}(K) = \mathrm{e}^{-\beta\omega}G_{21}(K). \tag{B.8}$$

For a free gas of scalar bosons, characterized by a momentum distribution $f(\boldsymbol{p})$, the following propagator is obtained in a homogeneous system

$$\boldsymbol{G}(P) = \boldsymbol{G}^{\mathrm{vac}}(P) + \boldsymbol{G}^{\mathrm{med}}(P), \tag{B.9}$$

where the vacuum component is defined as

$$\boldsymbol{G}^{\mathrm{vac}}(P) = \begin{pmatrix} \frac{1}{\omega^2-\pi(\boldsymbol{p})+\mathrm{i}\epsilon} & 0 \\ 0 & \frac{-1}{\omega^2-\pi(\boldsymbol{p})-\mathrm{i}\epsilon} \end{pmatrix} - 2\pi\mathrm{i}\delta(\omega^2 - \pi(\boldsymbol{p})) \begin{pmatrix} 0 & \Theta(-\omega) \\ \Theta(\omega) & 0 \end{pmatrix} \tag{B.10}$$

while the in-medium component is:

$$\boldsymbol{G}^{\mathrm{med}}(P) = -2\pi\mathrm{i}\delta(\omega^2 - \pi(\boldsymbol{p}))f(\boldsymbol{p}) \begin{pmatrix} 1 & 1 \\ 1 & 1 \end{pmatrix}. \tag{B.11}$$

B.2 Yang-Mills Theory

B.2.1 Feynman Rules

The basic building blocks for a naive diagramatic expansion of Yang-Mills theory in a medium characterized by the (gluonic) momentum distribtion $f(\boldsymbol{p})$ are listed in the following.

1. *Gluon Propagator*

   The bare gluon propagator $\boldsymbol{G}_{\mu\nu}^{ab}$ in a general covariant gauge with gauge parameter λ takes the following form [24]

   $$\mathrm{i}\boldsymbol{G}_{\mu\nu}^{ab}(K) = \delta_{ab}\left\{\left[g_{\mu\nu} + (\lambda-1)\frac{K_\mu K_\nu}{K^2}\right]\boldsymbol{G}^{\mathrm{vac}} - P_{T\mu\nu}\boldsymbol{G}^{\mathrm{med}}\right\}, \tag{B.12}$$

   using the components of the bare scalar boson propagator. P_T is the transverse projector.

2. *Ghost Propagator*

   The propagator for each component of the ghost field is identical to the scalar boson propagator (3.22) at vanishing temperature,

   $$\boldsymbol{S}^{ab} = -\mathrm{i}\delta_{ab}\boldsymbol{G}^{\mathrm{vac}}, \tag{B.13}$$

   since ghost particles can not be interpreted as physical plasma constituents.

3. *Interaction Vertices*

   The 3- and 4-vertices for the gluon self interaction as well as the ghost-gluon vertex are identical to their vacuum counterparts [18] on the forward part of the contour. Type 2 vertices differ by an opposite sign.

To calculate an amplitude in momentum space all topologically different diagrams are drawn and a summation is performed over all possible combinations of type 1 and 2 vertices which are joined by the appropriate entries of the bare real time propagators. Momentum conservation is imposed at every vertex and an integration is performed over the remaining unconstrained momenta appearing in the propagators.

B.2.2   Schwinger-Dyson Relations

The Schwinger Dyson relation for the resummed two point function $\tilde{\boldsymbol{G}}$ takes the following form in momentum space

$$\tilde{\boldsymbol{G}} = \boldsymbol{G} + \boldsymbol{G} \cdot \boldsymbol{\Pi} \cdot \tilde{\boldsymbol{G}}, \tag{B.14}$$

where $\boldsymbol{\Pi}$ is the self energy resumming one particle irreducible interactions and $\boldsymbol{G}$ the bare propagator. The bold print indicates matrices with respect to Schwinger-Keldysh indices. In a basis of retarded, advanced and symmetric components the following set of Schwinger-Dyson equations for the resummed two-point function ensues:

$$
\begin{aligned}
\tilde{\boldsymbol{G}}_{\mathrm{R,A}} &= \boldsymbol{G}_{\mathrm{R,A}} + \boldsymbol{G}_{\mathrm{R,A}} \cdot \boldsymbol{\Pi}_{\mathrm{R,A}} \cdot \tilde{\boldsymbol{G}}_{\mathrm{R,A}}, \\
\tilde{\boldsymbol{G}}_{\mathrm{S}} &= \boldsymbol{G}_{\mathrm{S}} + \boldsymbol{G}_{\mathrm{R}} \cdot \boldsymbol{\Pi}_{\mathrm{R}} \cdot \tilde{\boldsymbol{G}}_{\mathrm{S}} + \boldsymbol{G}_{\mathrm{S}} \cdot \boldsymbol{\Pi}_{A} \cdot \tilde{\boldsymbol{G}}_{\mathrm{A}} + \boldsymbol{G}_{\mathrm{R}} \cdot \boldsymbol{\Pi}_{\mathrm{S}} \cdot \tilde{\boldsymbol{G}}_{\mathrm{A}} .
\end{aligned}
\tag{B.15}
$$

B.2.3   Thermal Equilibrium

The retarded gluon propagator to first loop order has the following form in thermal equilibrium

$$G_R^{\mu\nu}(K) = \frac{1}{K^2 - \Pi_T} P_T^{\mu\nu} + \frac{1}{K^2 - \Pi_L} P_L^{\mu\nu} - \frac{\lambda}{K^4} K^\mu K^\nu \tag{B.16}$$

where the projectors on longitudinal and transverse components are defined via:

$$P_T^{00} = P_T^{0i} = 0, \quad P_T^{ij} = \delta_{ij} - \frac{K^i K^j}{k^2}, \quad \text{and} \quad P_L^{\mu\nu} = -g^{\mu\nu} + \frac{K^\mu K^\nu}{K^2} - P_T^{\mu\nu}. \tag{B.17}$$

The retarded self energy has been decomposed into longitudinal and transverse components

$$\Pi_R = P_L \Pi_L + P_T \Pi_T \tag{B.18}$$

which take the following form for soft external momenta $K \ll T$

$$\Pi_L = m_D^2 \left[1 - \frac{\omega^2}{k^2} \right] \left[1 - \frac{\omega}{2k} \log \frac{\omega+k}{\omega-k} \right], \quad \Pi_T = \frac{m_D^2}{2} \frac{\omega^2}{k^2} \left[1 - \frac{\omega^2 - k^2}{2\omega k} \log \frac{\omega+k}{\omega-k} \right]. \tag{B.19}$$

Note that the physical branch of the logarithm is Im $\log(\omega + k)/(\omega - k) = -\pi \Theta(k^2 - \omega^2)$. Other components of the resummed gluon propagator as well as self energy are conveniently obtained via the Kubo-Martin-Schwinger condition as well as $\tilde{G}_R = \tilde{G}_A^*$.

B.2.4   Anisotropic Media

Anisotropic media are characterized by a momentum distribution of gluons of the form

$$f(\boldsymbol{k}, \xi) = N(\xi) \, f_{\text{iso}} \left(\sqrt{\boldsymbol{k}^2 + \xi(\boldsymbol{k} \cdot \boldsymbol{n})^2} \right), \tag{B.20}$$

where $\boldsymbol{n}$ is the anisotropy vector, ξ the strength of the anisotropy and $N(\xi)$ a normalization factor which is chosen as $N(\xi = 0) = \sqrt{1+\xi}$ to keep the particle density independent of ξ. The resummed retarded gluon propagator in a covariant gauge takes the following general form in an anisotropic medium:

$$\tilde{G}_R^{\mu\nu}(K) = \Delta_A [A^{\mu\nu} - C^{\mu\nu}] + \Delta_G \left[(K^2 - \alpha - \gamma) \frac{\omega^4}{K^4} B^{\mu\nu} + (\omega^2 - \beta) C^{\mu\nu} + \delta \frac{\omega^2}{K^2} D^{\mu\nu} \right] - \frac{\lambda}{K^4} K^\mu K^\nu . \tag{B.21}$$

The structure function $\alpha(K) - \delta(K)$ are obtained by decomposing the retarded self-energy into the following components

$$\Pi_R^{\mu\nu}(K) = \alpha A^{\mu\nu} + \beta B^{\mu\nu} + \gamma C^{\mu\nu} + \delta D^{\mu\nu} = g^2 \int \frac{\mathrm{d}^3 \boldsymbol{p}}{(2\pi)^3} v_p^\mu \frac{\partial f(\boldsymbol{p})}{\partial P^\beta} \left(g^{\nu\beta} - \frac{v^\nu K^\beta}{K \cdot v + \mathrm{i}\epsilon} \right). \tag{B.22}$$

The tensor basis employed for the expansion of the gluon propagator and self energy has the following general form for an anisotropic medium characterized by a plasma velocity m and anisotropy vector n:

$$
\begin{aligned}
A^{\mu\nu} &= -g^{\mu\nu} + \frac{K^\mu K^\nu}{K^2} + \frac{\tilde{m}^\mu \tilde{m}^\nu}{\tilde{m}^2} \\
B^{\mu\nu} &= -\frac{K^2}{(m \cdot K)^2} \frac{\tilde{m}^\mu \tilde{m}^\nu}{} \\
C^{\mu\nu} &= \frac{\tilde{m}^2 K^2}{\tilde{m}^2 K^2 + (n \cdot K)^2} \left[\tilde{n}^\mu \tilde{n}^\nu - \frac{\tilde{m} \cdot \tilde{n}}{\tilde{m}^2} (\tilde{m}^\mu \tilde{n}^\nu + \tilde{m}^\nu \tilde{n}^\mu) + \frac{(\tilde{m} \cdot \tilde{n})^2}{\tilde{m}^4} \tilde{m}^\mu \tilde{m}^\nu \right] \\
D^{\mu\nu} &= \frac{K^2}{m \cdot K} \left[2 \frac{\tilde{m} \cdot \tilde{n}}{\tilde{m}^2} \tilde{m}^\mu \tilde{m}^\nu - (\tilde{n}^\mu \tilde{m}^\nu + \tilde{m}^\mu \tilde{n}^\nu) \right]
\end{aligned}
\tag{B.23}
$$

Here $\tilde{x}$ is defined as

$$\tilde{x}^\mu = x^\mu - \frac{x \cdot K}{K^2} K^\mu. \tag{B.24}$$

Note that the direction of the anisotropy affects only the tensors C and D. For a plasma at rest the plasma velocity has the form $m = (1, 0, 0, 0)$. The components A and B correspond to the transverse and longitudinal projectors up to a rescaling of the longitudinal projector. Other components of the resummed gluon propagator can be obtained using $G_R = G_A^*$, the Schwinger-Dyson relations and the symmetric self energy:

$$\mathrm{i}\Pi_S^{\mu\nu} = 8\pi g^2 N \frac{1}{k} \int \frac{d^3 p}{(2\pi)^3} v_p^\mu v_p^\nu f(\boldsymbol{p})(1 + f(\boldsymbol{p} + \boldsymbol{k})) \delta(\boldsymbol{v}_p \cdot \boldsymbol{v}_k). \tag{B.25}$$

C Classical and Kinetic Theory

C.1 Classical Theory

C.1.1 Continuum

The statistical partition function for classical Yang-Mills theory is

$$Z_{cl} = \int [\mathrm{D}A][\mathrm{D}E]\delta(\mathrm{D}_i E^i)\mathrm{e}^{-\beta H_{YM}}, \quad H_{YM} = -\int \mathrm{d}^d x \mathrm{Tr}\left\{E_i E^i + \frac{1}{2}F_{ij}F^{ij}\right\} \tag{C.1}$$

with the following Euler-Lagrange equations describing the time evolution of individual field configurations $[j^\mu = 0$ in the purely classical theory$]$:

$$\begin{aligned}
\partial_t \mathbf{B} &= -\nabla \times \mathbf{E} & \textit{(Faraday's law of induction)} & \tag{C.2}\\
\partial_t \mathbf{E} &= \mathbf{D} \times \mathbf{B} - \mathbf{j} & \textit{(Ampere's circuital law)} & \tag{C.3}\\
\mathrm{D} \cdot \mathbf{E} &= j^0 & \textit{(Gauss's law)} & \tag{C.4}
\end{aligned}$$

Electric and magnetic fields are defined via:

$$E_i = -F_{0i} \qquad \text{and} \qquad B_i = \frac{1}{2}\epsilon_{ijk}F_{jk}. \tag{C.5}$$

The classical partition function is dual to a Yang-Mills theory coupled to a massless adjoint Higgs:

$$Z_{cl} = \int [\mathrm{D}A][\mathrm{D}\varphi] \, \exp\left\{-\beta \int \mathrm{d}^d \boldsymbol{x} \mathrm{Tr}\left[\frac{1}{2}F_{ij}F^{ij} - \frac{1}{4}\mathrm{D}_i\varphi \mathrm{D}^i\varphi\right]\right\}. \tag{C.6}$$

C.1.2 Lattice

On a Hamiltonian lattice the partition function for classical Yang-Mills theory is

$$Z_L = \int [\mathrm{D}U] \int [\mathrm{D}E] \, \delta(G) \, \mathrm{e}^{-\beta H_L}. \tag{C.7}$$

where the Hamiltonian H_L of the lattice model is chosen to take the form

$$H_L(t) = \sum_x \left\{a^3 \mathrm{Tr} E_i(x,t)E_i(x,t) + \beta_L \sum_{i<j}\left\{1 - \frac{1}{N}\mathrm{Re} \, \mathrm{Tr} U_{ij}(x,t)\right\}\right\}. \tag{C.8}$$

and $\beta_L = 2N/ag^2$. The Euler Lagrange equations of motion are

$$\begin{aligned}
\dot{U}_i(x,t) &= \mathrm{i}E_i(x,t)U_i(x,t) & \textit{(Faraday's law of induction)} & \tag{C.9}\\
\dot{E}_i^a(x,t) &= 2\sum_{|j|\neq i} \mathrm{Im} \, \mathrm{Tr}\left\{T^a U_{ij}(x,t)\right\} & \textit{(Ampere's circuital law)} & \tag{C.10}
\end{aligned}$$

where the first relation is used as a definition for the color electric field on the lattice and a Gauss constraint needs to be satisfied by all field configurations of the ensemble:

$$\sum_i \left\{E_i(x,t) - U_{-i}(x,t)E_i(x-\hat{i},t)U_{-i}^+(x,t)\right\} = 0. \tag{C.11}$$

By equating the Debye masses in the continuum and on the lattice

$$m_D^2 = \frac{N}{3} g^2 T^2, \quad m_{D,L}^2 = \frac{N\Sigma}{2\pi} \frac{g^2 T}{a},$$ (C.12)

where $\Sigma = 3.175911536\ldots$, the lattice spacing is identified as

$$a = \frac{3}{2} \frac{\Sigma}{\pi T}.$$ (C.13)

The discretized partition function for the Yang-Mills theory coupled to an adjoint Higgs takes the form

$$Z_L = \int [\mathrm{D}U][\mathrm{D}\varphi]\, \mathrm{e}^{-\beta H_L}$$ (C.14)

where the lattice Hamiltonian is chosen as

$$H_L = \sum_x \left[\beta_L \sum_{i<j} \left\{ 1 - \frac{1}{N} \mathrm{Re\ Tr} U_{ij} \right\} + \frac{\beta_L}{N} \mathrm{Tr} \left\{ \phi(x)\phi(x) - \kappa \sum_i \phi(x) U_i(x) \phi(x+\hat{i}) U_i^+(x) \right\} \right],$$ (C.15)

using the rescaling $ag\varphi \leftrightarrow 2\varphi$ and $\kappa = 1/3$.

C.2   Kinetic Theory

C.2.1   Kinetic Theory in the Continuum

Employing an Expansion in spherical harmonics the equation of motion for the spherical components of the hard mode distribution is

$$\partial_t W_{lm}^a = -(\mathrm{D}_i W_{l'm'})^a C_{lml'm'}^i + E_i^{aE} X_{l'm'}^i + B_i^{aB} X_{l'm'}^i,$$ (C.16)

where the hard mode current j entering the classical field equations is defined as:

$$j^0 = \frac{m^2}{2\sqrt{\pi}} W_{00}^a \quad \text{and} \quad j^i = \frac{m^2}{4\pi} (v_m^i)^* W_{1m}^a.$$ (C.17)

The background distribution Ω enters the kinetic equations via the constants $^E X, {}^B X$:

$$
\begin{aligned}
{}^E X_{l'm}^i &= \int \mathrm{d}\Omega_v Y_{lm}^* (2v^i - \nabla_v^i)\Omega = \sum_{l'm'} \Omega_{l'm'} \left(3 + \frac{l(l+1) - l'(l'+1)}{2} \right) C_{lml'm'}^i, \\
{}^B X_{lm}^i &= \epsilon_{ijk} \int \mathrm{d}\Omega_v Y_{lm}^* v^j \nabla_v^k \Omega = -\frac{1}{2} \sum_{abl'm'} \Omega_{l'm'} \epsilon_{ijk} a(a+1) C_{lmab}^j C_{abl'm'}^k.
\end{aligned}
$$ (C.18)

In the special case of an isotropic medium the equation of motion for the hard mode distribution takes a simplified form:

$$\partial_t W_{l'm'}^a = -(\mathrm{D}_i W_{lm})^a C_{l'm'lm}^i + \delta_{l1} v_m^i E_i^a.$$ (C.19)

The constants v_m^i and $C_{lml'm'}^i$ are listed below.

C.2.2 Lattice Discretization

The discretization of the Vlasov equation is straightforward and complicated only by the term involving the chromo-magnetic field $B_i(x)$ which vanishes in thermal equilibrium:

$$\dot{W}_{lm} = -C^i_{lml'm'}\frac{1}{2}\left(U_i(x)W_{l'm'}(x+i)U^+_i(x) - U_{-i}(x)W_{l'm'}(x-i)U^+_{-i}(x)\right) + \tag{C.20}$$

$$+{}^EX^i_{lm}\frac{1}{2}\left(E_i(x) + U_{-i}(x)E_i(x-i)U^+_{-i}(x)\right) + {}^BX^i_{lm}\frac{1}{2}\left(B_i(x) + U_{-i}(x)B_i(x-i)U^+_{-i}(x)\right).$$

The hard mode current j at every lattice site is defined via

$$j_0(x) = \frac{m^2}{2\sqrt{\pi}}W_{00}(x) \quad \text{and} \quad j_i(x) = \frac{m^2}{4\pi}v^{i*}_m W_{1m}(x). \tag{C.21}$$

C.2.3 Spherical Constants

The constants v^i_m are defined via

$$\boldsymbol{v}_m = \int \mathrm{d}\Omega Y^*_{lm}\boldsymbol{v} = \begin{pmatrix} -\delta_{m1}\sqrt{\frac{2\pi}{3}} + \delta_{m,-1}\sqrt{\frac{2\pi}{3}} \\ i\delta_{m1}\sqrt{\frac{2\pi}{3}} + i\delta_{m,-1}\sqrt{\frac{2\pi}{3}} \\ \delta_{m0}\sqrt{\frac{4\pi}{3}} \end{pmatrix}. \tag{C.22}$$

The constants $C^i_{lml'm'}$ parametrize the coupling between the Vlasov equations for individual spherical components

$$C^i_{lml'm'} = \int \mathrm{d}\Omega_v Y^*_{lm}v^j Y_{l'm'} \tag{C.23}$$

and can be expressed in the following form for $l' = l+1$

$$C^i_{lml'm'} = \begin{pmatrix} \frac{1}{\sqrt{2}}\left[\delta_{m',m-1}A(l,-m) - \delta_{m',m+1}A(l,m)\right] \\ \frac{i}{\sqrt{2}}\left[-\delta_{m',m-1}A(l,-m) + \delta_{m',m+1}A(l,m)\right] \\ \delta_{m,m'}B(l,m) \end{pmatrix} \tag{C.24}$$

where the coefficient $A(l,m)$ and $B(l,m)$ are defined via

$$A(l,m) = \sqrt{\frac{(l+2+m)(l+1+m)}{2(2l+1)(2l+3)}} \quad \text{and} \quad B(l,m) = \sqrt{\frac{(l+1-m)(l+1+m)}{2(2l+1)(2l+3)}}. \tag{C.25}$$

For $l' = l-1$ the following form is obtained:

$$C^i_{lml'm'} = \begin{pmatrix} \frac{1}{\sqrt{2}}\left[-\delta_{m',m-1}A(l',m') + \delta_{m',m+1}A(l',-m')\right] \\ \frac{i}{\sqrt{2}}\left[\delta_{m',m-1}A(l',m') - \delta_{m',m+1}A(l',-m')\right] \\ \delta_{m,m'}B(l',-m') \end{pmatrix}. \tag{C.26}$$

If $|l' - l| \neq 1$ the constants vanish.

D   Technical Implementation of the Simulations
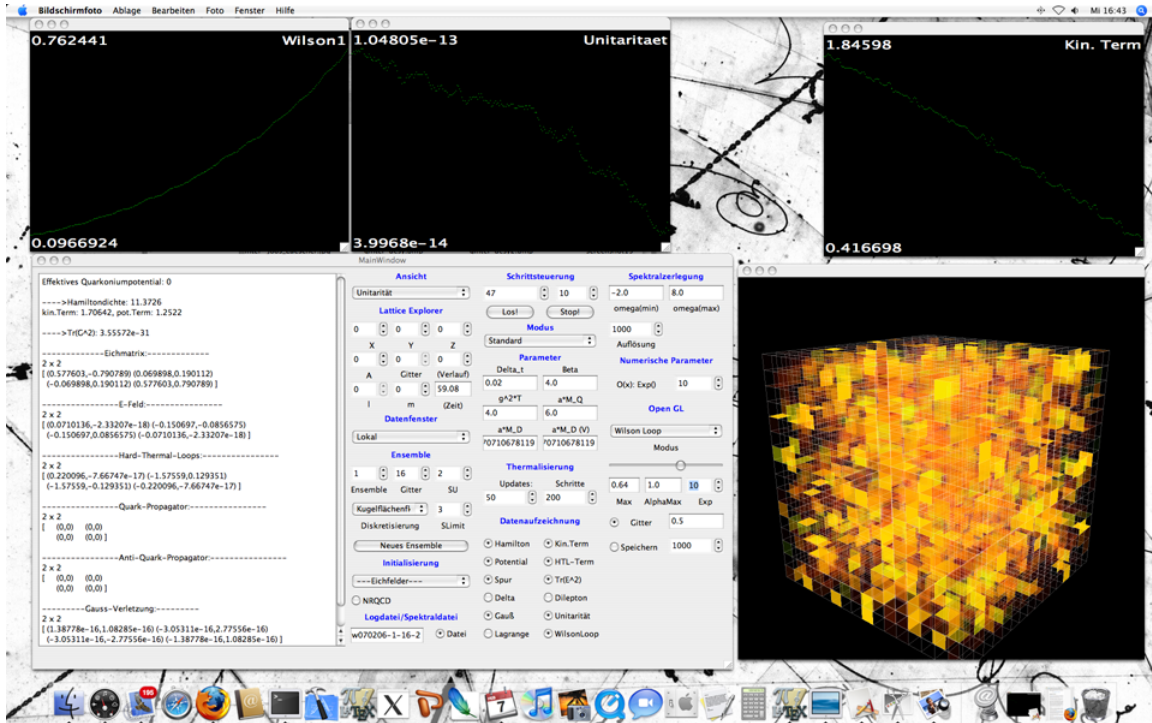
Figure D.1: Main Window for the Classical Simulation

- Compiler and OS: gcc 4.1, Debian Linux (Etch,Lenny) and Mac OS X (10.5, Leopard)

- Library providing Basic Lattice Functionality: QDP++

- Graphical User Interfaces: Qt 4.1

- 3D-Visualization: Open-GL

- Various Numerical Routines: "Numerical Recipes in C++"'

LIST OF FIGURES

Bibliography

[1] C. N. Yang and R. L. Mills, "Conservation of isotopic spin and isotopic gauge invariance," Phys. Rev. **96**, 191 (1954).

[2] M. Gell-Mann, "A Schematic Model Of Baryons And Mesons," Phys. Lett. **8**, 214 (1964).

[3] O. W. Greenberg, "Spin And Unitary Spin Independence In A Paraquark Model Of Baryons And Phys. Rev. Lett. **13**, 598 (1964).

[4] M. Y. Han and Y. Nambu, "Three-triplet model with double SU(3) symmetry," Phys. Rev. **139**, B1006 (1965).

[5] K. G. Wilson, "CONFINEMENT OF QUARKS," Phys. Rev. D **10**, 2445 (1974).

[6] V. N. Gribov, "Quantization of non-Abelian gauge theories," Nucl. Phys. B **139**, 1 (1978).

[7] G. 't Hooft, "50 years of Yang-Mills Theory," World Scientific, 2005

[8] D. J. Gross and F. Wilczek, "ULTRAVIOLET BEHAVIOR OF NON-ABELIAN GAUGE THEORIES," Phys. Rev. Lett. **30**, 1343 (1973).

[9] H. D. Politzer, "RELIABLE PERTURBATIVE RESULTS FOR STRONG INTERACTIONS?," Phys. Rev. Lett. **30**, 1346 (1973).

[10] E. Witten, "The Problem Of Gauge Theory," arXiv:0812.4512 [math.DG].

[11] F. Jüttner, Ann. Phys. **34**, 856 (1911).

[12] J. I. Kapusta and C. Gale, "Finite-temperature field theory: Principles and applications," *Cambridge, UK: Univ. Pr. (2006) 428 p*

[13] C. Hagen, F. Bruckmann, E. Bilgici and C. Gattringer, "Thin and dressed Polyakov loops from spectral sums of lattice differential operators," PoS **LAT2007**, 289 (2007) [arXiv:0710.0294 [hep-lat]].

[14] F. Karsch, "Properties of the Quark Gluon Plasma: A lattice perspective," Nucl. Phys. A **783**, 13 (2007) [arXiv:hep-ph/0610024].

[15] B. Svetitsky and L. G. Yaffe, "Critical Behavior At Finite Temperature Confinement Transitions," Nucl. Phys. B **210**, 423 (1982).

[16] J. Langelage, G. Munster and O. Philipsen, "Strong coupling expansion for finite temperature Yang-Mills theory in the confined phase," JHEP **0807**, 036 (2008) [arXiv:0805.1163 [hep-lat]].

[17] M. E. Peskin and D. V. Schroeder, "An Introduction To Quantum Field Theory," *Reading, USA: Addison-Wesley (1995) 842 p*; L. H. Ryder, *Cambridge, Uk: Univ. Pr. (1985) 443p*

[18] M. LeBellac, "Thermal Field Theory," *Cambridge University Press () p*

[19] J. S. Schwinger, J. Math. Phys. **2**, 407 (1961).

[20] L. V. Keldysh, Zh. Eksp. Teor. Fiz. **47** (1964) 1515 [Sov. Phys. JETP **20** (1965) 1018].

[21] E. M. Lifshitz, L. P. Pitaevskii, "Effective kinetic theory for high temperature gauge theories," *Physical Kinetics* (Pergamon Press, 1981)

[22] H. A. Weldon, "Covariant Calculations At Finite Temperature: The Relativistic Plasma," Phys. Rev. D **26**, 1394 (1982).

[23] N. P. Landsman and C. G. van Weert, "Real and Imaginary Time Field Theory at Finite Temperature and Density," Phys. Rept. **145**, 141 (1987).

[24] C. W. Kao, G. C. Nayak and W. Greiner, "Closed-time path integral formalism and medium effects of non-equilibrium QCD matter," Phys. Rev. D **66**, 034017 (2002) [arXiv:hep-ph/0102153].

[25] P. V. Landshoff and A. Rebhan, "Covariant gauges at finite temperature," Nucl. Phys. B **383**, 607 (1992) [Erratum-ibid. B **406**, 517 (1993)] [arXiv:hep-ph/9205235].

[26] M. D'Attanasio and M. Pietroni, "Gauge-invariant renormalization group at finite temperature," Nucl. Phys. B **498**, 443 (1997) [arXiv:hep-th/9611038].

[27] S. Caron-Huot, "Hard thermal loops in the real-time formalism," JHEP **0904**, 004 (2009) [arXiv:0710.5726 [hep-ph]].

[28] M. Laine, O. Philipsen, P. Romatschke and M. Tassler, "Real-time static potential in hot QCD," JHEP **0703**, 054 (2007) [arXiv:hep-ph/0611300].

[29] M. Laine, O. Philipsen and M. Tassler, "Thermal imaginary part of a real-time static potential from classical lattice gauge theory simulations," JHEP **0709**, 066 (2007) [arXiv:0707.2458 [hep-lat]].

[30] M. Laine, O. Philipsen and M. Tassler, "Wilson Loop in Classical Lattice Gauge Theory and the Thermal Width of Heavy Quarkonium," PoS **LAT2007**, 230 (2007) [arXiv:0710.0504 [hep-lat]].

[31] M. Tassler, "Heavy Quarkonia beyond Deconfinement and Real Time Lattice Simulations," PoS C **ONFINEMENT8**, 118 (2008) [arXiv:0812.3225 [hep-lat]].

[32] J. J. Aubert *et al.* [E598 Collaboration], "Experimental Observation Of A Heavy Particle J," Phys. Rev. Lett. **33**, 1404 (1974).

[33] J. E. Augustin *et al.* [SLAC-SP-017 Collaboration], "Discovery Of A Narrow Resonance In E+ E- Annihilation," Phys. Rev. Lett. **33**, 1406 (1974).

[34] T. Matsui and H. Satz, "J/psi Suppression by Quark-Gluon Plasma Formation," Phys. Lett. B **178**, 416 (1986).

[35] N. Brambilla, J. Ghiglieri, A. Vairo and P. Petreczky, "Static quark-antiquark pairs at finite temperature," Phys. Rev. D **78**, 014017 (2008) [arXiv:0804.0993 [hep-ph]].

[36] A. Dumitru, Y. Guo and M. Strickland, "The heavy-quark potential in an anisotropic (viscous) plasma," Phys. Lett. B **662**, 37 (2008) [arXiv:0711.4722 [hep-ph]].

[37] M. Laine, "A resummed perturbative estimate for the quarkonium spectral function in hot QCD," JHEP **0705** (2007) 028 [arXiv:0704.1720 [hep-ph]].

[38] Y. Burnier, M. Laine and M. Vepsalainen, "Heavy quarkonium in any channel in resummed hot QCD," JHEP **0801**, 043 (2008) [arXiv:0711.1743 [hep-ph]].

[39] L. D. McLerran and T. Toimela, "Photon And Dilepton Emission From The Quark - Gluon Plasma: Some General Considerations," Phys. Rev. D **31**, 545 (1985).

[40] H. A. Weldon, "Reformulation Of Finite Temperature Dilepton Production," Phys. Rev. D **42**, 2384 (1990).

[41] C. Gale and J. I. Kapusta, "Vector dominance model at finite temperature," Nucl. Phys. B **357**, 65 (1991).

[42] N. Gausmann, M. Tassler, in preparation

[43] O. Philipsen and M. Tassler, "On quarkonium in an anisotropic quark gluon plasma," arXiv:0908.1746 [hep-ph].

[44] P. Romatschke and M. Strickland, "Collective modes of an anisotropic quark gluon plasma," Phys. Rev. D **68**, 036004 (2003) [arXiv:hep-ph/0304092].

[45] P. Romatschke and M. Strickland, "Collective modes of an anisotropic quark-gluon plasma. II," Phys. Rev. D **70** (2004) 116006 [arXiv:hep-ph/0406188].

[46] S. Mrowczynski, A. Rebhan and M. Strickland, "Hard-loop effective action for anisotropic plasmas," Phys. Rev. D **70**, 025004 (2004) [arXiv:hep-ph/0403256].

[47] A. Dumitru, Y. Guo, A. Mocsy and M. Strickland, "Quarkonium states in an anisotropic QCD plasma," arXiv:0901.1998 [hep-ph].

[48] Y. Burnier, M. Laine and M. Vepsalainen, "Quarkonium dissociation in the presence of a small momentum space anisotropy," Phys. Lett. B **678**, 86 (2009) [arXiv:0903.3467 [hep-ph]].

[49] A. Dumitru, Y. Guo and M. Strickland, "The imaginary part of the static gluon propagator in an anisotropic (viscous) QCD plasma," Phys. Rev. D **79**, 114003 (2009) [arXiv:0903.4703 [hep-ph]].

[50] P. Romatschke and M. Strickland, "Energy Loss of a Heavy Fermion in an Anisotropic QED Plasma," Phys. Rev. D **69** (2004) 065005 [arXiv:hep-ph/0309093].

[51] P. Arnold, G. D. Moore and L. G. Yaffe, "Effective kinetic theory for high temperature gauge theories," JHEP **0301**, 030 (2003) [arXiv:hep-ph/0209353].

[52] M. A. Escobedo and J. Soto, "Non-relativistic bound states at finite temperature (I): the hydrogen atom," arXiv:0804.0691 [hep-ph].

[53] A. Beraudo, J. P. Blaizot and C. Ratti, "Real and imaginary-time $Q\bar{Q}$ correlators in a thermal medium," Nucl. Phys. A **806** (2008) 312 [arXiv:0712.4394 [nucl-th]].

[54] S. Mrowczynski and M. H. Thoma, "Hard loop approach to anisotropic systems," Phys. Rev. D **62**, 036011 (2000) [arXiv:hep-ph/0001164].

[55] M. Laine, G. D. Moore, O. Philipsen and M. Tassler, "Heavy Quark Thermalization in Classical Lattice Gauge Theory: Lessons for Strongly-Coupled QCD," JHEP **0905**, 014 (2009) [arXiv:0902.2856 [hep-ph]].

[56] S. Mrowczynski, "Plasma instability at the initial stage of ultrarelativistic heavy ion collisions," Phys. Lett. B **314**, 118 (1993).

[57] P. Arnold, J. Lenaghan and G. D. Moore, "QCD plasma instabilities and bottom-up thermalization," JHEP **0308** (2003) 002 [arXiv:hep-ph/0307325].

[58] T. Hahn, "CUBA: A library for multidimensional numerical integration," Comput. Phys. Commun. **168**, 78 (2005) [arXiv:hep-ph/0404043].

[59] G. Arfken, *Mathematical Methods for Physicists, 3rd ed.* (Orlando, FL: Academic Press, 1985)

[60] J. Crank, P. Nicolson, Proceedings of the Cambridge Philosophical Society. **43**, 50-64 (1947)

[61] I. Montvay and G. Münster, "Quantum fields on a lattice," *Cambridge, UK: Univ. Pr. (1994) 491 p. (Cambridge monographs on mathematical physics)*

[62] F. Green and F. Karsch, "Mean Field Analysis Of SU(N) Deconfining Transitions In The Presence Of Dynamical Quarks," Nucl. Phys. B **238**, 297 (1984).

[63] S. Fortunato, "Percolation and deconfinement in SU(2) gauge theory," arXiv:hep-lat/0012006.

[64] J. Langelage, M. Tassler, in preparation

[65] L. D. McLerran and B. Svetitsky, "Quark Liberation At High Temperature: A Monte Carlo Study Of SU(2) Gauge Theory," Phys. Rev. D **24**, 450 (1981).

[66] L. S. Brown and W. I. Weisberger, "Remarks On The Static Potential In Quantum Chromodynamics," Phys. Rev. D **20**, 3239 (1979).

[67] S. Nadkarni, "NONABELIAN DEBYE SCREENING. 2. THE SINGLET POTENTIAL," Phys. Rev. D **34**, 3904 (1986).

[68] O. Jahn and O. Philipsen, "The Polyakov loop and its relation to static quark potentials and free energies," Phys. Rev. D **70**, 074504 (2004) [arXiv:hep-lat/0407042].

[69] M. Creutz, "Gauge Fixing, The Transfer Matrix, And Confinement On A Lattice," Phys. Rev. D **15**, 1128 (1977).

[70] M. Luscher, "Construction Of A Selfadjoint, Strictly Positive Transfer Matrix For Euclidean Lattice Gauge Theories," Commun. Math. Phys. **54**, 283 (1977).

[71] J. B. Kogut and L. Susskind, "Hamiltonian Formulation Of Wilson's Lattice Gauge Theories," Phys. Rev. D **11**, 395 (1975).

[72] M. Luscher and P. Weisz, "Quark confinement and the bosonic string," JHEP **0207**, 049 (2002) [arXiv:hep-lat/0207003].

[73] A. Dumitru, Y. Hatta, J. Lenaghan, K. Orginos and R. D. Pisarski, "Deconfining phase transition as a matrix model of renormalized Polyakov loops," Phys. Rev. D **70**, 034511 (2004) [arXiv:hep-th/0311223].

[74] O. Philipsen, "On the non-perturbative gluon mass and heavy quark physics," Nucl. Phys. B **628**, 167 (2002) [arXiv:hep-lat/0112047].

[75] O. Kaczmarek, M. Laine, O. Philipsen and M. Tassler, in preparation

[76] D. Y. Grigoriev and V. A. Rubakov, "SOLITON PAIR CREATION AT FINITE TEMPERATURES. NUMERICAL STUDY IN (1+1)-DIMENSIONS," Nucl. Phys. B **299**, 67 (1988).

[77] J. Ambjorn, T. Askgaard, H. Porter and M. E. Shaposhnikov, "LATTICE SIMULATIONS OF ELECTROWEAK SPHALERON TRANSITIONS IN REAL TIME," Phys. Lett. B **244**, 479 (1990).

[78] D. Bodeker, L. D. McLerran and A. V. Smilga, "Really computing nonperturbative real time correlation functions," Phys. Rev. D **52**, 4675 (1995) [arXiv:hep-th/9504123].

[79] P. Arnold, "Hot B violation, the lattice, and hard thermal loops," Phys. Rev. D **55**, 7781 (1997) [arXiv:hep-ph/9701393].

[80] S. Nadkarni, "The SU(2) Adjoint Higgs Model In Three-Dimensions," Nucl. Phys. B **334**, 559 (1990).

[81] A. Hart, O. Philipsen, J. D. Stack and M. Teper, "On the phase diagram of the SU(2) adjoint Higgs model in 2+1 dimensions," Phys. Lett. B **396**, 217 (1997) [arXiv:hep-lat/9612021].

[82] G. D. Moore, "Motion of Chern-Simons Number at High Temperatures under a Chemical Potential," Nucl. Phys. B **480**, 657 (1996) [arXiv:hep-ph/9603384].

[83] B. Bunk, "Monte Carlo methods and results for the electro-weak phase transition," Nucl. Phys. Proc. Suppl. **42**, 566 (1995).

[84] G. D. Moore and D. Teaney, "How much do heavy quarks thermalize in a heavy ion collision?," Phys. Rev. C **71**, 064904 (2005) [arXiv:hep-ph/0412346].

[85] S. Caron-Huot and G. D. Moore, "Heavy quark diffusion in perturbative QCD at next-to-leading order," Phys. Rev. Lett. **100**, 052301 (2008) [arXiv:0708.4232 [hep-ph]].

[86] G. D. Moore, "Improved Hamiltonian for Minkowski Yang-Mills theory," Nucl. Phys. B **480**, 689 (1996) [arXiv:hep-lat/9605001].

[87] S. Caron-Huot, M. Laine and G. D. Moore, "A way to estimate the heavy quark thermalization rate from the lattice," JHEP **0904**, 053 (2009) [arXiv:0901.1195 [hep-lat]].

[88] E. Braaten and R. D. Pisarski, "Soft Amplitudes in Hot Gauge Theories: A General Analysis," Nucl. Phys. B **337**, 569 (1990).

[89] J. C. Taylor and S. M. H. Wong, "THE EFFECTIVE ACTION OF HARD THERMAL LOOPS IN QCD," Nucl. Phys. B **346**, 115 (1990).

[90] J. P. Blaizot and E. Iancu, "Kinetic equations for long wavelength excitations of the quark - gluon plasma," Phys. Rev. Lett. **70**, 3376 (1993) [arXiv:hep-ph/9301236].

[91] D. Bodeker, G. D. Moore and K. Rummukainen, "Chern-Simons number diffusion and hard thermal loops on the lattice," Phys. Rev. D **61**, 056003 (2000) [arXiv:hep-ph/9907545].

[92] J. P. Blaizot and E. Iancu, "Energy momentum tensors for the quark - gluon plasma," Nucl. Phys. B **421**, 565 (1994) [arXiv:hep-ph/9401211].

[93] M. Tassler, "Schwere Quarkonia vor einem Thermischen Hintergrund,"

[94] M. A. York and G. D. Moore, "Second order hydrodynamic coefficients from kinetic theory," Phys. Rev. D **79**, 054011 (2009) [arXiv:0811.0729 [hep-ph]].

[95] A. Rebhan, P. Romatschke and M. Strickland, "Dynamics of quark-gluon plasma instabilities in discretized hard-loop approximation," JHEP **0509**, 041 (2005) [arXiv:hep-ph/0505261].

[96] E. S. Weibel, "Spontaneously Growing Transverse Waves In A Plasma Due To An Anisotropic Velocity Distribution," Phys. Rev. Lett. **2**, 83 (1959).

[97] M. S. Wei, F. N. Beg, E. L. Clark, A. E. Dangor, R. G. Evans, A. Gopal, K. W. D. Ledingham, P. McKenna, P. A. Norreys, M. Tatarakis, M. Zepf, M. and K. Krushelnick, "Observation of the filamentation of high-intensity laser-produced electron beams," Phys. Rev. E **70**, 056412 (2004).

[98] P. Arnold, G. D. Moore and L. G. Yaffe, "The fate of non-abelian plasma instabilities in 3+1 dimensions," Phys. Rev. D **72**, 054003 (2005) [arXiv:hep-ph/0505212].

[99] D. Bodeker and K. Rummukainen, "Non-abelian plasma instabilities for strong anisotropy," JHEP **0707**, 022 (2007) [arXiv:0705.0180 [hep-ph]].

[100] P. Arnold and G. D. Moore, "Non-Abelian Plasma Instabilities for Extreme Anisotropy," Phys. Rev. D **76**, 045009 (2007) [arXiv:0706.0490 [hep-ph]].